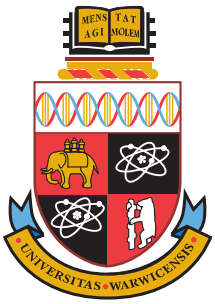

New Approaches and Applications in Electrochemical Scanning Probe Microscopy

by

Kim Martin McKelvey

Thesis

Submitted to the University of Warwick

for the degree of

Doctor of Philosophy

Supervisors: Prof. Patrick R. Unwin, Prof. Colin Robinson and Prof. Julie V. Macpherson

MOAC Doctoral Training Centre

December 2012

THE UNIVERSITY OF WARWICK

In loving memory of Grandad and Granny.

Contents

List of Figures

List of Tables

Abbreviations

EC-SPM	Electrochemical Scanning Probe Microscopy
SECM	Scanning Electrochemical Microscopy
IC	Intermittent Contact
IC-SECM	Intermittent Contact SECM
FEM	Finite Element Method
SECCM	Scanning Electrochemical Cell Microscopy
UME	Ultramicroelectrode
CV	Cyclic Voltamogram
AFM	Atomic Force Microscopy
TG/SC	Tip Generation/Substrate Collection
TC/SG	Tip Collection/Substrate Generation
PC	Personal Computer
DAQ	Data Acquisition
FPGA	Field Programmable Gate Array
AC-SECM	Alternating Current SECM
TPM-SECM	Tip Position Modulation SECM
SICM	Scanning Ion Conductance Microscopy

HIC-SECM	Hopping IC-SECM
AC	Alternating Current
DC	Direct Current
TM	Tapping Mode
FcTMA	Ferrocenylmethyltrimethylammonium
SGS	Strain Gauge Sensor
EPSRC	Engineering and Physical Sciences Research Council
MOAC	Molecular Organisation and Assembly in Cells
DTC	Doctoral Training Centre
SEM	Scanning Electron Microscope
QRE	Quasi Reference Electrode
QRCE	Quasi Reference Counter Electrode
FIFO	First-in First-out
DCE	Dual Carbon Electrode
DCMU	3-(3,4-dichlorophenyl)-1,1-dimenthylurea
PSI	Photosystem I
PSII	Photosystem II
PANI	Polyaniline

Acknowledgments

Firstly, I would like to thank my supervisors, Prof. Patrick Unwin, Prof. Colin Robinson and Prof. Julie MacPherson, for their encouragement and support.

I also thank the mechanical and electronic workshops for their amazing skills, and Alex Colburn for the superb custom electronics, without which our science would not be possible.

All my friends and colleagues in the Electrochemistry and Interfaces group, and the CR group, for all the science, and extra curricular activities, over the last three years.

I would like to acknowledge and thank the MOAC DTC and EPSRC for the support and funding. I would especially like to thank the 2008 MOAC intake, without which the last four years would not have been so enjoyable. Let's hope Daisy lives on.

I thank my family, Mum, Ella, Tim, Dad, Nan, Bessie and Lulu, for making me who I am.

Last, but most importantly, Leoni Baker, for pretending to listen to my random science rants and taking me to as many beaches as possible.

Declarations

The work presented in this thesis is entirely original and my own work, except where acknowledged in the text. I confirm that this thesis has not been submitted for a degree at another University.

Chapter 2 was published as:

McKelvey, K.; Edwards, M. A.; Unwin, P. R., Intermittent Contact-Scanning Electrochemical Microscopy (IC-SECM): A New Approach for Tip Positioning and Simultaneous Imaging of Interfacial Topography and Activity. *Anal. Chem.* **2010**, 82, 6334 - 6337.

Chapter 3 was published as:

McKelvey, K.; Snowden, M. E.; Peruffo, M.; Unwin, P. R., Quantitative visualization of molecular transport through porous membranes: enhanced resolution and contrast using intermittent contact-scanning electrochemical microscopy. *Anal. Chem.* **2011**, 83, 6447 - 6454.

Chapter 4 contains some data from Dr. Sophie Martin's thesis (University of Warwick, 2009) which has been reanalysed, together with new data. It is in preparation for:

Kim McKelvey, Sophie Martin, Colin Robinson and Patrick R. Unwin, Quantitative local photosynthetic flux measurements at intact chloroplasts and thylakoid membranes using scanning electrochemical microscopy (SECM)

Chapter 5 describes a new EC-SPM instrument that was constructed. This con-

tributed to the following papers:

Güell, A. G., Ebejer, N., Snowden, M. E., **McKelvey, K.**, Macpherson, J. V., and Unwin, P. R. Quantitative nanoscale visualization of heterogeneous electron transfer rates in 2D carbon nanotube networks. *Proc. Natl. Acad. Sci. USA*, **2012**, 109(29), 11487 - 11492.

Lai, S. C. S., Patel, A. N., **McKelvey, K.**, and Unwin, P. R. Definitive evidence for fast electron transfer at pristine basal plane graphite from high-resolution electrochemical imaging. *Angew. Chem. Int. Edit.*, **2012**, 51(22), 5405 - 5408.

Snowden, M. E., Güell, A. G., Lai, S. C. S., **McKelvey, K.**, Ebejer, N., OConnell, M. A., Colburn, A. W., et al. Scanning electrochemical cell microscopy: theory and experiment for quantitative high resolution spatially-resolved voltammetry and simultaneous ion-conductance measurements. *Anal. Chem.*, **2012**, 84(5), 2483 - 2491.

Patel, A. N., Guille Collignon, M., OConnell, M. A., Hung, W. O. Y., **McKelvey, K.**, Macpherson, J. V., and Unwin, P. R. A New View of Electrochemistry at Highly Oriented Pyrolytic Graphite (HOPG). *J. Am. Chem. Soc.*, **2012**, 134(49), 20117 - 20130.

Patel, A. N., **McKelvey, K.**, and Unwin, P. R. Nanoscale Electrochemical Patterning Reveals the Active Sites for Catechol Oxidation at Graphite Surfaces. *J. Am. Chem. Soc.*, **2012**, 134(50), 20246 - 20249.

Chapter 6 is in preparation for:

Kim McKelvey, *et al* Fabrication, Characterisation and Applications of Dual Carbon Electrodes

Chapter 7 is in preparation for:

Kim McKelvey, Michael A. O'Connell, Patrick R. Unwin, Meniscus Confined Fabrication of Nanoscale Multidimensional Conducting Polymer Structures with Positional Feedback

Abstract

This thesis is concerned with the development of new electrochemical scanning probe techniques and the application of these to biological problems. These techniques allow high resolution quantitative investigations of surface processes through measurements at a precisely placed electrode probe.

A new technique, called intermittent contact scanning electrochemical microscopy, which allowed the probe-surface distance to be decisively determined through the physical interaction of the probe with the surface was developed. Separately, a new type of dual electrode probe was developed and characterised, and a new instrument (including both hardware and software) capable of a wide range of electrochemical imaging modes was developed with wide applications.

The quantitative analysis of the electrochemical signal, typically measured at the probe, requires understanding the mass transport between the probe and the surface. Finite element modelling was used extensively throughout to solve the mass transport problem and therefore quantitatively analyse experimental results.

Intermittent contact scanning electrochemical microscopy was used to quantify the mass transport through a porous biological membrane, dentin, that separates the pulp and enamel in teeth. Oxygen generation and consumption rates during photosynthesis were determined by measuring the local oxygen flux at an electrode placed a precise distance above a monolayer of isolated chloroplasts or thylakoid membranes. Finally, the new dual electrode probe was used to measure the reduction of an artificial electron acceptor by isolated thylakoid membranes.

Chapter 1

Introduction

This thesis is concerned with the development of new electrochemical scanning probe microscopy (EC-SPM) techniques and the application of these techniques to the quantitative study of biological systems. The new EC-SPM techniques allow a probe to be placed a precise distance from a surface, such as a biological sample, which, in turn, enables quantitative analysis of the subsequent electrochemical signal. Therefore, the basic principles of EC-SPM, with a particular focus on tip positioning techniques, are discussed in this introduction to give a context to the subsequent chapters.

Each chapter, except Chapter 5, is self contained and based on journal articles that are in print or in preparation. Chapter 2 describes the development of a new probe positioning technique called intermittent contact scanning electrochemical microscopy (IC-SECM). This technique is inspired by the vertical oscillation of a probe (see tip position modulation SECM, Section 1.2.4, below) and the idea of using a non-electrochemical feedback mechanism (see shear force SECM, Section 1.2.5, below). This new technique is used to measure pressure driven molecular transport through dentin, a biological membrane, in Chapter 3. Chapter 4 describes the use of SECM to measure the oxygen generation and consumption during photosynthesis, and the subsequent data analysis, using a finite element method (FEM) simulation,

to extract the oxygen generation rates. Chapter 5 describes the construction of new EC-SPM instruments. A new dual electrode probe is described and characterised in Chapter 6 (see Section 1.2.7 below of the context). Finally, the fabrication of nanoscale structures using scanning electrochemical cell microscopy (SECCM, see Section 1.2.11 for the background) is demonstrated in Chapter 7. The final chapter, 8, draws together the different research projects and points to future directions for this work.

1.1 Dynamic Electrochemistry

The tip electrode, used in EC-SPM, typically functions as the working electrode at which an electrochemical signal is measured. This signal is often the result of the potential-dependent oxidation or reduction of a solution phase species at the electrode. The solution phase species is transported to the electrode surface, reduced or oxidized by the electrode, and then transported back into the bulk of the solution.[1] A schematic of the basic steps of this process is shown in Figure 1.1. Each step may be complicated, but the ultimate rate of an electrochemical reaction depends on the slowest step.[1] For simple systems, which were used exclusively in this thesis, adsorption/desorption and/or chemical reaction steps were unimportant. This greatly simplified the system and the rate of oxidation or reduction only depended on the mass transport of species to, and away from, the electrode surface and, in some situations, the rate of electron transfer at the electrode surface.

The potential of the working electrode is controlled with respect to a reference electrode, typically an Ag/AgCl wire herein, which has a fixed potential in solution. However, the applied potential is also reduced by an ohmic potential drop term, iR, due to solution resistance. When currents are small and when the solution resistance is reduced through the additional high background electrolyte concentration, typically KCl herein, the ohmic potential drop is negligible, as is the polarisation

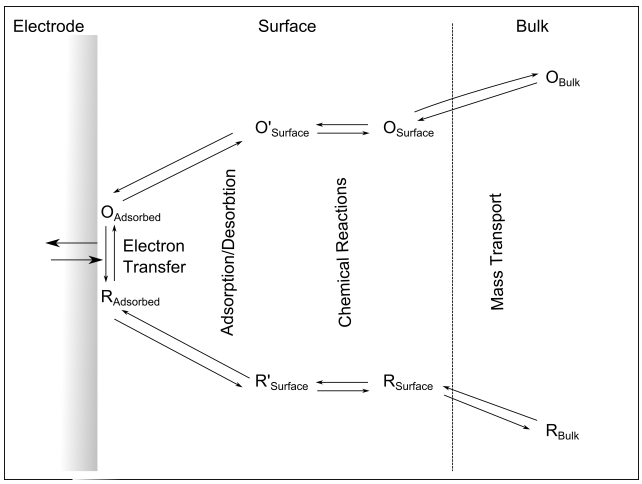

Figure 1.1: Components of a general electrode reaction. Species in the bulk of the solution are transported to the electrode surface, where further chemical reactions and adsorption can occur, before being reduced or oxidised by the electrode. Adapted from Bard and Faulkner.[1]

of the reference electrode, and a two-electrode configuration can be used. However, if the currents are large, or there is significant solution resistance, a three-electrode configuration has to be used. An additional counter electrode, which can be any convenient electrode, typically a Pt wire, which does not effect the electrode of interest, is used to pass the current. This arrangement means that negligible current is drawn through the reference electrode, which maintains a constant potential.

1.1.1 Mass Transport

The mass transport of a solution phase species is typically governed by three components: diffusion, convection and migration. The Nernst-Plank equation describes the contributions of all three components to the steady state flux, J, of species c, and can be written as:

$$J = -D\nabla c + uc - \frac{zF}{RT}Dc\nabla\phi \tag{1.1}$$

where D is the diffusion coefficient, u is the fluid velocity, z is the charge on the species, F is Faraday's constant, R is the ideal gas constant, T is the temperature and ϕ is the electric field. The first term, diffusion, is the concentration gradient inducted flux of active species, described by Fick's 1st law. The second term, convection, is flux of species due to the movement of the solution in which it is contained. The third term, migration, is the flux due to the movement of charged species in an electric field.

Typically, electrochemical experiments are conducted under conditions, such as high background electrolyte concentrations, to control the mass transport within the system, which usually results in diffusion only transport.

1.1.2 Electron Transfer

Once at the electrode surface a potential-dependent electron transfer reaction can occur. This is thermodynamically possible when the energy of the highest occupied molecular orbital of the active species is greater than the fermi level of electrons in the electrode (and results in the oxidation of the active species) or the lowest unoccupied molecular orbital is less than the fermi level of the active species (and results in the reduction of the active species). For a reversible system, in which the electron transfer at the electrode is fast compared to the mass transport to the electrode surface, the Nernst equation describes the potential, E, dependent concentration of the oxidised, O, and reduced, R, species at the electrode surface and can be written as

$$E = E_0 + \frac{RT}{n_e F} \ln(\frac{O}{R}) \tag{1.2}$$

where E_0 is the standard electrode potential for this redox couple and n_e is the number of electrons transferred.

In systems where the kinetics of the electrode reaction play a significant role the Butler-Volmer equations are typically used to describe the flux of oxidised, O,

and reduced, R, species at the electrode surface. Schematically the system can be written as:

$$O + n_e \underset{k_b}{\overset{k_f}{\rightleftharpoons}} R$$

where k_f and k_b are the first order heterogeneous rate constants for the reduction and oxidation reactions respectively. The rate constants can be expressed as

$$k_f = k^0 exp(-\alpha \frac{n_e F}{RT}(E - E^0)) \tag{1.3}$$

$$k_b = k^0 exp((1 - \alpha) \frac{n_e F}{RT}(E - E^0)) \tag{1.4}$$

where α is the transfer coefficient, k^0 is the standard rate constant and all other variables are as previously defined.

1.1.3 Ultramicroelectrodes

Ultramicroelectrodes (UMEs) are defined as electrodes in which the diffusive mass transport layer is greater than the electrode size,[1–3] which typically means one dimension of the electrode is less than 25 μm on the typical timescale of most voltammetric measurements. UMEs come in many shapes, for example spherical, band or cylindrical,[1,4,5] and have been constructed in sizes down to 1 nm.[6–14] For a typical disk-shaped UME the diffusion profile tends towards hemispherical, as illustrated in Figure 1.2, at the longer times. UMEs offer advantages over larger electrodes, such as high mass transport due to the hemispherical diffusion profile, low ohmic drop (iR drop) due to the low currents generated, and low double-layer charging and capacitances due to the small surface area.[1,15,16] UMEs have been used, in bulk solution, to measure heterogeneous electron-transfer kinetics using both steady-state voltammogram[17,18] and fast scan cyclic voltamogram[19–21] methods and to monitor single nano-particle collisions, among many other possible applications.[22]

Typically, within EC-SPM, and specifically within scanning electrochemical

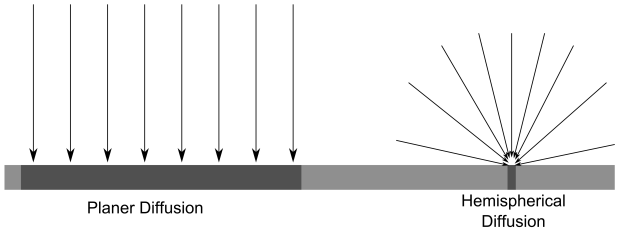

Figure 1.2: Planer (left) and hemispherical (right) diffusion profiles.

microscopy (SECM), disk-shaped UMEs are used. These consist of a planer disk-shaped electrode embedded in the end of a probe. Disk-shaped UMEs are characterised by the electrode radius and by the ratio of surrounding insulating material, in the plane of the electrode, to the electrode radius, known as the RG. Typical values of RG are between 2 and 20.

For a disk-shaped UME the diffusion-limited current, i_∞, can be expressed, from the analytical solution to Fick's 1st law, as:[1,23,24]

$$i_\infty = 4n_e aFDc_\infty \tag{1.5}$$

where c_∞ is the bulk concentration of the active species. Various other geometries, such as hemispherical, have related expressions for the diffusion-limited current.[1,25] However, if the geometry does not conform to any of the standard geometries, or the mass transport contains migration or convection terms, the theoretical current measured at the UME must often be calculated using numerical simulations.[23,26–29]

For concentrations of redox mediator in the mM range, the diffusion-limited current at a disk-shaped UME (micron scale) is in the nA range. Therefore, a two electrode configuration with one reference electrode and a high background electrolyte concentration, typically 20 times the redox mediator concentration, is an appropriate experimental configuration, as discussed above.

1.2 Electrochemical Scanning Probe Microscopy (EC-SPM)

As the name suggests EC-SPM techniques measure an electrochemical signal at a electrochemically active probe as it is scanned across a surface. This is then used to construct an image of the surface properties.

The resolution of EC-SPM techniques is governed by size of the probe. Therefore, increasing the resolution involves decreasing the probe size. As probes become smaller they become difficult to position without crashing into the sample, which damages both, and therefore a feedback mechanism is often required to position them. Having said this, the over whelming majority of SECM studies do not use such a protocol and have been limited to micron scale probes.

Techniques such as atomic force microscopy (AFM) use the physical interaction of a probe with the surface as a feedback mechanism.[30] Within EC-SPM the electrochemical signal often depends on the probe-surface distance and therefore can also be used as a feedback mechanism to control the position of the probe with respect to the surface.[23] However, this distance must also be known to extract quantitative information about the surface processes from the electrochemical signal[23] and, if the distance is not known, the electrochemical signal could potentially be interpreted incorrectly.

Broadly speaking new EC-SPM techniques try to solve one of two problems: i) how to position a probe in a controlled and measurable manner without crashing the probe into the surface; or ii) how to measure different electrochemical signals in order to enhance the information content. Chapters 2 and 3 describe a new hybrid-SECM technique, IC-SECM, that can be used to solve the first of these problems, and also contributes to the second objective. Chapter 5 describes the instrumentation which allowed the new EC-SPM techniques to be developed. The second of these problems was addressed in Chapters 6 and 7, by showing a new dual

electrode probe and using a dual barrelled pipet technique, SECCM, to construct patterns on surfaces. The SECCM technique also provides well-defined positional feedback response.

1.2.1 Scanning Electrochemical Microscopy (SECM)

SECM was one of the first EC-SPM techniques, being introduced in 1989 by Bard.[31–39] In its most common form, a disk-shaped UME is used as a probe. This is usually immersed in solution containing an electro-active species, and supporting electrolyte, and then placed close to an interface of interest and the electrochemical response of the UME is measured. Scanning electrochemical microscopy (SECM) forms the basis for many techniques[31,32,38–41] with hybrid SECM techniques, where SECM is combined with another technique usually capable of sensing the distance to the surface, typically used to extend and improve SECM.[33,36]

Probes

While a majority of SECM studies use metallic disk-shaped UMEs,[33–35,42] a number of other probes have been used including ion selective electrodes, for example to detect Zn^{2+} and Pb^{2+},[43–48] pH sensitive probes,[49–51] arrays of multiple electrodes[52–54] and recessed tips.[55] The choice of probe depends on the target electrochemical signal and so changes with each experiment. Obviously, ion-selective probes are employed in a potentiometric configuration, with the tip as the indicator electrode and a second reference electrode.[34,36,44,56–58]

Most probes in SECM are operated in an amperometric configuration in which the probe is held at a constant potential and the current generated from an electrochemical reaction is measured. As illustrated in Figure 1.3, when the probe is placed close to a surface, the current depends on the experimental configuration. Although a number of configuration are possible, such as tip generation/substrate collection (TG/SC), tip collection/substrate generation (TC/TG) and competitive

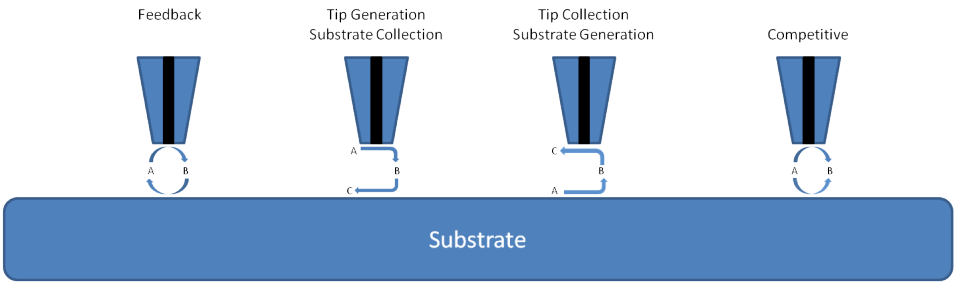

Figure 1.3: Different ways a UME can interact with a surface process. In the feedback mode, the tip oxidises (or reduces) an active species which can be reduced (or oxidised) at the surface, and the tip current is measured.[23,63] In tip generation/substrate collection (TG/SC) mode the tip generates an active species which is collected at the substrate, and the tip and substrate currents are usually measured.[64] In substrate generation/tip collection (SG/TC) mode an active species is generated at the surface and collected at the tip.[65] In competition mode the tip and surface both oxidise or reduce the same species.[66]

mode, the feedback mode is the most common configuration. Probes can also be operated in a potentiometric[56,59] or galvanostatic configuration.[60] In the galvanostatic configuration a feedback circuit is used to maintain a constant current at the probe.[2,61,62]

The spatial resolution of SECM is governed by the mass transport of species to the probe, which is typically restricted by experimental conditions to diffusive transport and so depends on the size of the probe and the probe-surface distance.[67] The temporal resolution typically depends on the diffusion time of active species from the bulk, or a surface, to the probe. However, some probes, such as some pH electrodes, can exhibit significant electrochemical response times,[49,51,68] and so the electrochemical signal can lag local concentration changes.

Approach Curves

An approach curve, in which the electrochemical signal is measured as a function of the distance between the probe and a surface, is the simplest SECM measurement. The probe is moved, usually at a constant rate of between 0.1 and 1 μm s^{-1}, vertically towards the surface and the electrochemical signal monitored throughout.

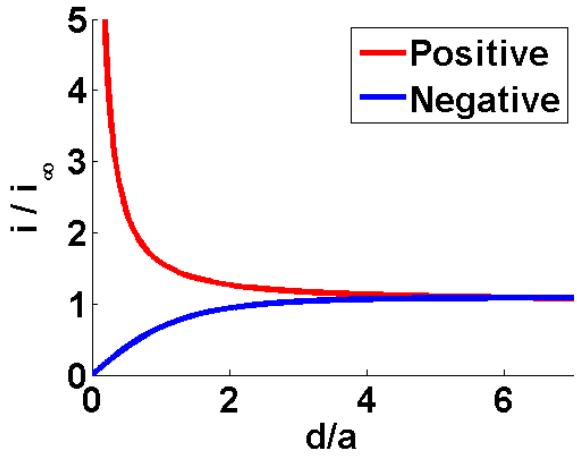

Figure 1.4: Typical approach curves, calculated from published expressions,[72] for a disk-shaped UME (RG=10) operated in feedback mode to conducting and insulating substrates. The current has been normalised by the bulk feedback current, i_∞, and the tip-surface distance normalised by the electrode radius, a.

Note that at very high approach rates the movement of the probe can introduce convection which complicates the analysis of the electrochemical signal by changing the mass transport characteristics.[69] Typical approach curves for a disk-shaped UME, operated in feedback mode, are shown in Figure 1.4. This shows that the current depends on the distance to the surface and on the nature of the surface, with insulating (inert) surfaces hindering the diffusion of active species from the bulk resulting in a decrease in current, and conducting surfaces often acting to regenerate the active species resulting in an increase in the current. When the regeneration of the active species at the substrate is the rate limiting step, or when the substrate has both active and insulating areas, the approach curve falls somewhere within these two extremes. Therefore, based on the profile observed, and by comparing to simulations,[70–73] it is possible to calculate the heterogeneous rate constant, within a reasonable range, for the oxidation or reduction of the active species at a locally uniformly active substrate.

Scanning

The local substrate activity and topography can be observed by scanning the SECM probe laterally across the surface and constructing 2D maps of the electrochemical activity. Typically, the probe is first approached towards a surface using an approach curve and then, at an appropriate distance away from the surface, a scan is initiated.

In its simplest form the probe is scanned laterally in a constant plane (constant height) across the surface as is illustrated in Figure 1.5. A 2D image of the surface is constructed from a series of line scans. However, it is not uncommon for the surface to be misaligned with respect to the lateral plane in which the probe is moved, and therefore at some lateral positions the probe is closer, or further away from the surface. If the surface is particularly badly aligned, or the surface has large topological features, the probe can make contact with the surface which can damage both the probe and the surface. As already mentioned, the electrochemical response of a probe typically depends on the probe-surface distance and therefore any change in this distance can be observed within the electrochemical signal. Figure 1.6 shows an example constant height SECM scan of a flat surface with active (gold) and insulating (glass) areas that was misaligned, obtained as part of my studies for Chapter 2. The probe was close to the surface at the top of the image and the active and insulating areas of the surface are clear, however at the bottom of the image the probe was further from the surface and the resolution was reduced. In general, we are interested in the activity of the surface and therefore the influence of the probe-surface distance on the electrochemical signal complicates matters.

Instead of moving the UME in a single plane the height can be adjusted during the lateral scan to keep a constant current response, this is known a constant current imaging.[74] The resulting motion of the probe traces the topography of a uniformly active surface, as is shown in Figure 1.5. However, samples generally have both topological and activity features, and this scanning scheme does not accurately track these types of surfaces.

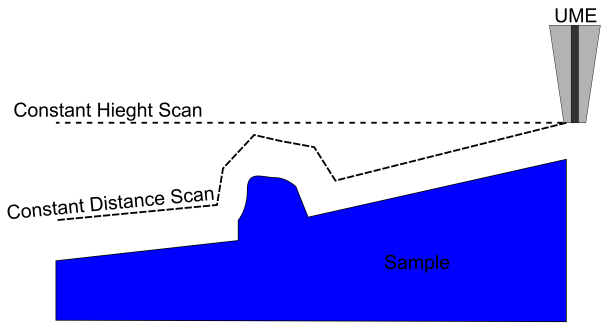

Figure 1.5: Motion of the probe during one line scan, shown as the black dashed lines, within SECM constant height and constant distance scans.

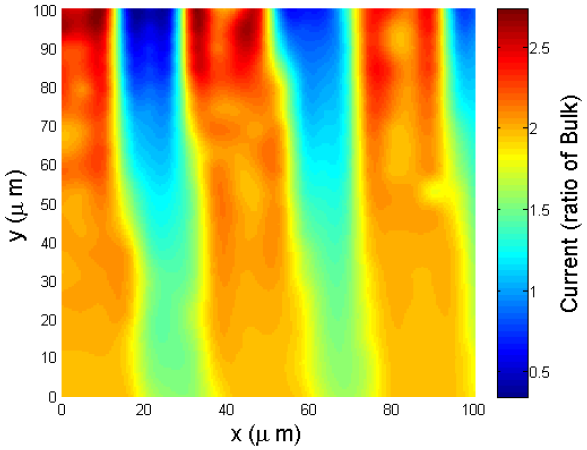

Figure 1.6: Constant height SECM scan of a planer sample of gold bands which is misaligned with respect to the probe movement plane.

The inability to separate the activity and topography in the current response is the major shortcoming of basic SECM and has motivated the development of new probe positioning methods, such as those discussed below. IC-SECM, see Chapters 2 and 3, was developed to overcome this problem.

SECM Instrumentation

The tip electrode used in SECM are typically below 25 μm in size and therefore must be precisely positioned, usually within 12.5 μm of the surface. Peizoelectric positioners are used to achieve accurate, sub-nanometre, positioning. However, piezoelectric positioners only have a range of hundreds of μm which restricts the area which can be scanned and also how close the probe must initially be placed to the surface. The probe position and electrochemical signals are typically measured and controlled by a personal computer (PC) through a data acquisition (DAQ) card. A new EC-SPM instrument is described in Chapter 5 that is capable of implementing SECM, as well as many other EC-SPM techniques.

Applications

SECM has been used for many interesting applications including studying electron transfer kinetics at surfaces,[75–78] studying the movement of charged species across[73,79] and along[80–84] interfaces, studying processes in organic solvents[85] and ionic liquids,[86] studying the corrosion of metals and the application of protective coatings to those metals,[87–92] and investigating single carbon nanotubes,[93] individual nanoparticles[94,95] and boron doped diamond[96] to name just a few.[31,34,36,41,75,76]

Of particular interest to studies in this thesis are a number of studies have investigated mass transport through microscale and nanoscale pores.[47,97,98] Typically, a UME was placed close to the interface containing a nanopore and scanned laterally across the surface. An electrochemical signal generated from species passing through the nanopore and subsequently being detected by the probe was measured.

SECM allows the flux from an isolated individual nanopore to be measured.[47,97,98] Measuring the contribution from an individual pore when the substrate contains a large number of closely spaced pores, for instance within dentin,[99,100] has been reported. Chapter 3 develops this research by using IC-SECM to study the mass transport through individual pores within a dentin sample, and demonstrates enhanced resolution.

Interestingly, SECM has been used to modify surfaces either through the etching of the surface[61,101,102] or deposition of enzymes,[103,104] fluorescent proteins,[105] self assembled monolayers,[106] metals[40,107] or conducting polymers[108] onto the surface. SECM is a solution phase technique and the resolution of any pattern created on a surface is constrained by the size of the probe and, more importantly, by the diffusion of active species away from the probe. Building on the idea of modifying a surface, Chapter 7 shows how a meniscus-based EC-SPM technique, SECCM, allows much higher resolution patterns to be constructed, and also the capability to produce multi-dimensional features.

Finally, a large number of biological systems have been investigated using SECM with a number of reviews covering the topic.[57,109–117] A range of biological systems such as skin,[118,119] cartilage,[120] and model biological systems such as biochemically active beads,[121] giant liposomes[122] and membranes[123,124] have also been investigated. On a larger scale, studies have also looked at detecting finger prints.[54,125,126] Interestingly, when a SECM probe was placed close to a single cell the flux of redox active species, such as oxygen, from the single cell can be detected.[127–134]

A SECM probe, placed over, or inside, a single cell was used to detect redox active mediators that interact with, or are produced by, the photosynthetic system.[135–138] Chapter 4 builds on this work, and uses a SECM configuration to investigate and quantify the oxygen generation and consumption at the location of photosynthesis in higher plants, isolated chloroplasts and thylakoid membranes.

Chapter 6 also shows how a single probe, in this case a dual electrode probe, can be placed close to isolated thylakoid membranes and used to investigate the interaction of an artificial electron acceptor with a thylakoid membrane.

1.2.2 Two Mediators

One of the simplest SECM innovations that allows the topography and electrochemical activity of a surface to be measured separately is to scan the surface twice, first using a mediator that does not interact with the surface, thus establishing the topography, and, second, with the mediator that does interact with the surface, thereby establishing the substrate activity, using the topography data from the first scan. Both of these mediators are present in solution and therefore the scans can be conducted sequentially without changing the solution. This method was used to image the oxygen permeability of cartilage, with an initial scan using the oxidation of hexacyanoruthenate (II) to establish the topography and a second scan for the reduction of oxygen establishing the oxygen permeability of the sample.[120] While successful, this method has seen limited use as it is often difficult to choose appropriate mediators that do not interact with the surface of interest. The idea of using two mediators to separate the topography and surface activity has also been used with a dual electrode probe, as discussed in Section 1.2.7.

1.2.3 Alternating Current (AC)-SECM

Another simple technique that builds on SECM to sense the probe-sample distance is AC-SECM. The potential of the electrode has a small alternating component added that induces an alternating current (AC) component.[139–141] This AC component depends directly on the conductance between the UME and the reference electrode in the bulk of the solution, while the direct current (DC) component depends on the faradaic current generated at the electrode. Therefore, as the probe approaches a surface, the magnitude of the AC drops as ion movement in the gap between

the probe and the substrate is hindered. This can be used as a feedback signal to monitor the distance between the probe and the surface. The AC signal does not depend on a faradaic current and so this technique can be used in a solution that does not contain any redox mediator. This technique is very simple to implement as it uses a standard UME, although it generally requires an external lock-in amplifier to extract the AC components.

AC-SECM is a popular technique that has been used to visualise transport through pores,[142,143] processes on living cells[144] and the corrosion of metallic surfaces.[145,146] An interesting development is the use of a 4D AC-SECM technique in which the frequency of the potential oscillation is also varied.[147,148] However, a significant drawback is that the distance dependent signal depends on the local substrate composition which complicates AC-SECM imaging on heterogeneous samples.

1.2.4 Tip Position Modulation (TPM)-SECM

TPM-SECM is another SECM technique that uses a UME, operated in feedback mode, to detect the tip-substrate distance.[149] The position of the probe is oscillated normal to the surface, typically at an amplitude of hundreds of nanometres. The electrochemical signal at the probe depends on the tip-surface distance, as discussed above, and the vertical oscillation modulates this distance and produces an AC component in the electrochemical signal. The magnitude of the AC component depends on the tip-surface distance and the phase depends on the electrochemical activity of the surface, with insulating and conducting surfaces showing a 180 phase difference. Therefore, the AC magnitude can be used to control the distance between the end of the probe and the surface. Although, a quantitative analysis of the technique has been published,[150] this technique has not proved popular because the tip-substrate distance response also depends on the electrochemical activity of the substrate and this restricts the type of surface that can be imaged stably. An

auto switching control scheme in which the feedback response changes based on the phase of the AC component has been reported,[151] although this has also not proved popular.

IC-SECM (see Chapters 2 and 3) builds on the idea of oscillating the probe normal to the surface of interest and using the AC components to provide additional information about the surface activity.

1.2.5 Shear Force SECM

Shear force SECM is an advanced probe positioning method that uses the fluid damping effects (shear forces) between the end of the probe and the surface, present when a probe is oscillated parallel to the surface (typically at hundreds of kHz), to detect the probe-surface distance.[152,153] This allows the probe to be placed at a precise distance from the surface and, importantly, this is achieved through a signal that is independent of any electrochemical signal.

Typically, specialised needle-like UMEs are used.[154] The end of the probe is immersed in solution and oscillated parallel to the surface of interest. The oscillation amplitude and phase are monitored, and changes at different frequencies are used to sense the distance between the end of the probe and the surface.[155]

A lateral scanning mode, a standing approach mode and a '4D' imaging mode have been used to construct images of surfaces. Within the lateral scanning mode the probe was moved laterally across the surface and a constant shear force signal, typically the oscillation amplitude, was maintained using a feedback loop and so the probe height traces the topography of the surface. The electrochemical signal at the probe was measured throughout, and a 2D map of the substrate electrochemical activity at a constant distance away from the surface is constructed.[156,157] A standing approach mode has also been used, in which a 2D image of the surface topography and activity was constructed from a series of short approach curves. The approach curves automatically terminated when the surface was sensed through the

shear force signal.[158] Finally, a '4D' imaging method was recently introduced, which constructed a 3D profile of the diffusion of the active species away from a surface from a series of approach curves which automatically halted when the surface was detected.[159] Constructing the 3D diffusion profiles above a sample is an interesting and useful method to visualise the local electrochemical activity and allows many 2D images to be constructed from a single 3D data set.

Shear force SECM has been used to investigate interesting samples such as single cells[160] and immobilised enzymes.[161] It has also been combined with optical microscopy[156] and scanning near field microscopy.[153] Although, the non-electrochemical feedback signal employed within shear force SECM allows many types of probe and operation, the restrictions on the probe design, i.e. the need for long tapered probes, and the complex nature of the feedback signal have restricted the applications and development of this technique. In addition, the shear force signal depends on the elastic nature of the surface and therefore the shear force feedback differs on soft samples compared to solid samples.[152] However, the non-electrochemical nature of the feedback signal entirely decouples the measurement of the tip-substrate distance from the electrochemical signal which simplifies the analysis of the electrochemical data.

1.2.6 Atomic Force Microscopy (AFM)-SECM

A different method, which also separates the measurement of the surface topography from the electrochemical signal, is to integrate an electrode into an AFM tip.[162] With this hybrid technique, the electrode is used to sense the electrochemical signal while the AFM tip provides the topography information. The first tips were constructed by hand from Pt wires that had been etched, bent into a cantilever shape and then insulated leaving only the end exposed to form the electrode.[162,163] More sophisticated methods such as modifying commercial AFM probes[164,165] or using micro-fabrication and lithography techniques to make integrated probes[166,167] are

now more common.

Two methods have been used to image a surface, a double scan technique and a parallel measuring technique. Within the double scan technique the topography was first determined by using the probe as a typical AFM tip and then a second scan, taking into account the topography just determined, was conducted at set distance from the surface to measure the electrochemical signal.[168] Within the parallel imaging technique both the sample topography and electrochemical signal at the electrode were measured at the same time, this reduced the time needed to image a surface.[163,169] The unconventional geometry of AFM-SECM probes complicates the mass transport of active redox species to the electrode and therefore custom FEM simulations have been used to quantify the electrochemical response at the electrode.[170–172]

AFM-SECM has been used to detect the diffusion through single nanopores,[173] the correlations between structure and transport within membranes[174] and even in a new molecular touching AFM-SECM mode where the redox active species was immobilised on the tip of the probe.[175] While, AFM-SECM certainly has a bright future the major bottle neck at this point in time is the fabrication of the probes.

1.2.7 Dual Electrode Systems

Typical SECM probes consist of a single electrochemical sensor, usually a UME, at the end of a probe. However, probes with two electrodes embedded in the end have been developed.[176] Each electrode can be controlled independently and therefore used to measure a different electrochemical signal. A number of different electrode geometries have been reported, including dual disk electrodes,[177–180] ring disk electrodes[181] and dual ring electrodes.[182]

Building on the idea of using two mediators in solution (see Section 1.2.2) a dual electrode probe can be used to measure two different redox mediators present in the solution simultaneously. One mediator can be used to detect the distance to

the surface and the other used to detect the activity of the surface. This method has been used to measure the tip-substrate distance and local nitric oxide concentration over endothelial cells[183] and to measure the topography and photosynthetic activity of a single protoplast.[184] An alternative configuration is to use the two independent electrodes in a generation/collection mode in which a redox active species is generated at one electrode and collected at the other electrode.[176]

Although dual electrodes allow many new systems to be investigated the fabrication and characterisation of the probe, again, acts as a bottle neck in the development of the technique. Chapter 6 reports on the construction, characterisation and use of a new simple dual electrode probe that has the potential to overcome these problems.

1.2.8 Scanning Ion Conductance Microscopy (SICM)

Scanning ion conductance microscopy (SICM) is an EC-SPM technique that uses a glass pipet that has been pulled to a sharp point (known as nanopipet) as a probe.[185] This is filled with electrolyte solution and a reference electrode is inserted into the pipet. This is then placed in solution with another reference electrode in the bulk of the solution and an ionic conductance current is induced, by holding the electrodes at different potentials. When the end of the probe is placed close to a surface the ionic conductance current is hindered and decreases. Therefore, the ionic conductance current can be used as a signal to measure the probe-surface distance. The probe is typically oscillated normal to the surface which induces an AC component and the magnitude of this is used as the feedback signal to detect the probe-surface distance.[186–189]

Typically, SICM has been used to image the topography of a sample, for example soft biological systems.[190] With SICM, a lateral scanning procedure, where the probe was moved laterally and the probe-substrate distance kept constant,[185] or a hopping procedure, where the topography was sensed through a series of small

approach curves which halted when the surface was detected[190–192] have been used to extract the topography. Nanopipets can also be used as electrochemical sensors[193–195] or to deliver species to a substrate.[196] In addition, they have been used to detect the flow of species through porous membranes,[197] individual nanopores[198] and detect the passage of DNA strands.[199]

1.2.9 SICM-SECM

The combination of the SICM and SECM techniques into a single probe allows the topography, through the SICM signal, and electrochemical activity, through the SECM signal, to be measured simultaneously. Probes have been fabricated as either a ring electrode surrounding an open barrel that forms the SICM channel,[200–202] or from a dual barrel pipet with an electrode formed in one barrel and the other barrel left open to form the SICM channel.[203]

SICM-SECM scans have been constructed either using a hopping mode, which involved a series of approach curves at different lateral positions across the surface,[204] or a lateral scanning method where the probe was moved laterally and a feedback signal used to keep the probe a constant distance away from the surface.[201,202] The imaging of single nanopores,[202] single living cells,[200,203] and gold electrodes[201] have been demonstrated.

SICM-SECM offers a flexible and practical hybrid electrochemical imaging technique, although, like many others techniques, the fabrication of the probes is the major bottleneck and once addressed this approach should see many more applications.

1.2.10 Scanning micropipet contact method

The liquid meniscus that forms at the end of a pipet which has been filled with solution (containing mediator and supporting electrolyte) can be used as a nano or micro scale positionable electrochemical cell.[205] A reference electrode is inserted

into the pipet and when the liquid meniscus, which can be as small as 150 nm, comes into contact with a sample this forms a working electrode whose size is defined by the contact area of the meniscus. The electrochemical signal is measured at the substrate. This technique has been exploited for high-resolution imaging, using a hopping mode, of the redox activity of an electrode surface.[205] The fabrication of individual nanoscale crystals and thin ZnO films at the interface of the liquid meniscus with the substrate has also been demonstrated.[206,207]

1.2.11 Scanning electrochemical cell microscopy (SECCM)

Finally, scanning electrochemical cell microscopy (SECCM) is a recently developed technique which builds on the idea of using a nanoscale liquid meniscus formed at the end of a dual barrelled pipet.[208–210]

SECCM uses, as a probe, a dual barrelled pipet that has been pulled to a sharp point. Both barrels are filled with solution containing redox mediator and supporting electrolyte. The liquid meniscus that forms at the end of the probe is then used as a positionable nanoscale electrochemical cell, as in the scanning micropipet contact method. A quasi reference counter electrode (QRCE) is inserted into each barrel, and each QRCE is then held at a different potential to induce an ionic conductance current between the barrels, in a similar manner as used for SICM. The conductance current depends on the size and shape of the liquid meniscus at the end of the probe and therefore when this meniscus deforms, as it comes into contact with a surface, this can be measured as a change in the conductance current. This change in the conductance current is used to detect when the meniscus makes contact with a surface (which can be either conductance or insulating) and also as a feedback signal to keep the meniscus in contact with the surface, at a constant distance from the surface, while the probe is moved laterally. A tip modulation scheme is typically used, where the probe is oscillated normal to the surface and the AC components (magnitude and phase) of the conductance current are used as

feedback signals.[211] Over conducting substrates the contact area of the meniscus with the surface forms a working electrode, with the QRCEs in the barrels forming the reference/counter electrode.

This technique has been used to image single nano particles,[212] graphene,[213] carbon nanotubes,[214] highly orientated pyrolytic graphite,[214] conducting polymers[215] and boron doped diamond.[216]

The new EC-SPM instruments, described in Chapter 5, were designed, in part, for the SECCM technique. Finally, Chapter 7 shows how SECCM can be expanded to fabricate nanoscale structures on surfaces.

1.3 Finite Element Method (FEM) Simulations

The electrochemical signal depends on the mass transport of an active species to the electrode and the subsequent oxidation or reduction of species. Quantitative analysis of the electrochemical signal requires a solution to the mass transport problem which depends on the geometry of the system and on the underlying mass transport equations.

For simple geometries, such as a disk-shaped UMEs, the diffusive mass transport to the electrode in a bulk solution can be solved analytically, giving results such as Equation 1.5. However, when the probe is placed close to a surface the mass transport equations becomes difficult to solve analytically. In these situations numerical methods are typically used to find an approximate solution to the mass transport problem. For a simple disk-shaped UME, operated in feedback mode, expressions based on the numerical solutions to the underlying mass transport problem have been published and can be used to analyse experimental data.[70–72]

However, for more complex geometries, or when the underlying mass transport characteristics differ, custom numerical simulations are needed solve the mass transport problem and quantify electrochemical signals. The FEM is one numerical

technique that can be used to solve these problems. Commercial FEM software packages, such as Comsol, are typically used to find numerical solutions.

FEM simulations solve, numerically, a partial differential equation over a domain of interest (which usually is 1, 2 or 3 dimensional) subject to boundary and initial conditions. Within EC-SPM applications the partial differential equation that describes the mass transport within the domain of interest was usually the Nernst-Plank equation, or a derivative of it. The boundary conditions define the concentration or flux on the boundary of the domain of interest. These usually represent the interface of the solution with a surface or the bulk solution. The initial conditions describe an initial guess at a solution for a steady state simulation or the conditions at time = 0 for a time dependent simulation. From the numerical solution the flux of active species to an electrode can be used to calculate the current at an electrode. This current can then be compared to experimental results.

FEM simulations are complicated and the commercial software packages take FEM simulations (geometry, mass transport equations, boundary and initial conditions) and compute solutions. It is important to check that the solution makes sense, as the software produces a numerical approximation. This approximation may contain numerical errors, or there may be multiple solutions to the problem of which only one is physically possible.

1.4 Aims of Thesis

This thesis is concerned with developing new EC-SPM techniques and then applying these to biologically problems. The new EC-SPM techniques address one of two problems: i) how to position a EC-SPM probe close to the surface in a controlled and measurable manner without crashing the probe into the surface; and/or ii) how to measure different electrochemical signals in an EC-SPM configuration to enhance the information content.

Chapter 2 introduces the IC-SECM technique, which is a new EC-SPM probe positioning technique that uses the physical interaction of the probe with the surface to determine the tip-surface distance and so address the first problem. Chapter 3 shows the application of IC-SECM to the quantitative measurement of fluid flow through a porous biological membrane, dentin.

Chapter 4 shows how SECM can be used to assess an interesting biological problem, namely photosynthesis. FEM simulation were used to analyse and quantify the electrochemical measurements.

In order to develop advanced EC-SPM techniques, a series of new EC-SPM instruments were built to run the new EC-SPM techniques (SECCM, SICM-SECM, etc.) and accommodate new users. Chapter 5 describes the hardware and software of these new instruments.

The new EC-SPM instruments were used with a new dual electrode probe in Chapter 6 and, finally, SECCM was expanded to fabricate nanoscale patterns on surfaces in Chapter 7.

References

[1] Bard, A. J.; Larry R. Faulkner, *Electrochemical Methods*; John Wiley & Sons, 2001.

[2] Heinze, J. *Angew. Chem. Int. Edit.* **1993**, *32*, 1268–1288.

[3] Amatore, C.; Pebay, C.; Thouin, L.; Wang, A.; Warkocz, J.-S. *Anal. Chem.* **2010**, *82*, 6933–6939.

[4] Arrigan, D. W. M. *Analyst* **2004**, *129*, 1157–1165.

[5] Cox, J. T.; Zhang, B. *Ann. Rev. Anal. Chem.* **2012**, *5*, 253–272.

[6] Watkins, J. J.; Zhang, B.; White, H. S. *J. Chem. Edu.* **2005**, *82*, 712–719.

[7] Li, Y.; Bergman, D.; Zhang, B. *Anal. Chem.* **2009**, *81*, 5496–5502.

[8] Zhang, B.; Galusha, J.; Shiozawa, P. G.; Wang, G.; Bergren, A. J.; Jones, R. M.; White, R. J.; Ervin, E. N.; Cauley, C. C.; White, H. S. *Anal. Chem.* **2007**, *79*, 4778–4787.

[9] Zuliani, C.; Walsh, D. A.; Keyes, T. E.; Forster, R. J. *Anal. Chem.* **2010**, *82*, 7135–7140.

[10] Mezour, M. A.; Morin, M.; Mauzeroll, J. *Anal. Chem.* **2011**, *83*, 2378–2382.

[11] Bonazza, H. L.; Fernández, J. L. *J. Electroanal. Chem.* **2010**, *650*, 75–81.

[12] Nogala, W.; Velmurugan, J.; Mirkin, M. V. *Anal. Chem.* **2012**, *84*, 5192–5197.

[13] Elsamadisi, P.; Wang, Y.; Velmurugan, J.; Mirkin, M. V. *Anal. Chem.* **2011**, *83*, 671–673.

[14] Chang, J.; Leonard, K. C.; Cho, S. K.; Bard, A. J. *Anal. Chem.* **2012**, *84*, 5159–5163.

[15] Wehmeyer, K. R.; Wightman, R. M. *J. Electroanal. Chem.* **1985**, *196*, 417–421.

[16] Basha, C. A.; Rajendran, L. *Int. J. Electrochem. Sci.* **2006**, *1*, 268–282.

[17] Mirkin, M. V.; Bard, A. J. *Anal. Chem.* **1992**, *64*, 2293–2302.

[18] Sun, P.; Mirkin, M. V. *Anal. Chem.* **2006**, *78*, 6526–6534.

[19] Wipf, D. O.; Kristensen, E. W.; Deakin, M. R.; Wightman, R. M. *Anal. Chem.* **1988**, *60*, 306–310.

[20] Wipf, D. O.; Michael, A. C.; Wightman, R. M. *J. Electroanal. Chem.* **1989**, *269*, 15–25.

[21] Wipf, D. O.; Wightman, R. M. *J. Phys. Chem.* **1989**, *93*, 4286–4291.

[22] Kwon, S. J.; Fan, F.-R. F.; Bard, A. J. *J. Am. Chem. Soc.* **2010**, *132*, 13165–13167.

[23] Bard, A. J.; Mirkin, M. V.; Unwin, P. R.; Wipf, D. O. *J. Phys. Chem.* **1992**, *96*, 1861–1868.

[24] Aoki, K.; Osteryoung, J. *J. Electroanal. Chem.* **1981**, *122*, 19–35.

[25] Bruckenstein, S.; Janiszewska, J. *J.Electroanal. Chem.* **2002**, *538-539*, 3–12.

[26] Menshykau, D.; Javier del Campo, F.; Muñoz, F. X.; Compton, R. G. *Sensors Actuat. B-Chem.* **2009**, *138*, 362–367.

[27] He, R.; Chen, S.; Yang, F.; Wu, B. *J. Phys. Chem. B* **2006**, *110*, 3262–3270.

[28] Lavacchi, A.; Bardi, U.; Borri, C.; Caporali, S.; Fossati, A.; Perissi, I. *J. Appl. Electrochem.* **2009**, *39*, 2159–2163.

[29] Molina, A.; Gonzalez, J.; Henstridge, M. C.; Compton, R. G. *J. Phys. Chem. C* **2011**, *115*, 4054–4062.

[30] Binnig, G.; Quate, C. F.; Gerber, C. *Phys. Rev. Lett.* **1986**, *56*, 930–933.

[31] Amemiya, S.; Bard, A. J.; Fan, F.-R. F.; Mirkin, M. V.; Unwin, P. R. *Ann. Rev. Anal. Chem.* **2008**, *1*, 95–131.

[32] Bard, A. J.; Mirkin, M. V. *Scanning Electrochemical Microscopy*; Marcel Dekker Inc: New York, 2001.

[33] Edwards, M. A.; Martin, S.; Whitworth, A. L.; Macpherson, J. V.; Unwin, P. R. *Physiol. Meas.* **2006**, *27*, R63–108.

[34] Mirkin, M. V. *Anal. Chem.* **1996**, *68*, 177A–182A.

[35] Mirkin, M. V.; Nogala, W.; Velmurugan, J.; Wang, Y. *Phys. Chem. Chem. Phys.* **2011**, *13*, 21196–21212.

[36] Sun, P.; Laforge, F. O.; Mirkin, M. V. *Phys. Chem. Chem. Phys.* **2007**, *9*, 802–823.

[37] Bard, A. J.; Fan, F.-r. F.; Kwak, J.; Lev, O. *Anal. Chem.* **1989**, *61*, 132–138.

[38] Kwak, J.; Bard, A. J. *Anal. Chem.* **1989**, *61*, 1221–1227.

[39] Kwak, J.; Bard, A. J. *Anal. Chem.* **1989**, *61*, 1794–1799.

[40] Bard, A. J.; Denuault, G.; Lee, C.; Mandler, D.; Wipf, D. O. *Acc. Chem. Res.* **1990**, *23*, 357–363.

[41] Bard, A. J.; Fan, F.-R. R.; Pierce, D. T.; Unwin, P. R.; Wipf, D. O.; Zhou, F. *Science* **1991**, *254*, 68–74.

[42] Velmurugan, J.; Sun, P.; Mirkin, M. V. *J. Phys. Chem. C* **2009**, *113*, 459–464.

[43] Izquierdo, J.; Nagy, L.; Varga, A.; Bitter, I.; Nagy, G.; Souto, R. M. *Electrochim. Acta* **2012**, *59*, 398–403.

[44] Gyurcsányi, R. E.; Pergel, E.; Nagy, R.; Kapui, I.; Lan, B. T.; Tóth, K.; Bitter, I.; Lindner, E. *Anal. Chem.* **2001**, *73*, 2104–2011.

[45] Ishimatsu, R.; Kim, J.; Jing, P.; Striemer, C. C.; Fang, D. Z.; Fauchet, P. M.; McGrath, J. L.; Amemiya, S. *Anal. Chem.* **2010**, *82*, 7127–7134.

[46] Varga, A.; Nagy, L.; Izquierdo, J.; Bitter, I.; Souto, R. M.; Nagy, G. *Anal. Lett.* **2011**, *44*, 2876–2886.

[47] Shen, M.; Ishimatsu, R.; Kim, J.; Amemiya, S. *J. Am. Chem. Soc.* **2012**, *134*, 9856–9859.

[48] Kimmel, D. W.; LeBlanc, G.; Meschievitz, M. E.; Cliffel, D. E. *Anal. Chem.* **2012**, *84*, 685–707.

[49] Izquierdo, J.; Nagy, L.; Santana, J. J.; Nagy, G.; Souto, R. M. *Electrochim. Acta* **2011**, *58*, 707–716.

[50] Kang, J.; Yang, Y.; Jiang, F.; Shao, H. *Surf. Interface Anal.* **2007**, *39*, 877–884.

[51] Lamaka, S.; Taryba, M.; Montemor, M.; Isaacs, H.; Ferreira, M. *Electrochem. Commun.* **2011**, *13*, 20–23.

[52] Lesch, A.; Momotenko, D.; Cortés-Salazar, F.; Wirth, I.; Tefashe, U. M.; Meiners, F.; Vaske, B.; Girault, H. H.; Wittstock, G. *J. Electroanal. Chem.* **2012**, *666*, 52–61.

[53] Cortés-Salazar, F.; Momotenko, D.; Lesch, A.; Wittstock, G.; Girault, H. H. *Anal. Chem.* **2010**, *82*, 10037–10044.

[54] Cortes-Salazar, F.; Momotenko, D.; Girault, H. H.; Lesch, A.; Wittstock, G. *Anal. Chem.* **2011**, *83*, 1493–1499.

[55] Sun, P.; Mirkin, M. V. *Anal. Chem.* **2007**, *79*, 5809–5816.

[56] Gray, N. J.; Unwin, P. R. *Analyst* **2000**, *125*, 889–893.

[57] Schulte, A.; Schuhmann, W. *Angew. Chem. Int. Edit.* **2007**, *46*, 8760–8777.

[58] Slowinska, K.; Feldberg, S. W.; Majda, M. *J. Electroanal. Chem.* **2003**, *554-555*, 61–69.

[59] Horrocks, B. R.; Mirkin, M. V.; Pierce, D. T.; Bard, A. J. *Anal. Chem.* **1993**, *65*, 1213–1224.

[60] Stoica, L.; Neugebauer, S.; Schuhmann, W. *Adv. Biochem. Engin/Biotechnol.* **2008**, *109*, 455–492.

[61] McGeouch, C.-A.; Peruffo, M.; Edwards, M. A.; Bindley, L. A.; Lazenby, R. A.; Mbogoro, M. M.; McKelvey, K.; Unwin, P. R. *J. Phys. Chem. C* **2012**, *116*, 14892–14899.

[62] Rudd, N. C.; Cannan, S.; Bitziou, E.; Ciani, I.; Whitworth, A. L.; Unwin, P. R. *Anal. Chem.* **2005**, *77*, 6205–6217.

[63] Oleinick, A. I.; Battistel, D.; Daniele, S.; Svir, I.; Amatore, C. *Anal. Chem.* **2011**, *83*, 4887–4893.

[64] Cannan, S.; Cervera, J.; Steliaros, R. J.; Bitziou, E.; Whitworth, A. L.; Unwin, P. R. *Phys. Chem. Chem. Phys.* **2011**, *13*, 5403–5412.

[65] Zeradjanin, A. R.; Schilling, T.; Seisel, S.; Bron, M.; Schuhmann, W. *Anal. Chem.* **2011**, *83*, 7645–7650.

[66] Fonseca, S. M.; Barker, A. L.; Ahmed, S.; Kemp, T. J.; Unwin, P. R. *Chem. Comm.* **2003**, 1002–1003.

[67] Borgwarth, K.; Ricken, C.; Ebling, D. G.; Heinze, J. *Fresenius J Anal Chem* **1996**, *356*, 288–294.

[68] Choi, W.-H.; Papautsky, I. *J. Micro-Nanolith. Mem.* **2011**, *10*, 020501–020501–3.

[69] Cornut, R.; Poirier, S.; Mauzeroll, J. *Anal. Chem.* **2012**, *84*, 3531–3537.

[70] Mirkin, M. V.; Fan, F.-R. F.; Bard, A. J. *J. Electroanal. Chem.* **1992**, *328*, 47–62.

[71] Amphlett, J. L.; Denuault, G. *J. Phys. Chem. B* **1998**, *102*, 9946–9951.

[72] Cornut, R.; Griveau, S.; Lefrou, C. *J. Electroanal. Chem.* **2010**, *650*, 55–61.

[73] Wei, C.; Bard, A. J.; Mirkin, M. V. *J. Phys. Chem.* **1995**, *99*, 16033–16042.

[74] Mandler, D.; Bard, A. J. *J. Electrochem. Soc.* **1989**, *136*, 3143–3144.

[75] Mirkin, M. V. *Mikrochim. Acta* **1999**, *130*, 127–153.

[76] Wittstock, G.; Burchardt, M.; Pust, S. E.; Shen, Y.; Zhao, C. *Angew. Chem. Int. Edit.* **2007**, *46*, 1584–1617.

[77] Nioradze, N.; Kim, J.; Amemiya, S. *Anal. Chem.* **2011**, *83*, 828–835.

[78] D'iaz-Ballote, L.; Alpuche-Aviles, M. A.; Wipf, D. O. *J. Electroanal. Chem.* **2007**, *604*, 17–25.

[79] Shao, Y.; Mirkin, M. V. *J. Phys. Chem. B* **1998**, *102*, 9915–9921.

[80] Zigah, D.; Noel, J.-M.; Lagrost, C.; Hapiot, P. *J. Phys. Chem. C* **2010**, *114*, 3075–3081.

[81] Zhang, J.; Barker, A. L.; Mandler, D.; Unwin, P. R. *J. Am. Chem. Soc.* **2003**, *125*, 9312–9313.

[82] Mandler, D.; Unwin, P. R. *J. Phys. Chem. B* **2003**, *107*, 407–410.

[83] Tsionsky, M.; Zhou, J.; Amemiya, S.; Fan, F.-R. F.; Bard, A. J.; Dryfe, R. A. W. *Anal. Chem.* **1999**, *71*, 4300–4305.

[84] Bertoncello, P.; Ciani, I.; Li, F.; Unwin, P. R. *Langmuir* **2006**, *22*, 10380–10388.

[85] Noël, J.-M.; Latus, A.; Lagrost, C.; Volanschi, E.; Hapiot, P. *J. Am. Chem. Soc.* **2012**, *134*, 2835–2841.

[86] Mengesha Tefashe, U.; Nonomura, K.; Vlachopoulos, N.; Hagfeldt, A.; Wittstock, G. *J. Phys. Chem. C* **2012**, *116*, 4316–4323.

[87] Duarte, R. G.; González, S.; Castela, A. S.; Ferreira, M. G.; Souto, R. M. *Prog. Org. Coat.* **2012**, *74*, 365–370.

[88] González, S.; Santana, J. J.; González-García, Y.; Fernández-Mérida, L.; Souto, R. M. *Corros. Sci.* **2011**, *53*, 1910–1915.

[89] Izquierdo, J.; Santana, J. J.; González, S.; Souto, R. M. *Electrochim. Acta* **2010**, *55*, 8791–8800.

[90] Leiva-García, R.; Akid, R.; Greenfield, D.; Gittens, J.; Muñoz Portero, M.; García-Antón, J. *Electrochim. Acta* **2012**, *70*, 105–111.

[91] Sánchez-Sánchez, C.; Souza-Garcia, J.; Sáez, A.; Montiel, V.; Herrero, E.; Aldaz, A.; Feliu, J. *Electrochim. Acta* **2011**, *56*, 10708–10712.

[92] Sidane, D.; Devos, O.; Puiggali, M.; Touzet, M.; Tribollet, B.; Vivier, V. *Electrochem. Commun.* **2011**, *13*, 1361–1364.

[93] Kim, J.; Xiong, H.; Hofmann, M.; Kong, J.; Amemiya, S. *Anal. Chem.* **2010**, *82*, 1605–1607.

[94] Lee, S.; Zhang, Y.; White, H. S.; Harrell, C. C.; Martin, C. R. *Anal. Chem.* **2004**, *76*, 6108–6115.

[95] Malel, E.; Colleran, J.; Mandler, D. *Electrochim. Acta* **2011**, *56*, 6954–6961.

[96] Neufeld, A. K.; O'Mullane, A. P. *J. Solid State Electr.* **2006**, *10*, 808–816.

[97] Scott, E. R.; White, H. S.; Phipps, J. B. *J. Mem. Sci.* **1991**, *58*, 71–87.

[98] Uitto, O. D.; White, H. S.; Aoki, K. *Anal. Chem.* **2002**, *74*, 4577–4582.

[99] Nugues, S.; Denuault, G. *J. Electroanal. Chem.* **1996**, *408*, 125–140.

[100] Macpherson, J. V.; Unwin, P. R. *Electroanal.* **2005**, *17*, 197–204.

[101] Cornut, R.; Nunige, S.; Lefrou, C.; Kanoufi, F. *Electrochim. Acta* **2011**, *56*, 10701–10707.

[102] Oltra, R.; Zimmer, A.; Sorriano, C.; Rechou, F.; Borkowski, C.; Néel, O. *Electrochim. Acta* **2011**, *56*, 7038–7044.

[103] Wilhelm, T.; Wittstock, G. *Langmuir* **2002**, *18*, 9485–9493.

[104] Roberts, W. S.; Davis, F.; Collyer, S. D.; Higson, S. P. J. *Analyst* **2011**, *136*, 5287–5293.

[105] Ku, S.-Y.; Wong, K.-T.; Bard, A. J. *J. Am. Chem. Soc.* **2008**, *130*, 2392–2393.

[106] Wittstock, G.; Hesse, R.; Schuhmann, W. *Electroanal.* **1997**, *9*, 746–750.

[107] Sheffer, M.; Mandler, D. *J. Electrochem. Soc.* **2008**, *155*, D203.

[108] Zhou, J.; Wipf, D. O. *J. Electrochem. Soc.* **1997**, *144*, 1202–1207.

[109] Yasukawa, T.; Kaya, T.; Matsue, T. *Electroanal.* **2000**, *12*, 653–659.

[110] Schulte, A.; Nebel, M.; Schuhmann, W. *Ann. Rev. Anal. Chem.* **2010**, *3*, 299–318.

[111] Gyurcsányi, R. E.; Jágerszki, G.; Kiss, G.; Tóth, K. *Bioelectrochem.* **2004**, *63*, 207–215.

[112] Kranz, C.; Wiedemair, J. *Anal. Bioanal.Chem.* **2008**, *390*, 239–243.

[113] Abe, H. *J. Mamm. Ova Res.* **2007**, *24*, 70–78.

[114] Kaya, T.; Numai, D.; Nagamine, K.; Aoyagi, S.; Shiku, H.; Matsue, T. *Analyst* **2004**, *129*, 529–534.

[115] Bard, A. J.; Li, X.; Zhan, W. *Biosens. Bioelectron.* **2006**, *22*, 461–472.

[116] Beaulieu, I.; Kuss, S.; Mauzeroll, J.; Geissler, M. *Anal. Chem.* **2011**, *83*, 1485–1492.

[117] Kovarik, M. L.; Allbritton, N. L. *Trends Biotechnol.* **2011**, *29*, 222–230.

[118] Scott, E. R.; Phipps, J. B.; White, H. S. *J. Invest. Dermatol.* **1995**, *104*, 142–145.

[119] Bath, B. D.; White, H. S.; Scott, E. R. *Pharm. Res.* **2000**, *17*, 471–475.

[120] Gonsalves, M.; Barker, A. L.; Macpherson, J. V.; Unwin, P. R.; OHare, D.; Winlove, C. P. *Biophys. J.* **2000**, *78*, 1578–1588.

[121] Wijayawardhana, C. A.; Wittstock, G.; Halsall, H. B.; Heineman, W. R. *Anal. Chem.* **2000**, *72*, 333–338.

[122] Zhan, W.; Bard, A. J. *Anal. Chem.* **2006**, *78*, 726–733.

[123] Kim, E.; Xiong, H.; Striemer, C. C.; Fang, D. Z.; Fauchet, P. M.; McGrath, J. L.; Amemiya, S. *J. Am. Chem. Soc.* **2008**, *130*, 4230–4231.

[124] Koley, D.; Bard, A. J. *Proc. Natl. Acad. Sci. USA* **2010**, *107*, 16783–16787.

[125] Zhang, M.; Girault, H. H. *Analyst* **2009**, *134*, 25–30.

[126] Qin, G.; Zhang, M.; Zhang, T.; Zhang, Y.; McIntosh, M.; Li, X.; Zhang, X. *Electroanal.* **2012**, *24*, 1027–1032.

[127] Xue, Y.; Ding, L.; Lei, J.; Yan, F.; Ju, H. *Anal. Chem.* **2010**, *82*, 7112–7118.

[128] Zhang, B.; Heien, M. L. a. V.; Santillo, M. F.; Mellander, L.; Ewing, A. G. *Anal. Chem.* **2011**, *83*, 571–577.

[129] Bergner, S.; Wegener, J.; Matysik, F.-M. *Anal. Chem.* **2011**, *83*, 169–174.

[130] Koley, D.; Bard, A. J. *Proc. Natl. Acad. Sci. USA* **2012**, *109*, 11522–11527.

[131] Takahashi, Y.; Shevchuk, A. I.; Novak, P.; Babakinejad, B.; Macpherson, J. V.; Unwin, P. R.; Shiku, H.; Gorelik, J.; Klenerman, D.; Korchev, Y. E.; Matsue, T. *Proc. Natl. Acad. Sci. USA* **2012**, *109*, 11540–11545.

[132] Zhang, M. M.-N.; Long, Y.-T.; Ding, Z. *Chem. Cent. J.* **2012**, *6*, 20.

[133] Kurulugama, R. T.; Wipf, D. O.; Takacs, S. A.; Pongmayteegul, S.; Garris, P. A.; Baur, J. E. *Anal. Chem.* **2005**, *77*, 1111–1117.

[134] Shiku, H.; Shiraishi, T.; Ohya, H.; Matsue, T.; Abe, H.; Hoshi, H.; Kobayashi, M. *Anal. Chem.* **2001**, *73*, 3751–3758.

[135] Yasukawa, T.; Uchida, I.; Matsue, T. *Biophys. J.* **1999**, *76*, 1129–1135.

[136] Zhu, R.; Macfie, S. M.; Ding, Z. *Langmuir* **2008**, *24*, 14261–14268.

[137] Uchida, I.; Abe, T.; Itabashi, T.; Matsue, T. *Chem. Lett.* **1990**, 1227–1230.

[138] Matsue, T.; Koike, S.; Uchida, I. *Biochem. Bioph. Res. Comm.* **1993**, *197*, 1283–1287.

[139] Alpuche-Aviles, M. A.; Wipf, D. O. *Anal. Chem.* **2001**, *73*, 4873–4881.

[140] Eckhard, K.; Schuhmann, W. *Analyst* **2008**, *133*, 1486–1497.

[141] Gabrielli, C.; Huet, F.; Keddam, M.; Rousseau, P.; Vivier, V. *J. Phys. Chem. B* **2004**, *108*, 11620–11626.

[142] Ervin, E. N.; White, H. S.; Baker, L. A. *Anal. Chem.* **2005**, *77*, 5564–5569.

[143] Ervin, E. N.; White, H. S.; Baker, L. A.; Martin, C. R. *Anal. Chem.* **2006**, *78*, 6535–6541.

[144] Diakowski, P. M.; Ding, Z. *Phys. Chem. Chem. Phys.* **2007**, *9*, 5966–5974.

[145] Ruhlig, D.; Gugel, H.; Schulte, A.; Theisen, W.; Schuhmann, W. *Analyst* **2008**, *133*, 1700–1706.

[146] Souto, R. M.; Socas, B.; Izquierdo, J.; Santana, J. J.; González, S. *Prog. Org. Coat.* **2012**, *74*, 371–375.

[147] Eckhard, K.; Erichsen, T.; Stratmann, M.; Schuhmann, W. *Chem. Eur. J.* **2008**, *14*, 3968–3976.

[148] Senoz, C.; Maljusch, A.; Rohwerder, M.; Schuhmann, W. *Electroanal.* **2012**, *24*, 239–245.

[149] Wipf, D. O.; Bard, A. J. *Anal. Chem.* **1992**, *64*, 1362–1367.

[150] Unwin, P. R.; Edwards, M. A.; Whitworth, A. L. *Anal. Chem.* **2011**, *83*, 1977–1984.

[151] Wipf, D. O.; Bard, A. J.; Tallman, D. E. *Anal. Chem.* **1993**, *65*, 1373–1377.

[152] Ludwig, M.; Kranz, C.; Schuhmann, W.; Gaub, H. E. *Revi. Sci. Instru.* **1995**, *66*, 2857–2860.

[153] Karrai, K.; Grober, R. D. *Appl. Phys. Lett.* **1995**, *66*, 1842–1844.

[154] Katemann, B. B.; Schuhmann, W. *Electroanal.* **2002**, *14*, 22–28.

[155] Tefashe, U. M.; Wittstock, G. *CR Chim.* **2012**, 1–8.

[156] Lee, Y.; Ding, Z.; Bard, A. J. *Anal. Chem.* **2002**, *74*, 3634–3643.

[157] Katemann, B. B.; Schulte, A.; Schuhmann, W. *Chem. Eur. J.* **2003**, *9*, 2025–2033.

[158] Takahashi, Y.; Hirano, Y.; Yasukawa, T.; Shiku, H.; Yamada, H.; Matsue, T. *Langmuir* **2006**, *22*, 10299–10306.

[159] Nebel, M.; Eckhard, K.; Erichsen, T.; Schulte, A.; Schuhmann, W. *Anal. Chem.* **2010**, *82*, 7842–7848.

[160] Takahashi, Y.; Shiku, H.; Murata, T.; Yasukawa, T.; Matsue, T. *Anal. Chem.* **2009**, *81*, 9674–9681.

[161] Yamada, H.; Fukumoto, H.; Yokoyama, T.; Koike, T. *Anal. Chem.* **2005**, *77*, 1785–1790.

[162] Macpherson, J. V.; Unwin, P. R. *Anal. Chem.* **2000**, *72*, 276–285.

[163] Rodriguez, R. D.; Anne, A.; Cambril, E.; Demaille, C. *Ultramicroscopy* **2011**, *111*, 973–981.

[164] Kranz, C.; Friedbacher, G.; Mizaikoff, B.; Lugstein, A.; Smoliner, J.; Bertagnolli, E. *Anal. Chem.* **2001**, *73*, 2491–2500.

[165] Wain, A. J.; Cox, D.; Zhou, S.; Turnbull, A. *Electrochem. Commun.* **2011**, *13*, 78–81.

[166] Dobson, P. S.; Weaver, J. M. R.; Burt, D. P.; Holder, M. N.; Wilson, N. R.; Unwin, P. R.; Macpherson, J. V. *Phys. Chem. Chem. Phys.* **2006**, *8*, 3909–3914.

[167] Dobson, P. S.; Weaver, J. M. R.; Holder, M. N.; Unwin, P. R.; Macpherson, J. V. *Anal. Chem.* **2005**, *77*, 424–434.

[168] Macpherson, J. V.; Unwin, P. R. *Anal. Chem.* **2001**, *73*, 550–557.

[169] Kueng, A.; Kranz, C.; Lugstein, A.; Bertagnolli, E.; Mizaikoff, B. *Angew. Chem. Int. Edit.* **2003**, *42*, 3238–3240.

[170] Holder, M. N.; Gardner, C. E.; Macpherson, J. V.; Unwin, P. R. *J. Electroanal. Chem.* **2005**, *585*, 8–18.

[171] Leonhardt, K.; Avdic, A.; Lugstein, A.; Pobelov, I.; Wandlowski, T.; Wu, M.; Gollas, B.; Denuault, G. *Anal. Chem.* **2011**, *83*, 2971–2977.

[172] Pust, S. E.; Salomo, M.; Oesterschulze, E.; Wittstock, G. *Nanotechnology* **2010**, *21*, 105709.

[173] Macpherson, J. V.; Jones, C. E.; Barker, A. L.; Unwin, P. R. *Anal. Chem.* **2002**, *74*, 1841–1848.

[174] Gardner, C. E.; Unwin, P. R.; Macpherson, J. V. *Electrochem. Commun.* **2005**, *7*, 612–618.

[175] Anne, A.; Chovin, A.; Demaille, C.; Lafouresse, M. *Anal. Chem.* **2011**, *83*, 7924–7932.

[176] Barnes, E. O.; Lewis, G. E. M.; Dale, S. E. C.; Marken, F.; Compton, R. G. *Analyst* **2012**, *137*, 1068–1081.

[177] Zhong, M.; Zhou, J.; Lunte, S. M.; Zhao, G.; Giolando, D. M.; Kirchhoff, J. R. *Anal. Chem.* **1996**, *68*, 203–207.

[178] Matysik, F.-M. *Electrochim. Acta* **1997**, *42*, 3113–3116.

[179] Gao, N.; Lin, X.; Jia, W.; Zhang, X.; Jin, W. *Talanta* **2007**, *73*, 589–593.

[180] Yang, C.; Sun, P. *Anal. Chem.* **2009**, *81*, 7496–7500.

[181] Liljeroth, P.; Johans, C.; Slevin, C. J.; Quinn, B. M.; Kontturi, K. *Electrochem. Commun.* **2002**, *4*, 67–71.

[182] Fushimi, K.; Matsushita, K.-i.; Hasegawa, Y. *Electrochim. Acta* **2011**, *56*, 9602–9608.

[183] Isik, S.; Etienne, M.; Oni, J.; Blöchl, A.; Reiter, S.; Schuhmann, W. *Anal. Chem.* **2004**, *76*, 6389–6394.

[184] Yasukawa, T.; Kaya, T.; Matsue, T. *Anal. Chem.* **1999**, *71*, 4637–4641.

[185] Chen, C.-c.; Zhou, Y.; Baker, L. A. *Ann. Rev. Anal. Chem.* **2012**, *5*, 207–228.

[186] Chen, C.-C.; Baker, L. A. *Analyst* **2011**, *136*, 90–97.

[187] Edwards, M. A.; Williams, C. G.; Whitworth, A. L.; Unwin, P. R. *Anal. Chem.* **2009**, *81*, 4482–4492.

[188] Pastré, D.; Iwamoto, H.; Liu, J.; Szabo, G.; Shao, Z. *Ultramicroscopy* **2001**, *90*, 13–9.

[189] Shevchuk, A. I.; Gorelik, J.; Harding, S. E.; Lab, M. J.; Klenerman, D.; Korchev, Y. E. *Biophys. J.* **2001**, *81*, 1759–1764.

[190] Takahashi, Y.; Murakami, Y.; Nagamine, K.; Shiku, H.; Aoyagi, S.; Yasukawa, T.; Kanzaki, M.; Matsue, T. *Phys. Chem. Chem. Phys.* **2010**, *12*, 10012–10017.

[191] Novak, P.; Li, C.; Shevchuk, A. I.; Stepanyan, R.; Caldwell, M.; Hughes, S.; Smart, T. G.; Gorelik, J.; Ostanin, V. P.; Lab, M. J.; Moss, G. W. J.; Frolenkov, G. I.; Klenerman, D.; Korchev, Y. E. *Nat. Methods* **2009**, *6*, 279–281.

[192] Klenerman, D.; Korchev, Y. E.; Davis, S. J. *Curr. Opin. Chem. Biol.* **2011**, *15*, 1–8.

[193] Morris, C. A.; Friedman, A. K.; Baker, L. A. *Analyst* **2010**, *135*, 2190–2202.

[194] Lan, W.-J.; Holden, D. A.; Zhang, B.; White, H. S. *Anal. Chem.* **2011**, *83*, 3840–3847.

[195] Yang, X.; Liu, X.; Zhang, X.; Lu, H.; Zhang, J.; Zhang, Y. *Ultramicroscopy* **2011**, *111*, 1417–1422.

[196] Bruckbauer, A.; James, P.; Zhou, D.; Yoon, J. W.; Excell, D.; Korchev, Y.; Jones, R.; Klenerman, D. *Biophys. J.* **2007**, *93*, 3120–3131.

[197] Chen, C.-C.; Derylo, M. A.; Baker, L. A. *Anal. Chem.* **2009**, *81*, 4742–4751.

[198] Chen, C.-C.; Zhou, Y.; Baker, L. A. *ACS Nano* **2011**, *5*, 8404–8411.

[199] Steinbock, L. J.; Otto, O.; Chimerel, C.; Gornall, J.; Keyser, U. F. *Nano Lett.* **2010**, *10*, 2493–2497.

[200] Takahashi, Y.; Shevchuk, A. I.; Novak, P.; Murakami, Y.; Shiku, H.; Korchev, Y. E.; Matsue, T. *J. Am. Chem. Soc.* **2010**, *132*, 10118–10126.

[201] Comstock, D. J.; Elam, J. W.; Pellin, M. J.; Hersam, M. C. *Anal. Chem.* **2010**, *82*, 1270–1276.

[202] Morris, C. A.; Chen, C.-C.; Baker, L. A. *Analyst* **2012**, *137*, 2933–2938.

[203] Takahashi, Y.; Shevchuk, A. I.; Novak, P.; Zhang, Y.; Ebejer, N.; Macpherson, J. V.; Unwin, P. R.; Pollard, A. J.; Roy, D. D.; Clifford, C. A.; Shiku, H.; Matsue, T.; Klenerman, D.; Korchev, Y. E. *Angew. Chem. Int. Edit.* **2011**, *50*, 9638–9642.

[204] Takahashi, Y.; Miyamoto, T.; Shiku, H.; Ino, K.; Yasukawa, T.; Asano, R.; Kumagai, I.; Matsue, T. *Phys. Chem. Chem. Phys.* **2011**, *13*, 16569–16573.

[205] Williams, C. G.; Edwards, M. A.; Colley, A. L.; Macpherson, J. V.; Unwin, P. R. *Anal. Chem.* **2009**, *81*, 2486–2495.

[206] Yang, D.; Han, L.; Yang, Y.; Zhao, L.-B.; Zong, C.; Huang, Y.-F.; Zhan, D.; Tian, Z.-Q. *Angew. Chem. Int. Edit.* **2011**, *50*, 8679–8682.

[207] Zhan, D.; Yang, D.; Zhu, Y.; Wu, X.; Tian, Z.-Q. *Chem. Comm.* **2012**, *48*, 11449–11451.

[208] Rodolfa, K. T.; Bruckbauer, A.; Zhou, D.; Korchev, Y. E.; Klenerman, D. *Angew. Chem. Int. Edit.* **2005**, *44*, 6854–6859.

[209] Rodolfa, K. T.; Bruckbauer, A.; Zhou, D.; Schevchuk, A. I.; Korchev, Y. E.; Klenerman, D. *Nano Lett.* **2006**, *6*, 252–257.

[210] Ebejer, N.; Schnippering, M.; Colburn, A. W.; Edwards, M. A.; Unwin, P. R. *Anal. Chem.* **2010**, *82*, 9141–9145.

[211] Snowden, M. E.; Güell, A. G.; Lai, S. C. S.; McKelvey, K.; Ebejer, N.; O'Connell, M. A.; Colburn, A. W.; Unwin, P. R. *Anal. Chem.* **2012**, *84*, 2483–2491.

[212] Lai, S. C. S.; Dudin, P. V.; Macpherson, J. V.; Unwin, P. R. *J. Am. Chem. Soc.* **2011**, *122*, 10744–10747.

[213] Güell, A. G.; Ebejer, N.; Snowden, M. E.; Macpherson, J. V.; Unwin, P. R. *J. Am. Chem. Soc.* **2012**, *134*, 7258–7261.

[214] Güell, A. G.; Ebejer, N.; Snowden, M. E.; McKelvey, K.; Macpherson, J. V.; Unwin, P. R. *Proc. Natl. Acad. Sci. USA* **2012**, *109*, 11487–11492.

[215] Laslau, C.; Williams, D. E.; Kannan, B.; Travas-Sejdic, J. *Adv. Funct. Mater.* **2011**, *21*, 4607–4616.

[216] Patten, H. V.; Meadows, K. E.; Hutton, L. A.; Iacobini, J. G.; Battistel, D.; McKelvey, K.; Colburn, A. W.; Newton, M. E.; Macpherson, J. V.; Unwin, P. R. *Angew. Chem. Int. Edit.* **2012**, *51*, 7002–7006.

Chapter 2

Intermittent Contact - Scanning Electrochemical Microscopy (IC-SECM): A New Approach for Tip Positioning and Simultaneous Imaging of Interfacial Topography and Activity

IC-SECM is a new SECM probe positioning technique. The probe is oscillated normal to a surface and the damping of the oscillation, caused by the physical interaction of the probe with the surface, is detected and used to measure the probe-surface distance. The initial idea for IC-SECM came from observations of the probe oscillation amplitude during studies of TPM-SECM by Martin Edwards.

This chapter contains the initial paper describing IC-SECM. I was responsible for data collection, analysis and the paper preparation. Martin Edwards contributed to the instrumentation, and the work built on his original observations.

Intermittent Contact - Scanning Electrochemical Microscopy (IC-SECM): A New Approach for Tip Positioning and Simultaneous Imaging of Interfacial Topography and Activity

Kim McKelvey, Martin A. Edwards and Patrick R. Unwin

Anal. Chem., 2010, 82(15), 6334 - 6337.

2.1 Abstract

A new SECM tip positioning method that allows surface topography and activity to be resolved simultaneously and independently is presented. The tip, controlled by a piezoelectric positioner operated in closed loop, is oscillated normal to the substrate surface. Changes in the oscillation amplitude, caused by the intermittent contact (IC) of the tip with the substrate surface, are used as a feedback signal to control the tip height. The method is illustrated with amperometric feedback approach curve measurements to inert (insulating) and active (conducting) substrates using 12.5 μm and 1 μm radius Pt disk electrodes. Imaging of gold bands on a glass substrate demonstrates the capabilities for simultaneous topography and activity mapping. The prospect for using IC methodology more widely with other types of tips is highlighted briefly.

2.2 Introduction

Scanning electrochemical microscopy (SECM) is a scanned probe microscopy technique in which the electrochemical response of a mobile ultramicroelectrode (UME) tip is used to provide information on the properties (e.g. topography or chemical activity) of an interface or phase.[1–4] Despite the tremendous impact of SECM in interfacial science,[5] a significant - and generally unresolved - challenge concerns absolute tip positioning, for example during approach curve measurements.[6] For SECM imaging there is a need for methods which allow topography and surface flux (or activity) information to be determined unambiguously. This paper describes a new and simple approach for both tip positioning and SECM imaging which addresses this challenge.

Conventional amperometric SECM (which forms the overwhelming majority of applications) typically operates in direct current-constant height mode in which the tip, typically held at a potential to detect or electrolyze an analyte at a diffusion-limited rate, is scanned in a fixed (x-y) plane above the interface of interest. The tip response, recorded as a function of position, provides a current image which depends on both the sample topography (distance between the tip and the interface) and sample activity; and one cannot unambiguously determine these two parameters. Several methods have been proposed to address this general issue, including: (i) the use of two electroactive mediators in the solution, one which maps the topography alone and the other the activity;[7] (ii) the use of impedance based methods;[8–11] (iii) shear force methods;[12–15] and (iv) the integration of UMEs into atomic force microscopy (AFM) tips.[16–21] Methods (iii) and (iv) are attractive because they utilize a force based feedback signal to allow a close (and more or less constant) separation to be maintained between the tip and interface of interest during imaging, but they require additional specialist instrumentation and non-conventional tips.

Herein, we describe a simple new approach for controlling the distance be-

tween a conventional SECM tip (metal wire sealed in a glass capillary) and surface based on the application of a small AC positional perturbation to the piezoelectric positioner controlling the tip normal to the surface of interest (z-axis). This is attractive because it requires minimal additional hardware and is easily implemented. Under this AC positional perturbation, the amplitude of the oscillation becomes damped just as the tip encounters the surface (in some respects akin to Tapping Mode (TM) AFM,[22,23] but different in that the tip is oscillated at much lower frequencies). The damping is detected and provides information on the tip-surface separation (e.g. for approach curve measurements), and can also be used as a set point to maintain a fixed distance between the tip and surface during electrochemical imaging (mean current and AC current information). IC-SECM differs from early tip position modulation (TPM) studies of Wipf and Bard[24] in that a non-electrochemical signal is used to provide the feedback and positioning sensitivity. The approach herein is thus attractive because it would allow other types of tips, such as potentiometric electrodes, to be deployed in the future.

2.3 Experimental

2.3.1 Apparatus and Instrumentation

Coarse control of the SECM tip, mounted perpendicular to the substrate surface, utilized a manual x,y,z stage. Fine control was realized by three (x, y, z) piezoelectric positioners, with 100 μm total travel each, fitted with strain gauge sensors (Nanocube P-611.3S, Physik Instrumente), for closed loop operation with an amplifier/servo (E-664 LVPZT, Physik Instrumente). The piezoelectric positioner amplifier/servo was controlled through a field programmable gate array (FPGA) card (NI PCI-7830 R, National Instruments) from a PC running custom LabVIEW code (labVIEW 9.0, National Instruments). An AC signal (generated by a home-built AC signal generator) was added to the z piezoelectric positioner control signal

with a homebuilt signal adder. The AC signal created a sinusoidal oscillation of $\sin(2 \times f \times t)$ in the height of the SECM tip about the average tip height. All experiments were carried out in a two-electrode arrangement, with the tip as the working electrode and an Ag/AgCl (0.1 M KCl) quasi-reference electrode. The SECM tip current, measured by a homebuilt current to voltage converter, and the locations of the piezoelectric positioners were recorded through the FPGA card. The SECM was operated in a diffusion-limited feedback configuration, with the tip potential applied by the FPGA card. A schematic of this setup is shown in Figure 2.1.

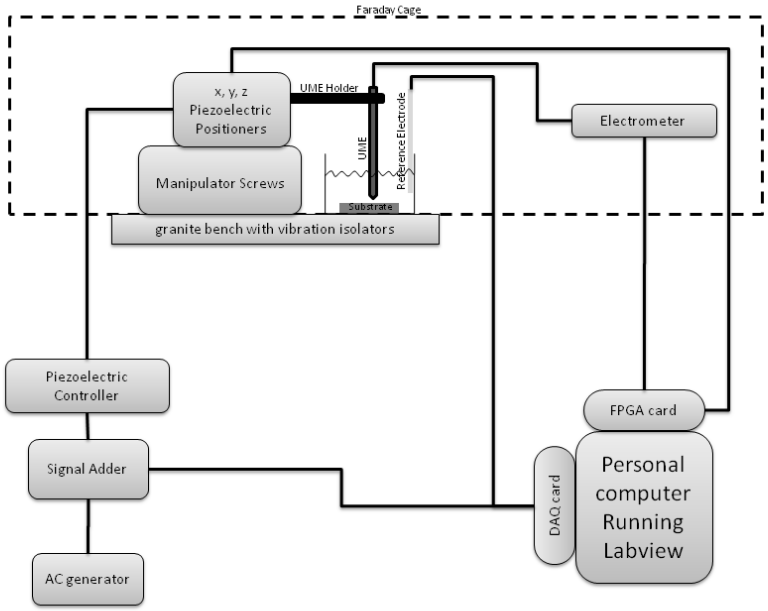

Figure 2.1: IC-SECM configuration. The signal adder and the AC generator are the only additional components that are needed for IC-SECM, as compared to SECM.

2.3.2 IC-SECM Approach Curves

Approach curve measurements were carried out by translating the SECM tip towards the substrate using the z piezoelectric positioner (at an average velocity of 0.066 μm s^{-1}). Simultaneously, the SECM tip was typically oscillated at 70 Hz with a

magnitude of 1 - 4 % of the active electrode radius. The IC-SECM approach curve was terminated when IC was detected. For the studies herein, this was defined as a greater than 15 % sustained decrease in the z piezoelectric positioner strain gauge sensor (z-SGS) oscillation amplitude as compared to that in the bulk solution.

2.3.3 IC-SECM Imaging

The SECM tip was engaged to the surface using an IC-SECM approach curve which halted when IC was detected. An image was constructed with a series of line scans. Each line scan consisted of a forward IC scan, where IC was maintained throughout, and a reverse constant distance scan, where the tip tracked the topography. The constant distance for the reverse scan was identified by the z-positions in the forward scan. This separation was typically 1.0 μm. During the IC scan, the SECM tip height was updated every 0.1 μm by a proportional controller, which took the form $z_{new} = z_{old} + P * (z^{SGSAmplitude} - (1 - 0.1) * z^{SGSBulkAmplitude})$, where z_{new} and z_{old} are the new and old SECM tip height respectively, $z^{SGSAmplitude}$ is the z-SGS oscillation amplitude and $z^{SGSBulkAmplitude}$ is the z-SGS oscillation amplitude in the bulk solution. P was set to 1. Thus, a decrease in the z-SGS oscillation amplitude was used as a set point for scanning. The SECM tip current was typically measured every 4 μm after a 20 ms pause in SECM tip movement.

2.3.4 Materials and chemicals

Solutions. These comprised 2 mM or 0.5 mM ferrocenylmethyltrimethylammonium ($FcTMA^+$) hexafluorophosphate (obtained from the metathesis of ferrocenylmethyltrimethylammonium iodide and silver hexafluorophosphate (Strem Chemicals)), with a supporting electrolyte of 0.1 M potassium chloride (Aldrich, AR grade), made up in Milli-Q reagent grade water (resistivity of ca. 18.2 MΩ cm at 25 °C). **Substrates.** The model surface for imaging comprised parallel gold bands (25 μm width, 20 μm pitch) on a glass microscope slide created by a lift off process. A

substrate with conducting (gold) and insulating (glass) regions was similarly created for approach curve measurements. **Probes.** Pt disk electrodes of 1 μm ($RG = 10$) and 12.5 μm ($RG = 10$) radius were used.[25]

2.4 Results and Discussion

2.4.1 IC-SECM Approach Curves

Typical IC-SECM approach curves of the 12.5 μm and 1 μm radius Pt disk electrodes to conducting (gold) and non-conducting (glass) substrates are shown in Figure 2.2. The tip was held at a potential of 0.44 V for the diffusion-limited one-electron oxidation of $FcTMA^+$ and the classical negative feedback response for the glass substrate and substantial positive feedback for the gold surface, as recorded by the average SECM tip current (i_{mean}), can be identified clearly.[26] The z-SGS oscillation amplitude stays constant for most of the approach curve duration, only showing a decrease when IC is made between the tip and the surface. This decrease can be detected reliably and in each case was used to automatically halt the progress of the SECM tip towards the substrate surface.

When IC is detected, the magnitude of i_{mean} for both substrates[26] indicates that the UME face and substrate surfaces are not parallel. As is well known, the glass surround of the UME comes into contact with the substrate surface and it is this that is detected in IC. Importantly, because the IC response informs as to when the probe makes physical contact, we can analyze the currents at the point unambiguously, to accurately estimate the distance between the active part of the electrode and substrate (2.0 μm for the 12.5 μm radius electrode and 0.13 μm for the 1 μm radius electrode), and hence the angle between the tip face and the substrate.[27] The 12.5 μm radius electrode tip face is at an angle to the substrate of 0.8 degrees, the 1 μm radius electrode tip face is at an angle to the substrate of 0.7 degrees. The similarity of these values for different sized electrodes, prepared similarly gives

further confidence in the IC-SECM method. The feedback curves for the unbiased gold bands can be seen to comprise some kinetic control of mediator turnover at the surface.[28] The apparent rate constant[29] is 0.09 ± 0.01 cm s^{-1} for the 12.5 μm electrode and is 0.11 ± 0.01 cm s^{-1} for the 1 μm electrode. The similarity in the rate constant with different sized electrodes gives confidence in the IC-SECM method for recording and analyzing approach curves. The turnover rates are a little lower than seen recently for other unbiased gold surfaces[28] but this can be accounted for by the fact that we made no attempt to clean the surface or pretreat the surface.

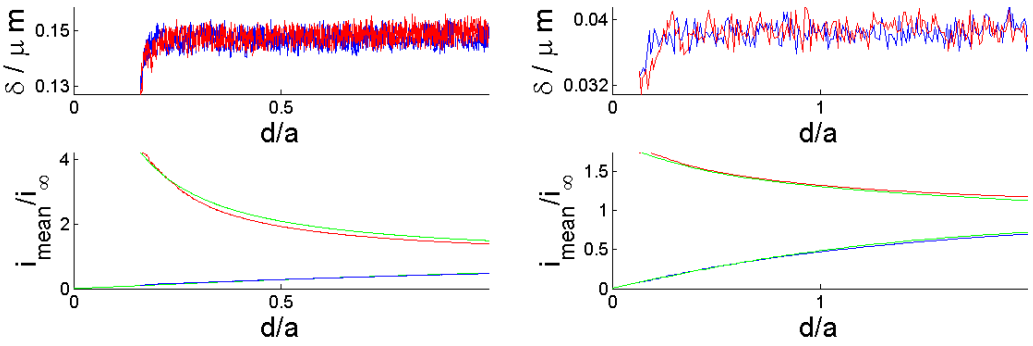

Figure 2.2: Typical feedback approach curves to conducting, gold (red), and non-conducting, glass (blue), substrates. Left: 12.5 μm radius Pt disk electrode oscillated at 70 Hz, δ = 145 nm in 0.5 mM $FcTMA^+$. Right: 1 μm radius Pt disk electrode oscillated at 70 Hz, δ = 39 nm in 2 mM $FcTMA^+$. Top: SECM tip oscillation amplitude as a function of the tip-substrate separation. Bottom: Mean SECM tip current, i_{mean}, as a function of the tip-substrate separation. The mean SECM current for the analytical approximation for the feedback response is shown in green.[27,29] i_{mean} was normalized by the bulk steady-state SECM tip current, i_∞. The distance from the substrate, d, was normalized by the SECM tip radius, a. IC-SECM approach curves were 100% reproducable.

2.4.2 IC-SECM Imaging

Figure 2.3 shows a typical set of images obtained in one scan by IC-SECM imaging of gold bands on glass using a 1 μm radius Pt disk electrode. Figure 2.3 (a) and (b) are average current images obtained in IC (forward scan, (a)) and constant separation mode (at 1.0 μm in the reverse scan, (b)). Both images clearly show the conducting

nature of the gold bands (high current) and insulating gaps (low current). Notably the IC i_{mean} image shows greater sensitivity to changes in conductivity than the constant distance image. This is because the tip is closer to the surface when in IC.

In addition to recording the mean current, one can record the amplitude of the current oscillations, i_{ac}. These data ((c) and (d)) were obtained simultaneously with the average current data ((a) and (b)) and show the same underlying features, but with a greater dynamic range, consistent with earlier TPM work.[24] The IC i_{ac} image (c) again shows more sensitivity than the constant distance i_{ac} image (d) because of the closer tip-substrate separation.

The topography images ((e) and (f)) obtained by recording the location of the z piezoelectric positioner reveal the orientation of the substrate. The substrate is clearly at a slope of approximately 1.5 degrees, as revealed in Figure 2.3 (e). Significant local changes in substrate height, due to the gold bands, are also visible in both images, especially in the plane fitted image (f). It can be seen that the gold bands are between 200 nm and 300 nm in height (consistent with the lithographic procedure used to make the substrate). The local height changes are offset as compared to the location of the gold bands in the current images because, as highlighted above, the glass sheath surrounding the electrode makes IC with the substrate. This effect could be exploited in the future by deliberately incorporating a "distance-sensing" element into the tip, e.g. by a focused ion beam or other method, or by preparing tapered glass pipettes with a very fine wall.[27]

2.5 Conclusions

IC-SECM constitutes a simple and robust new method of identifying the substrate surface. In particular, the use of IC-SECM means that the contact between the tip and the surface can be determined and, more importantly, this allows the substrate topography and activity to be identified unambiguously. IC-SECM requires a closed-

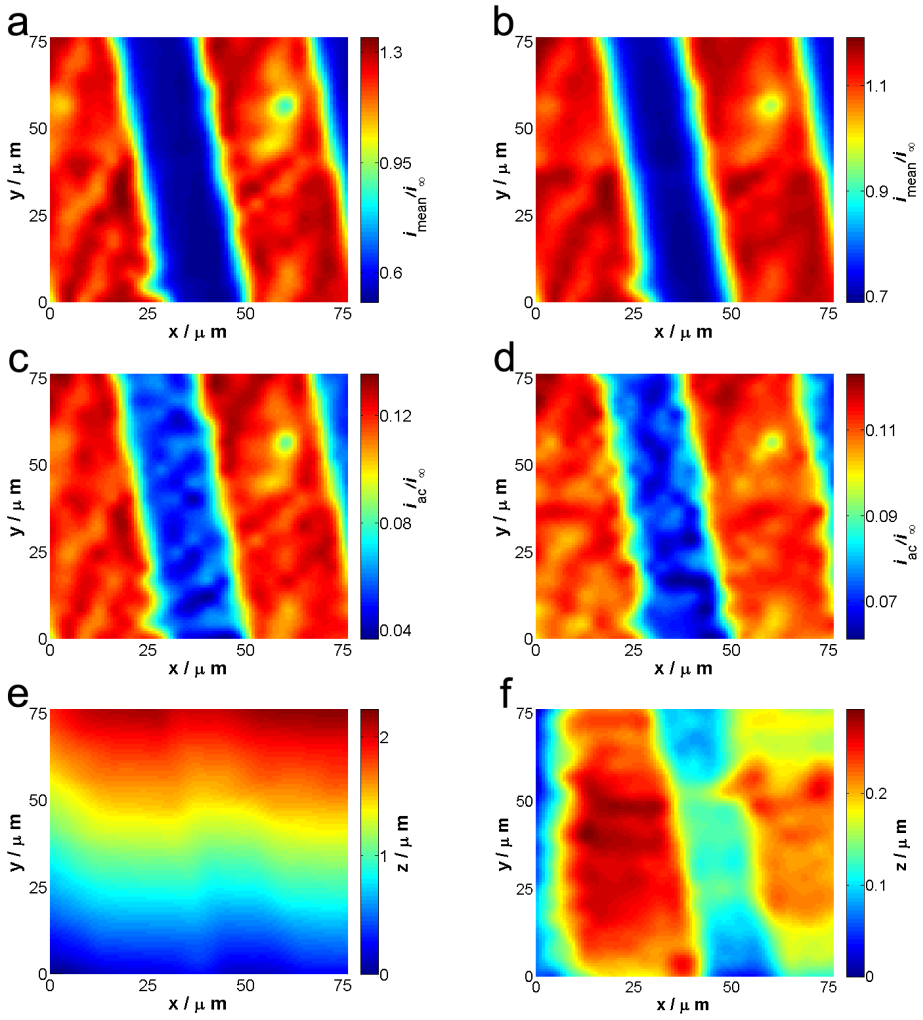

Figure 2.3: IC-SECM imaging of gold bands on glass obtained using a 1 μm radius Pt disk electrode (70 Hz, δ = 39 nm, 2 mM $FcTMA^+$). (a) Average tip current in IC forward scan. (b) Average tip current at a constant separation of 1 μm from the surface in the reverse scan. (c) i_{ac} in IC. (d) i_{ac} at a constant separation of 1 μm. (e) Surface topography from the z-piezoelectric positioner motion. (f) Plane fitted surface topography. The latter was constructed by taking the plane of best fit to the surface topography away from the surface topography. The tip currents have been normalized by the bulk SECM tip current, i_∞. IC-SECM imaging of gold band was highly (close to 100%) reproducable.

loop positioner for the z-axis or a positioner that gives a feedback signal for tip position control. As such, IC-SECM can be easily implemented on most existing SECM setups with existing SECM tips, only requiring an AC generator and a small

amount of additional control code. This distinguishes IC-SECM from the other tip positioning methods highlighted in the introduction. IC-SECM has the potential to be applied in many situations. The feedback control is based on the physical interaction of the SECM tip with the underlying substrate and thus allows for the application of this technique with many different types of tip. We expect it will be particularly useful for positioning and imaging with potentiometric probes which are otherwise difficult to utilize. Future work will explore such tips, nanoscale electrodes and softer interfaces, so as to elucidate the full range of situations which IC-SECM may be useful.

2.6 Acknowledgements

This work was supported by the EPSRC (MOAC/DTC studentship for K. M. and M. E.). We are grateful to Professor Julie Macpherson for helpful advice and supplying an electrode.

2.7 References

(1) Bard, A. J.; Fan, F. F.; Pierce, D. T.; Unwin, P. R.; Wipf, D. O.; Zhou, F. *Science* **1991**, 254, 68-74.

(2) Amemiya, S.; Bard, A. J.; Fan, F. F.; Mirkin, M. V.; Unwin, P. R. *Annu. Rev. Anal. Chem.* **2008**, 1, 95-131.

(3) Wittstock, G.; Burchardt, M.; Pust, S. E.; Shen, Y.; Zhao, C. *Angew. Chem. Int. Ed.* **2007**, 46, 1584-1617.

(4) Edwards, M. A.; Martin, S.; Whitworth, A. L.; Macpherson, J. V.; Unwin, P. R. *Physiol. Meas.* **2006**, 27, R63-108.

(5) Bard, A. J.; Mirkin, M. V. (eds) *Scanning Electrochemical Microscopy*; Marcel Dekker Inc: New York, 2001.

(6) Zigah, D.; Noel, J.; Lagrost, C.; Hapiot, P. *J. Phys. Chem. C* **2010**, 114,

3075-3081.

(7) Gonsalves, M.; Barker, A. L.; Macpherson, J. V.; Unwin, P. R.; O'Hare, D.; Winlove, C. P. *Biophys. J.* **2000**, 78, 1578-1588.

(8) Alpuche-Aviles, M. A.; Wipf, D. O. *Anal. Chem.* **2001**, 73, 4873-4881.

(9) Kurulugama, R. T.; Wipf, D. O.; Takacs, S. A.; Pongmayteegul, S.; Garris, P. A.; Baur, J. E. *Anal. Chem.* **2005**, 77, 1111-1117.

(10) Eckhard, K.; Schuhmann, W. *Analyst* **2008**, 133, 1486-1497.

(11) Gabrielli, C.; Huet, F.; Keddam, M.; Rousseau, P.; Vivier, V. *J. Phys. Chem. B* **2004**, 108, 11620-11626.

(12) Lee, Y.; Ding, Z.; Bard, A. J. *Anal. Chem.* **2002**, 74, 3634-3643.

(13) Takahashi, Y.; Shiku, H.; Murata, T.; Yasukawa, T.; Matsue, T. *Anal. Chem.* **2009**, 81, 9674-9681.

(14) Yamada, H.; Fukumoto, H.; Yokoyama, T.; Koike, T. *Anal. Chem.* **2005**, 77, 1785-1790.

(15) Ludwig, M.; Kranz, C.; Schuhmann, W.; Gaub, H. E. *Rev. Sci. Instrum.* **1995**, 66, 2857-2860.

(16) Macpherson, J. V.; Unwin, P. R. *Anal. Chem.* **2000**, 72, 276-285.

(17) Macpherson, J. V.; Unwin, P. R. *Anal. Chem.* **2001**, 73, 550-557.

(18) Kranz, C.; Friedbacher, G.; Mizaikoff, B.; Lugstein, A.; Smoliner, J.; Bertagnolli, E. *Anal. Chem.* **2001**, 73, 2491-2500.

(19) Kueng, A.; Kranz, C.; Lugstein, A.; Bertagnolli, E.; Mizaikoff, B. *Angew. Chem. Int. Ed.* **2003**, 42, 3238-3240.

(20) Macpherson, J. V.; Jones, C. E.; Barker, A. L.; Unwin, P. R. *Anal. Chem.* **2002**, 74, 1841-1848.

(21) Dobson, P. S.; Weaver, J. M.; Holder, M. N.; Unwin, P. R.; Macpherson, J. V. *Anal. Chem.* **2005**, 77, 424-434.

(22) Hansma, P.; Cleveland, J.; Radmacher, M.; Walters, D.; Hillner, P.; Bezanilla, M.; Fritz, M.; Vie, D.; Hansma, H.; Prater, C.; Massie J.; Fukunaga L.; Gurley J.;

Elings V. *Appl. Phys. Lett.* **1994**, 64, 1738-1740.

(23) Moller, C.; Allen, M.; Elings, V.; Engel, A.; Muller, D. J. *Biophys. J.* **1999**, 77, 1150-1158.

(24) Wipf, D. O.; Bard, A. J. *Anal. Chem.* **1992**, 64, 1362-1367.

(25) Wightmann, R. M.; Wipf, D. O. In *Electroanalytical Chemistry* Vol. 15; Bard, A. J.; Marcel Dekker: New York, 1989.

(26) Kwak, J.; Bard, A. J. *Anal. Chem.* **1989**, 61, 1221-1227.

(27) Amphlett, J. L.; Denuault, G. *J. Phys. Chem. B.* **1998**, 102, 9946-9951.

(28) Laforge, F. O.; Velmurugan, J.; Wang, Y.; Mirkin, M. V. *Anal. Chem.* **2009**, 81, 3143-3150.

(29) Wei, C.; Bard, A. J.; Mirkin, M. V. *J. Phys. Chem.* **1995**, 99, 16033-16042.

Chapter 3

Quantitative Visualization of Molecular Transport through Porous Membranes: Enhanced Resolution and Contrast using Intermittent Contact-Scanning Electrochemical Microscopy

The IC-SECM technique was used to quantify the molecular transport through the porous biological membrane, dentin (also known as dentine), which is located between the pulp and enamel in teeth. Tubules, typically 0.5 - 2.0 μm in diameter, run through the dentin and transport species from one side to the other. The tubules are an important target for treatments of dentinal hypersensitivity. The spatial resolution of IC-SECM allows a UME to be placed close to the sample, and the fluid flow rates through individual tubules quantified.

This chapter contains the published communication describing this work. I was responsible for the experimentation, data analysis, simulation and paper preparation. Michael E. Snowden and Massimo Peruffo contributed to sample preparation and simulation discussions.

Quantitative Visualization of Molecular Transport through Porous Membranes: Enhanced Resolution and Contrast using Intermittent Contact-Scanning Electrochemical Microscopy

Kim McKelvey, Michael E. Snowden, Massimo Peruffo, Patrick R. Unwin

Anal. Chem., 2011, 83(17), 6447 - 6454.

3.1 Abstract

The use of intermittent contact-scanning electrochemical microscopy (IC-SECM) in diffusion-limited amperometric mode to visualize and quantify mass transport through multiporous membranes, is described, using dentin as a model example. The IC mode of SECM employs the damping of a vertically modulated ultramicroelectrode (UME) to achieve positioning close to the receptor side of a membrane. In this way the UME can detect electroactive species close to the pore exit. A key aspect of IC-SECM is that in addition to the direct current (dc) from the diffusion-limited detection of the analyte, an alternating current (ac) also develops due to the motion of the probe. It is demonstrated that this ac signal enhances the spatial resolution of SECM detection and allows the hydrodynamic flow of species to be detected from individual closely spaced pores. The experimental deductions are

supported by three-dimensional finite element modeling which allows IC-SECM current maps to be analyzed to reveal transport rates through individual pores. The method described should be widely applicable to multi-porous membrane transport.

3.2 Introduction

Porous membranes are widely used for many applications in analytical science and other areas.[1–3] These membranes typically consist of closely spaced pores of variable size and mass transport rates, and membrane transport is typically evaluated by averaging across large areas of the membrane. However, this measurement approach obscures information about individual pores and thus the distribution of mass transport rates that operate.

Among many applications of scanning electrochemical microscopy (SECM)[4–6] its use for visualizing and quantifying transport through membranes[7–10] and porous materials[11–26] on a local scale has been among the most successful. Pioneering work in this area by White and co-workers[11,16,17] led to subsequent applications, notably the investigation of iontophoretic and electroosmotic transport through mouse skin,[15,16,18] local hydraulic permeability measurements of dentin[23,24,27] and diffusive transport across dentin.[22] In all of these cases heterogeneity in transport rates was demonstrated as an important consideration for understanding membrane function.

A recent theme in SECM measurements of membrane transport has been to improve the spatial resolution and contrast. In particular, for multi-porous membranes with discrete pores, a key goal has been to develop methods capable of resolving transport at the level of a single pore. Advances include the use of the reverse imaging mode, where the SECM tip is used to detect the accumulation of species from the donor side of the pore[14,28] and impedance imaging.[12,29] Related techniques such as combined SECM-atomic force microscopy (AFM)[19–21] and scanning ion conductance microscopy (SICM)[30,31] have also enhanced the spatial resolution of

electrochemical imaging of membrane transport.

An advantage of SECM is that a wide range of tips can be employed, and in amperometric mode the applied potential can be used as a method for detecting particular species selectively and quantitatively. On the other hand, conventional SECM lacks positional feedback, which means that samples have to be flat and aligned with great care to avoid convolution from topographical effects and also tip crash. This often restricts the tip size and tip-substrate separation that can be employed in SECM, which are critical limitations for membrane transport studies. Consequently, SECM has mainly been used to image single micropores in an otherwise inert membrane,[17] or materials such as skin[15,16,18,28] with a low density of (widely spaced) micropores. For materials such as dentin[23,24,32] where the naturally formed tubules (pores) running through the membrane are much more closely spaced, it has only been possible to make measurements of single pore transport under conditions where all other neighboring pores are inactive.[24]

The goal of this paper is to demonstrate how one can significantly improve the resolution and contrast of SECM measurements of membrane transport through the use of intermittent contact (IC)-SECM.[33] This primarily serves two purposes. First, IC-SECM allows the tip to be scanned with positional feedback just above a substrate. For porous materials this means the tip can access material just above the pore exit. Second, IC-SECM provides dc and ac amperometric maps and the phase of the ac current, akin to tip position modulation SECM.[34,35] We show herein that the ac map, in particular, greatly enhances the spatial resolution of the amperometric signal and, together with the phase map, allows unambiguous identification of membrane activity. Using dentin as a model sample, comprising a high density (typically of the order of 10^7 cm^{-2}) of micron-sized pores, we show that quantitative measurements of convective fluid flow through an array of active pores is achievable with individual pore resolution. The experimental observations are supported by numerical modeling of multipore transport to allow transport rates through individ-

ual pores to be elucidated. The results are valuable, not only for demonstrating clear advantages of IC-SECM for functional imaging, but also because knowledge of local convective-diffusion through dentin, an integral component of the tooth structure, is of vital importance for understanding and treating dentinal hypersensitivity.[27,36–39]

3.3 Experimental

3.3.1 Materials

Bovine dentin slices, ca. 1 cm by 1 cm square, with a typical thickness of 250 μm were used. These were prepared and treated using standard procedures outlined elsewhere.[32] Electron microscopy confirmed dentinal tubules with typical diameter of 1.5 μm and density ca. 10^7 cm^{-2} (*vide infra*). A 15 mM hexaammineruthenium (III) chloride $Ru(NH_3)_6Cl_3$ (Fisher Scientific) solution, with a supporting electrolyte of 0.1 M potassium chloride (Aldrich, AR grade), made up in Milli-Q reagent grade water (resistivity ca. 18.2 MΩ cm at 25 °C) was used as the solution on the donor side of the membrane. A supporting electrolyte solution containing 0.1 M potassium chloride, in Milli-Q reagent grade water served as the receptor solution.

3.3.2 Instrumentation

The instrumentation for IC-SECM and its implementation was described recently.[33] The SECM tip was a Pt disk electrode of 1 μm radius ($RG = 10$, where RG is the ratio of the overall probe radius to the electrode radius) constructed from Wollaston wire using standard procedures,[40] such that the electrodes was in the center of the tip. A two-electrode voltammetric set-up, with an Ag/AgCl (0.1 M KCl) quasi-reference electrode (QRE), was used.

Figure 3.1 shows a diagram of the experimental arrangement. To create a hydrostatic pressure across the dentin slice, the dentin slice was sealed, using O-rings, to the barrel end of a 5 ml syringe tube (radius 5 mm), with the plunger removed.

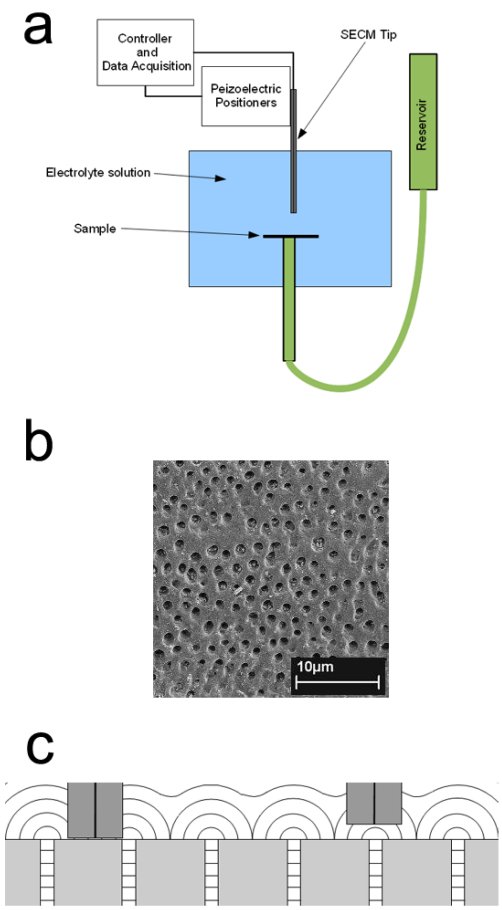

Figure 3.1: a) Experimental setup. The sample (dentin) is mounted over a reservoir containing the redox active, $Ru(NH_3)_6^{3+}$, species and electrolyte. The SECM tip, in an electrolyte solution, is moved with respect to the receptor surface of the membrane using piezoelectric positioners. b) SEM of a typical slice of dentin showing the openings of tubules of diameter ca. 1.5 μm which run across the sample. c) Mass transport through tubules in the dentin sample, with a tip close to the surface on the left (as in the IC scan) and the tip further away from the surface on the right (as in the reverse constant distance scan).

This was filled with the 15 mM $Ru(NH_3)_6^{3+}$ (0.1 M KCl) solution and connected, using flexible plastic tubing, to a donor reservoir containing the same solution. The syringe, with dentin sample fixed across the end, was mounted vertically below the SECM tip in a sample (receptor) chamber containing only 0.1 M potassium chloride solution.

The reservoir was positioned at a height of 20 cm with respect to the sur-

face in the receptor part of the cell providing a hydrostatic pressure of ca. 2 kPa across the dentin slice, which is typical of that used for dentin disk permeability measurements,[23] matching the pulpal pressure across dentin measured in vivo.[41,42] This pressure induced the flow of electrolyte/redox mediator solution from the donor side of the cell to the receptor side that contained only electrolyte solution.

3.3.3 Imaging Procedure

The SECM tip was held at a potential (-0.25 V) with respect to the QRE for the transport-limited one-electron reduction of $Ru(NH_3)_6^{3+}$ to $Ru(NH_3)_6^{2+}$ and various current signals (and ac phase) were recorded as a function of tip position. IC-SECM was used to position the tip close to the surface and maintain a constant distance from the surface during imaging, as described previously.[33] In brief, the tip was oscillated, using a piezoelectric positioner (Nanocube P-611.3S, Physik Instrumente), normal (vertical) to the surface (dentin) of interest. The vertical position of the tip was monitored by the integrated strain gauge sensor of the piezoelectric positioner (Nanocube P-611.3S, Physik Instrumente). When the tip came into intermittent contact with the sample, a damping in the oscillation amplitude of the strain gauge sensor signal was detected. This was used as a feedback signal to control the vertical position of the tip with respect to the sample and maintain an essentially constant (close) separation between the tip and the sample.

The tip was first engaged to the dentin surface using IC-SECM in approach mode, in which the SECM tip was translated towards the dentin surface while oscillating at a frequency of 70 Hz with an amplitude of 50 nm. The approach was halted when a damping of 15% in the oscillation amplitude was detected. IC-SECM imaging was then carried out by scanning the tip in a series of lines. Each line scan consisted of an IC forward scan and a constant distance reverse scan. During the IC forward scan the SECM tip was moved in close proximity to the surface while adjusting the height of the tip based on the oscillation amplitude signal from the

strain gauge sensor so as to maintain intermittent contact with the surface. The reverse scan was then carried out in which the tip followed the surface topography, detected in the IC forward scan, at a constant distance of 1 μm. A series of line scans was used to construct a two-dimensional image of the area of interest. A scan area of 19 μm by 19 μm, with a line scan every 1 μm, was typically used in this study, and the current was measured every 0.5 μm after a 20 ms pause. The current can be decomposed into two components: the average value (dc current) and the magnitude of the oscillating component (ac current). The ac current was calculated by taking the oscillating component of the current of the same frequency (70 Hz) as the piezo-positioner driving signal, using a software implemented lock-in amplifier. This frequency-locked detection method allows the ac signal to be readily detected with high sensitivity. The phase of the ac current with respect to the tip position was also recorded. Thus, we obtain four current images: ac and dc in both the IC and constant distance modes and two images of the ac phase. The IC-SECM scan also reveals the z-position of the tip needed to maintain intermittent contact with the surface and hence a quasi-topography map. For the present application, the tip size is of the same scale as the pore size and so these maps typically revealed only general information about the slope on the sample which is not of interest herein.

3.3.4 Simulations

To complement the experimental measurements, a steady-state 3 dimensional finite element method (FEM) simulation of the transport of $Ru(NH_3)_6^{3+}$ through a dentin sample and the detection at a static SECM tip was carried out. Simulations encompassed transport through a single pore, as well as through two neighboring pores.

Fluid flow was simulated by solving the Navier-Stokes equations for incompressible flow. The concentration of $Ru(NH_3)_6^{3+}$ was then calculated by solving the convection-diffusion equation subject to the fluid flow solution. The current at the

SECM tip was calculated based on the total normal flux arriving at the electrode surface. The steady-state Navier-Stokes equations are given by:

$$\rho(\mathbf{u}.\nabla)\mathbf{u} = -\nabla p + \mu\nabla^2\mathbf{u} \quad (3.1)$$

$$\nabla\mathbf{u} = 0 \quad (3.2)$$

and the steady-state convection-diffusion equation is

$$\nabla(-D\nabla c + \mathbf{u}c) = 0 \quad (3.3)$$

where ∇ is the Laplacian operator, c is the concentration of $Ru(NH_3)_6^{3+}$, $\mathbf{u}$ is the fluid velocity vector, p is the fluid pressure, ρ is the density of the fluid which is set to 1.00 $\times$ 10^3 kg m^{-3} in this case, μ is the dynamic viscosity and is set to 1.0 $\times$ 10^{-3} Pa s^{-1} and D is the diffusion coefficient of $Ru(NH_3)_6^{3+}$ which is 6.8 $\times$ 10^{-6} cm^2 s^{-1}.

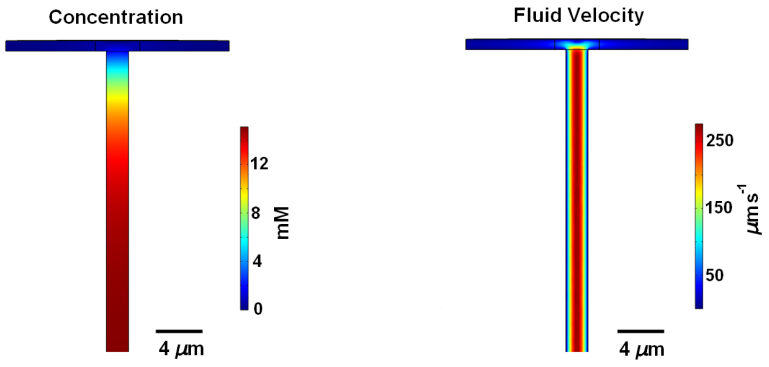

Figure 3.2: Concentration of $Ru(NH_3)_6^{3+}$ (a) and fluid velocity (b) for a typical simulation with the tip and pore coaxial. The inflow velocity was 150 μm s^{-1}.

The domain of interest was the dentin pore and the region between the UME and the substrate surface. The pore was modeled as a 250 μm long cylinder with a diameter of 1.5 μm, approximately the mean dentin pore size. The boundary conditions at the source (donor end) of the pore was a uniform normal fluid velocity

(plug flow), with the concentration of $Ru(NH_3)_6^{3+}$ fixed at 15 mM. The walls of the pore, electrode, surrounding glass and surface of the dentin were modeled as non-slip walls. Non-slip walls within the pore confine the fluid flow to a parabolic flow profile (see Figure 3.2), which has been reported for the pressure driven flow of fluid through nanoscale pores.[43,44] The geometry is also similar to that for free and confined impinging jet ultramicroelectrodes, for which non-slip boundary conditions have been shown to be appropriate at the electrode surface, even at much higher Reynolds numbers.[45,46] Fluid exits the model through the outlet between the UME and the substrate surface, defined by a zero pressure boundary condition. The concentration of $Ru(NH_3)_6^{3+}$ was set to zero at the electrode and at the outlet boundary. The geometries of the 2 models of the single and double pore are shown later where the simulation results are discussed (see Figure 3.4 and Figure 3.5). The boundary conditions and dimensions of the model are given in Table 3.1 and 3.2, respectively. A typical profile of the $Ru(NH_3)_6^{3+}$ concentration and fluid velocity at the exit of the pore is given in the Figure 3.2, from which it is evident that the SECM tip detects essentially all material emerging from a pore. It was assumed that the tip was parallel to the substrate.

Table 3.1: Model Boundary Conditions

Boundary	Description	Navier-Stokes Boundary Condition	Diffusion Boundary Condition
α	symmetry	$\mathbf{u}.\mathbf{n} = 0$	$-\mathbf{n}.(-D\nabla c + \mathbf{u}c) = 0$
β	wall	$\mathbf{u} = 0$	$-\mathbf{n}.(-D\nabla c + \mathbf{u}c) = 0$
γ	electrode	$\mathbf{u} = 0$	$c = 0$
ϵ	outlet	$p = 0,[\eta(\nabla\mathbf{u} + (\nabla\mathbf{u})^T)]\mathbf{n} = 0$	$c = 0$
ζ	inlet	$\mathbf{u} = -\text{inflowvelocity} \times \mathbf{n}$	$c = 15\text{mM}$

The dc current at the electrode was calculated as $2 * F * E_{TNF}$, where F is the Faraday constant and E_{TNF} is the total normal flux at the electrode surface. The ac current was approximated by calculating the difference in the dc current at three vertical displacements (the minimum, maximum and mean vertical displacements of the vertical oscillation of the tip; see Table 3.2). As each tip height and lateral displacement has its own distinct 3-D simulation grid, and small current differences

Table 3.2: Model Dimensions

Variable	Description	Value (μm)
e_h	Electrode Height	0.95 - 1.05
r_e	Electrode Radius	1
r_d	Sheath Radius	10
p_o	Pore Offset	0 - 9
p_d	Pore Depth	250
r_p	Pore Radius	0.75
p_{dist}	Double Pore Distance	5

are measured, there is naturally some variability in the calculated results which appears as "noise" in the raw ac current profiles (see Figure 3.4 and Figure 3.5). Note that this approach does not take into account fluid flow induced by the movement of the tip. A model for this scenario was presented recently,[34] and showed that when the tip modulation is small compared to the overall tip size, as it is in this case, tip convective effects are expected to be negligible.[34,35] The veracity of this approach for the conditions used herein is further confirmed by a simple back of the envelope calculation: the tip motion pumps fluid out of (and into) the active area of the tip electrode at ca. 11 μm^3 s^{-1}, whereas for the characteristic mean pore fluid velocity of 250 μm s^{-1} (*vide infra*), fluid exits the pore at more than 20 times this rate. Thus, the effect of any fluid flow induced by the tip motion is negligible when compared to fluid flow rate from a pore.

The simulations were run on a personal computer (Windows XP Pro 64 bit) using Matlab R2010b (The MathWorks, Cambridge, U.K.) and COMSOL Multiphysics 4.1 (Comsol AB, Sweden).

3.4 Results and Discussion

Typical current images, taken with a 1 μm radius Pt disk electrode operated in IC-SECM mode, of pressure-induced $Ru(NH_3)_6^{3+}$ transport through dentin are shown in Figure 3.3. The dc current (i_{mean}; Figure 3.3(a) and Figure 3.3(b)) and the ac current (i_{ac}; Figure 3.3(c) and Figure 3.3(d)) are shown for both the forward (IC)

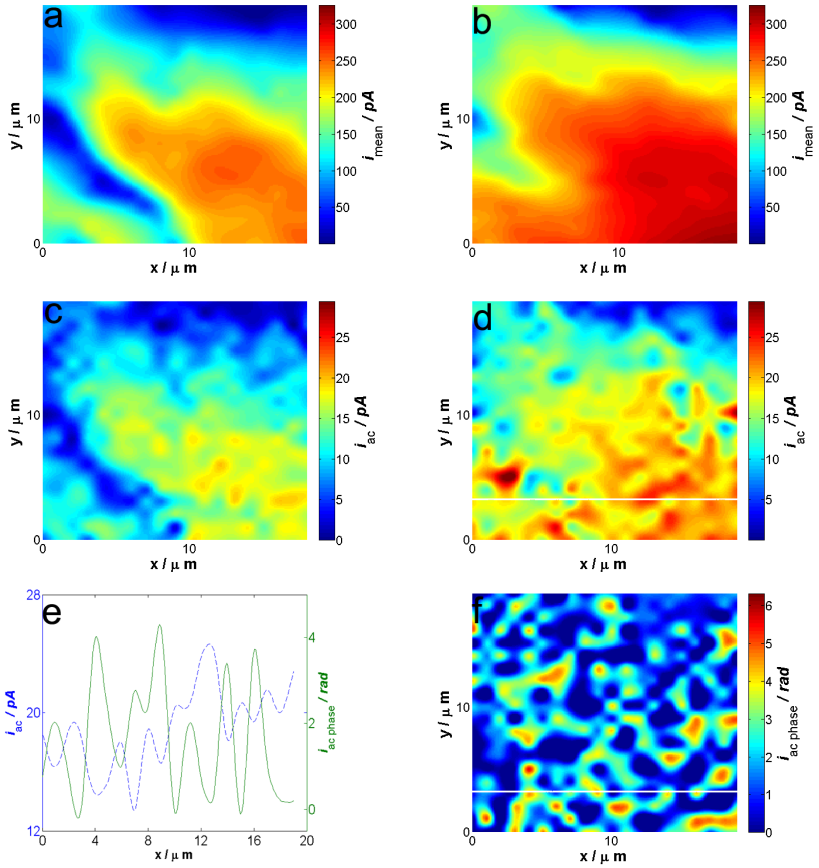

Figure 3.3: Current images of $Ru(NH_3)_6^{3+}$ transport across dentin obtained with IC-SECM, using a 1 μm radius Pt disk electrode, operated at 70 Hz with an amplitude of 50 nm. The current images obtained in IC mode are shown on the left hand side, as the dc current (a) and ac current (c) respectively. The current images obtained while at a constant distance, 1 μm from the surface, are shown on the right hand side, as dc current (b), ac current (d) and the ac current phase (f). A profile through one line of the ac current and ac current phase images is shown in (e) and its location is indicated by the white horizontal line on (d) and (f). IC-SECM imaging of dentin was reproducible, based on 6 samples.

scan and the reverse (constant distance) scan. The ac current phase is also shown for the reverse (constant distance) scan. Taken together, the current (flux) images highlight considerable heterogeneity of mass transport across the dentin sample. Regions of high and low flux (as evident in the i_{mean} and i_{ac} values) are observed within the 19 μm by 19 μm scan. This type of behavior is typical of all dentin

samples that have been imaged previously by SECM,[22,24,27] but there have been no reports of heterogeneity at this small length scale. The resolution of the mean (dc) current, in particular, compares most favorably with previous images obtained with a conventional constant height configuration[22] precisely because IC-SECM allows the deployment of a small tip, very close to the dentin surface, and topographical influences are largely eliminated in the current map recorded.

Figure 3.3(a) and 3.3(b) (mean (dc) current images in IC and constant distance mode) show similar features, but the active area of the sample (where i_{mean} is high) is more extensive in the reverse (constant distance) scan in Figure 3.3(b). This is expected because diffusion spreads material further from the source in a heterogeneously active sample. On the other hand, the local concentration of analyte should be lower when the tip is further from the source, but the tip current is actually higher in Figure 3.3(b) than in Figure 3.3(a). This apparent paradox can be rationalized because even this small tip cannot be considered simply as a passive (non-invasive) sensor of concentration due to the close tip-substrate separations employed to record these images. In particular, in the IC scan the tip will potentially inhibit transport across the membrane and the tip response will also be subject to very strong hindered diffusion of mediator from neighboring pores, which will diminish the current response, see Figure 3.1(c). Consequently, we concentrate on the back (constant distance mode) scan to evaluate membrane transport. Although some spatial resolution is lost by operating further from the surface, this distance is still only ca. 1 μm, which is sufficient to achieve high spatial resolution information.

The ac current in both the forward (IC) scan and the reverse (constant distance) scan correlate well with to the average tip current measurements. Generally, areas of the highest or lowest ac currents correspond to areas of high and low dc current, respectively. However, comparison of Figure 3.3(a) with 3.3(c); and Figure 3.3(b) with 3.3(d) shows clearly that the ac current varies spatially within the regions of the sample where high and low dc currents are detected. Moreover, the

variation of the ac current occurs on a similar length scale as the size and spacing of the dentinal pores, as shown in the SEM of dentin in Figure 3.1(b). It is evident from Figure 3.3(f) that the ac phase also varies significantly, with the variation occurring on a similar length scale to that seen in the ac current images. For the purpose of Figure 3.3(f) the ac phase is defined with respect to the z-piezo extension (which is a maximum during the periodic oscillation when the tip is closest to the surface): thus a phase of 0 rad corresponds to the current maximum occurring at the maximum piezo extension (tip closest to the surface) during the oscillation. It can be seen that the peaks in the ac current map in Figure 3.3(d) coincide well with ac minima, i.e. where the current tends to be in-phase (Figure 3.3(f)), highlighting clearly that local current maxima are due to the detection of flux from individual pores (to which the tip becomes more sensitive as it moves closer in the z-direction). In contrast, when the tip is laterally away from the mouth of the pore, it will tend to measure a lower current during maximum extension (closest to the surface) - as it will now experience restricted diffusion from the source, and a higher current will be seen further away (less restricted diffusion), resulting in an out-of-phase ac signal. This characteristic is seen most clearly in the line scan in Figure 3.3(e), where ac current maxima (corresponding to pores) coincide with ac phase minima (current signal in-phase with tip extension).

To confirm that IC-SECM was capable of detecting flow from single pores, the 3-dimensional FEM model was used to elucidate how the dc and ac components of the current related to the flow of $Ru(NH_3)_6^{3+}$ through individual pores. We first consider the dc current and ac current calculated for a 1 μm radius disk electrode, held 1 μm above the dentin surface with a characteristic fluid velocity of 75 μm s^{-1} (at the lower end of that detected and so the most challenging case; *vide infra*) at a range of horizontal offsets of the SECM tip from a single active pore source. The profiles of the dc and ac currents, with respect to the horizontal offset of the tip from the pore, are shown in Figure 3.4. As the offset increases, the magnitude

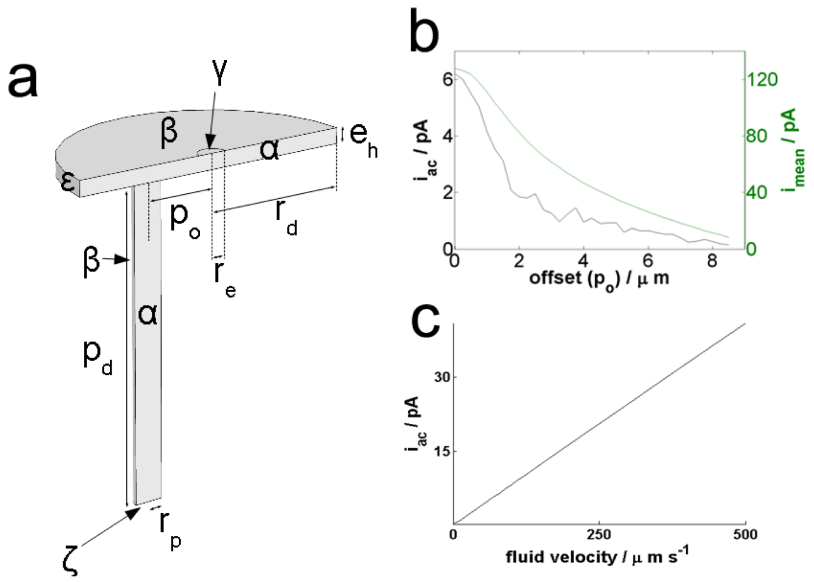

Figure 3.4: a) Geometry of the FEM model of mass transport through a single dentin pore and collection at the tip (see Table 3.2 for model description and dimensions). The pore source is located at the bottom of the schematic (pore inlet boundary, ζ) with the electrode in the top center (electrode surface boundary, γ). b) Raw current profiles (ac and dc) from FEM simulations of the mass transport of $Ru(NH_3)_6^{3+}$ through a single dentin pore and its collection at the electrode at a range of tip-pore offsets (p_o). c) The relation between the fluid flow rate and the ac current detected at the tip, when the tip is directly above the pore (no lateral offset, $p_o = 0$).

of the dc and ac currents diminishes. However, the dc profile extends over many multiples of the pore dimensions, such that the width of the dc profile is large compared to the inter-pore spacing that is found in dentin (typically 5 μm pore center to center). We thus deduce that the dc current response will sense material from multiple overlapping pores, so that fluxes from individual pores cannot be seen. This is evident in the dc current data (Figure 3.3(a) and 3.3(b)), and has been reported previously.[11,16,23,24]

Significantly, the profile of ac current, shown in Figure 3.4(b), with respect to the horizontal offset between the tip and the pore is considerably narrower than the dc current profile. Consequently, the overlap of the ac current signal due to adjacent pores will be limited. Clearly the narrowing of the ac current profile, as

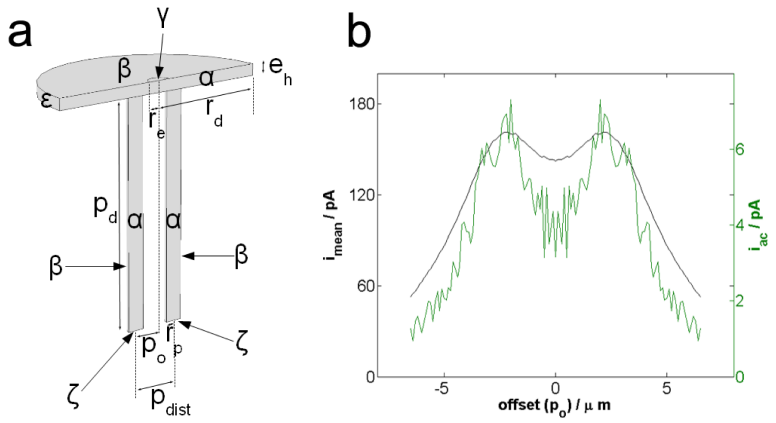

Figure 3.5: Current profiles from FEM simulations for the detection of $Ru(NH_3)_6^{3+}$ transport through two dentin pores, spaced 5 μm apart (center to center), and its collection at the electrode. The boundary conditions and model dimensions are defined in Table 3.1 and 3.2. a) Schematic of the simulation geometry. b) Comparison of the raw dc and ac current profiles.

compared to the dc current profile, means that for mass transport imaging the ac current image yields enhanced spatial resolution and contrast.

To confirm the deductions from the single pore simulations, a model of the dc and ac current profiles from two pores, at the typical inter-pore spacing for dentin (5 μm), was constructed. The results of this model, in Figure 3.5(b), again for a tip-substrate separation of 1 μm and a convective flow of 75 μm s^{-1} through each pore show that the dc current response is incapable of resolving the flux from two pores, but the ac current response is sufficient to obtain single pore resolution.

Since the overlap of the magnitude of the ac tip current from different pores is minimal, the local peak magnitude of the ac current provides an upper bound on the individual pore fluid flow velocity (transport rate). Individual pores can be identified from local peaks in the ac current. The relation between the peak ac current and fluid flow rate for a single pore is shown in Figure 3.4(c) and was calculated from the FEM model. Pores and pore velocities identified from the ac current image are shown in Figure 3.6, which also describes the procedure for identifying active pores. Figure 3.6(a) highlights 30 pores that are identified in the 19 μm by 19 μm scan area,

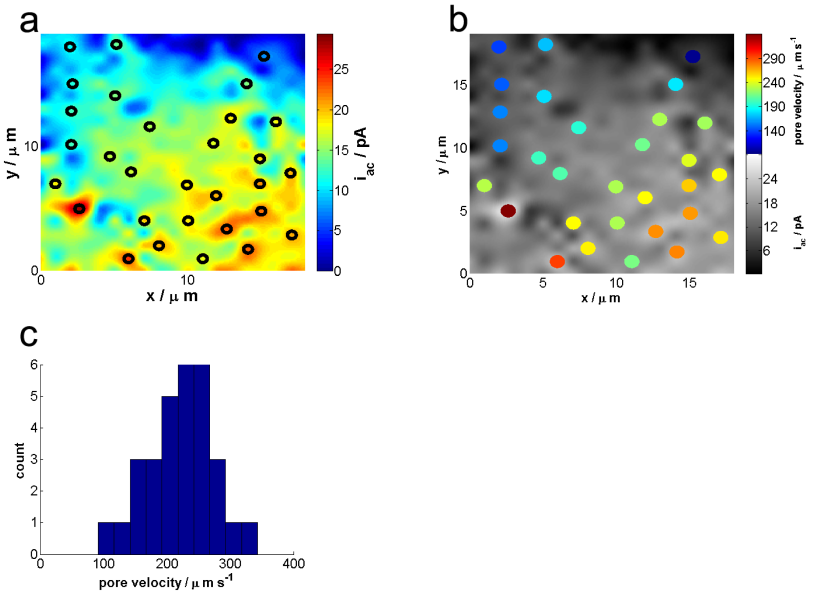

Figure 3.6: Analysis of the ac current map to obtain local pore velocity. a) Identification of individual pores as local peaks in the ac current, that are greater than the average ac current in the surrounding 3 μm and that are more than 2 μm from a neighboring pore. b) Mapping the pore velocity (deduced using Figure 3(c)) to the ac current map. The distribution of pore velocities in this area of the sample is shown in c).

corresponding to an active pore density of 8.3×10^6 cm^{-2}. This value is lower than, but of the same order as, the density of pore openings seen in Figure 3.1(b). The lower value for the active pore density is expected because some pores will be inactive to transport (blocked sub-surface).[23,24,32] The range of velocity values - highlighted in Figure 3.6(b) and (c) - is consistent with mean transport rates under similar conditions,[24] confirming the veracity of the IC-SECM approach. Significantly, the pore velocities show a normal distribution between ca. 100 μm s^{-1} and 340 μm s^{-1}, with a mode value of 230 μm s^{-1}. It is important to point out that the local velocity will be critically dependent on pore geometry and structure, and small variations from the idealized model will impact the mass transport rates, which explains the broad range seen. Generally, the distribution of pore velocities reveals a significant variation in individual pore transport rates.

3.5 Conclusions

IC-SECM provides a method to image regions of multiporous membranes and detect and analyze molecular transport at the level of individual pores. Through exemplar studies of dentin, we have shown that quantitative imaging is possible, with a small tip, yielding current maps that are essentially free from topographical effects, while avoiding tip crash due to the use of intermittent contact for distance control. Two components of the current, dc and ac, are measured during IC-SECM: the dc current is shown, through experiment and simulation, to generally be the result of transport from several neighboring pores to the electrode surface. However, the ac current is influenced, predominately, only by the transport from the nearest single pore and so provides superior resolution. This deduction was confirmed by measuring the ac phase, which is very sensitive to whether the tip is over, or away from, a pore. The ac current can be treated quantitatively, so providing a means of measuring fluid flow rates through individual pores.

The studies herein provide a foundation for the use of IC-SECM as a new probe of local membrane transport which is of widespread importance, as highlighted in the introduction. An important outcome of the studies described is that the scale of heterogeneities in transport rates from active pores in dentin has been observed and quantified via the ac current signal produced by IC-SECM. The inherent heterogeneity in individual pore transport rates is an important factor to be taken into account when developing treatments for dentinal hypersensitivity which typically acts to occlude tubules against fluid flow or uses active ingredients to desensitize nerve cells, which respond to fluid flow through tubules in vivo.

Although we have focused on multiporous membrane transport for the studies herein, the results are expected to be general, i.e. the ac signal of IC-SECM provides improved spatial resolution (and improved information content when coupled with the ac phase data) for SECM activity mapping. This advantage of ac imaging,

compared to conventional dc SECM, was evident in earlier TPM studies,[35] but IC-SECM has the considerable advantage that the current signals measured are free from topographical effects due to independent tip distance control.

3.6 Acknowledgements

This work was supported by EPSRC (MOAC/DTC studentship for K.M.). We are grateful to Professor Julie Macpherson for helpful advice and for supplying an electrode. We thank Unilever Research for supplying the dentin samples. Some of the equipment used in this research was obtained through Birmingham Science City with support from Advantage West Midlands and the European Regional Development Fund.

3.7 References

(1) Lawson, K. W.; Lloyd, D. R. *J. Mem. Sci.* **1997**, 124, 1-25.

(2) Coronas, J.; Santamaria, J. *Catal. Today* **1999**, 51, 377-389.

(3) Martin, C. R.; Nishizawa, M.; Jirage, K.; Kang, M. *J. Phys. Chem. B* **2001**, 105, 1925-1934.

(4) Amemiya, S.; Bard, A. J.; Fan, F.-R. F.; Mirkin, M. V.; Unwin, P. R. *Anal. Chem.* **2008**, 1, 95-131.

(5) Wittstock, G.; Burchardt, M.; Pust, S. E.; Shen, Y.; Zhao, C. *Angew. Chem. Int. Ed.* **2007**, 46, 1584-1617.

(6) Edwards, M. A.; Martin, S.; Whitworth, A. L.; Macpherson, J. V.; Unwin, P. R. *Physiolo. Meas.* **2006**, 27, R63-108.

(7) Grime, J. M. A.; Edwards, M. A.; Rudd, N. C.; Unwin, P. R. *Proc. Natl. Acad. Sci. U. S. A.* **2008**, 105, 14277-14282.

(8) Tsionsky, M.; Zhou, J.; Amemiya, S.; Fan, F.-R. F.; Bard, A. J.; Dryfe, R. A. W. *Anal. Chem.* **1999**, 71, 4300-4305.

(9) Yamada, H.; Matsue, T.; Uchida, I. Biochem. Bioph. *Res. Comm.* **1991**, 180, 1330-1334.

(10) Macpherson, J. V.; O'Hare, D.; Unwin, P. R.; Winlove, C. P. *Biophys. J.* **1997**, 73, 2771-2781.

(11) Scott, E. R.; White, H. S.; Phipps, J. B. *J. Mem. Sci.* **1991**, 58, 71-87.

(12) Ervin, E. N.; White, H. S.; Baker, L. A. *Anal. Chem.* **2005**, 77, 5564-5569.

(13) Lee, S.; Zhang, Y.; White, H. S.; Harrell, C. C.; Martin, C. R. *Anal. Chem.* **2004**, 76, 6108-6115.

(14) Uitto, O. D.; White, H. S.; Aoki, K. *Anal. Chem.* **2002**, 74, 4577-4582.

(15) Bath, B. D.; White, H. S.; Scott, E. R. *Pharm. Res.* **2000**, 17, 471-475.

(16) Scott, E. R.; White, H. S.; Phipps, J. B. *Anal. Chem.* **1993**, 65, 1537-1545.

(17) Bath, B. D.; Lee, R. D.; White, H. S.; Scott, E. R. *Anal. Chem.* **1998**, 70, 1047-1058.

(18) Scott, E. R.; Phipps, J. B.; White, H. S. *J. Invest. Dermatol.* **1995**, 104, 142-145.

(19) Macpherson, J. V.; Unwin, P. R. *Anal. Chem.* **2000**, 72, 276-285.

(20) Macpherson, J. V.; Jones, C. E.; Barker, A. L.; Unwin, P. R. *Anal. Chem.* **2002**, 74, 1841-1848.

(21) Gardner, C. E.; Unwin, P. R.; Macpherson, J. V. *Electrochem. Commun.* **2005**, 7, 612-618.

(22) Nugues, S.; Denuault, G. *J. Electroanal. Chem.* **1996**, 408, 125-140.

(23) Macpherson, J. V.; Beeston, M. A.; Unwin, P. R.; Hughes, N. P.; Littlewood, D. *Langmuir* **1995**, 11, 3959-3963.

(24) Macpherson, J. V.; Beeston, M. A.; Unwin, P. R.; Hughes, N. P.; Littlewood, D. *J. Chem. Soc. Faraday Trans.* **1995**, 91, 1407-1410.

(25) Ishimatsu, R.; Kim, J.; Jing, P.; Striemer, C. C.; Fang, D. Z.; Fauchet, P. M.; McGrath, J. L.; Amemiya, S. *Anal. Chem.* **2010**, 82, 7127-7134.

(26) Kim, E.; Xiong, H.; Striemer, C. C.; Fang, D. Z.; Fauchet, P. M.; McGrath, J.

L.; Amemiya, S. *J. Am. Chem. Soc.* **2008**, 130, 4230-4231.

(27) Williams, C. G.; Macpherson, J. V.; Unwin, P. R.; Parkinson, C. *Anal. Sci.* **2008**, 24, 437-442.

(28) Uitto, O. D.; White, H. S. *Anal. Chem.* **2001**, 73, 533-539.

(29) Ervin, E. N.; White, H. S.; Baker, L. A.; Martin, C. R. *Anal. Chem.* **2006**, 78, 6535-6541.

(30) Chen, C.-C.; Baker, L. A. *Analyst* **2011**, 136, 90-97.

(31) Chen, C.-C.; Derylo, M. A.; Baker, L. A. *Anal. Chem.* **2009**, 81, 4742-4751.

(32) Macpherson, J. V.; Unwin, P. R. *Electroanal.* **2005**, 17, 197-204.

(33) McKelvey, K.; Edwards, M. A.; Unwin, P. R. *Anal. Chem.* **2010**, 82, 6334-6337.

(34) Edwards, M. A.; Whitworth, A. L.; Unwin, P. R. *Anal. Chem.* **2011**, 83, 1977-1984.

(35) Wipf, D. O.; Bard, A. J. *Anal. Chem.* **1992**, 64, 1362-1367.

(36) Pashley, D. H. *J. Endodontics* **1986**, 12, 465-474.

(37) Andrade e Silva, S. M. de; Marquezini, L. J.; Manso, A. P.; Garcia, F. P.; Carrilho, M. R.; Pashley, D. H.; Tay, F. R.; Carvalho, R. M. *J. Adhes. Dent.* **2007**, 9, 505-512.

(38) Lavender, S. A.; Petrou, I.; Heu, R.; Stranick, M. A.; Cummins, D.; Kilpatrick-Liverman, L.; Sullivan, R. J.; Santarpia III, R. P. *Am. J. Dent.* **2010**, 23, 14A-19A.

(39) Wang, Z.; Sa, Y.; Sauro, S.; Chen, H.; Xing, W.; Ma, X.; Jiang, T.; Wang, Y. *J. Dent.* **2010**, 38, 400-410.

(40) Wightman, R. M.; Wipf, D. O. In *Electroanalytical Chemistry* Vol. 15; Bard, A. J., Ed.; 1988; pp. 268-353.

(41) Lin, M.; Lou, Z. Y.; Bai, B. F.; Xu, F.; Lu, T. J. *JMMB* **2011**, 11, 205-219.

(42) Pashley, D. H.; Matthews, W. G. *Archs Oral Biol.* **1993**, 38, 577-582.

(43) Ulrich, E. S.; Limbach, C. M.; Manne, S. *Appl. Phys. Lett.* **2008**, 93, 243103-243103-3.

(44) Thompson, A. P. *J. Chem. Phys.* **2003**, 119, 7503-7511.

(45) Bitziou, E.; Rudd, N. C.; Edwards, M. A.; Unwin, P. R. *Anal. Chem.* **2006**, 78, 1435-1443.

(46) Macpherson J. V.; Unwin, P. R. *Anal. Chem.* **1998**, 70, 2914-2921.

Chapter 4

Quantitative local photosynthetic flux measurements at intact chloroplasts and thylakoid membranes using scanning electrochemical microscopy (SECM)

Here we show how a conventional disk shaped UME can be used to quantify the production and consumption of oxygen during photosynthesis at isolated chloroplasts and thylakoid membranes. We also show how the generation of a redox active species from a single isolated thylakoid membrane can be measured.

This chapter consists of a communication currently in preparation. The

data for the oxygen generation and consumption experiments, Section 4.5.2 and 4.5.3, as well as the chloroplast intactness experiments, Section 4.5.1, was collected by Dr. Sophie Martin and appeared in her thesis, although it is reanalysed here. I was responsible for the FEM simulations, data fitting, single thylakoid membrane measurements and the paper preparation.

Quantitative local photosynthetic flux measurements at intact chloroplasts and thylakoid membranes using scanning electrochemical microscopy (SECM)

Kim McKelvey, Sophie Martin, Colin Robinson and Patrick R. Unwin

In preparation

4.1 Abstract

Scanning electrochemical microscopy (SECM) is shown to provide a fast and quantitative method to measure the local flux of oxygen and ferrocyanide ($Fe(CN)_6^{4-}$) at the source of photosynthesis in higher plants, namely chloroplasts and thylakoid membranes sourced from chloroplasts. SECM investigations require the immobilization of chloroplasts or thylakoid membranes onto a suitable substrate and we show that the detection of $Fe(CN)_6^{4-}$, produced from the photo-reduction of ferricyanide ($Fe(CN)_6^{3-}$), can be used to assay the intactness of chloroplasts. 75% of chloroplasts within a chloroplast film on a poly-L-lysine (PLL) covered substrate remain intact (similar to bulk levels of intactness). This demonstrates that this surface configuration is adequate for studying photosynthetic processes, and for studies of immobilization chloroplasts, in general. Oxygen generation at films of chloroplasts and thylakoid membranes was detected directly during photosynthesis, but in the thylakoid membrane case this reduced to sustained oxygen consumption. An initial oxygen concentration spike was detected at the electrode over both chloroplast

and thylakoid membrane films, and the kinetics of the oxygen generation rates were extracted by fitting the experimental data to a finite element model (FEM) representative of the SECM configuration. The oxygen generation profile was attributed to the oxidation state of the plastoquinone pool, which is known to be of a limited size, and a contributing factor within photoinhibition. Finally, the mobile nature of the SECM probe also allowed us to detect ferrocyanide from a single thylakoid membrane. These results confirm that SECM is a practical platform with which to investigate biological systems, in this case photosynthesis, and in particular that the time resolution allows quantitative kinetic information to be elucidated.

Keywords : Oxygen, Kinetics, Local Flux, Photosynthesis, Single cell.

4.2 Introduction

Photosynthesis is the ultimate source of virtually all metabolic energy, converting sunlight to a usable form of chemical energy to drive otherwise endogenic reactions needed for the growth and maintenance of organisms.[1,2] Within higher plants, all the primary processes of photosynthesis, e.g. light capture and electron transport, leading to NADPH and ATP synthesis, and many secondary processes,[1,2] are located in the chloroplast. The light-dependent components of the photosynthetic pathway are embedded in the thylakoid membrane which is contained within the chloroplast, as illustrated schematically in Figure 4.1 A. Isolated chloroplasts and thylakoid membranes have consequently been used extensively to investigate aspects of photosynthesis,[2] but the majority of investigations have been performed on large populations, with data averaged over many individual chloroplasts or membranes. This averaging reduces the temporal resolution of any measurement and, as such, obscures potentially interesting kinetic aspects of photosynthesis.

Microscopy investigations of individual chloroplasts and thylakoid membranes have tended to focus on structure, rather than the flux of chemical species, us-

ing techniques such as optical microscopy,[3–5] electron microscopy,[6–8] atomic force microscopy,[9,10] or scanning tunneling microscopy.[11] Optical microscopy techniques, such as fluorescence microscopy, do provide some opportunities to access chemical flux measurements from individual cells (or components) but this is indirect, requiring the use of appropriate indicators.[12,13]

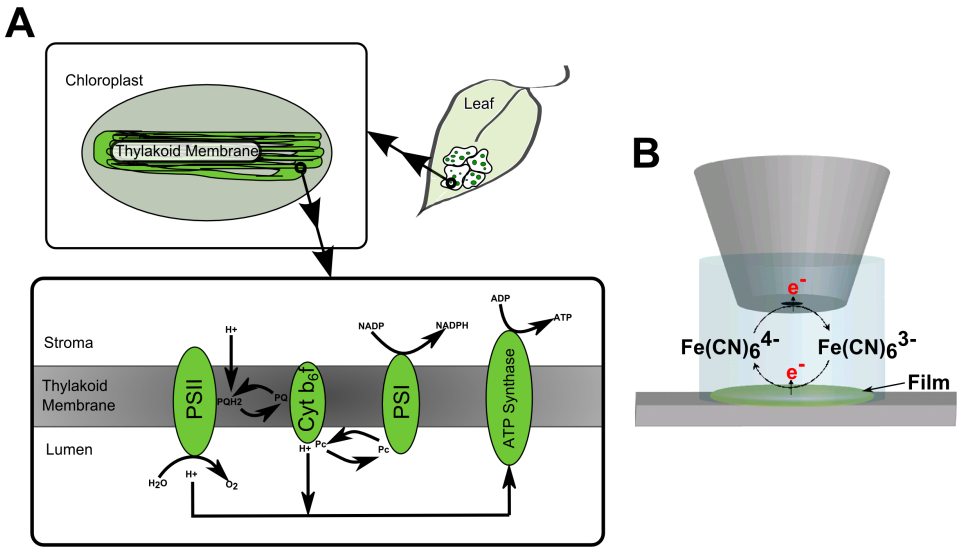

Figure 4.1: A) A simplified diagram of the light dependent components of photosynthesis are imbedded within the thylakoid membrane, which is contained within the chloroplast, which is its self located within plant cells in higher plants. The primary components of the photosynthetic pathway consists of the photosystem II (PSII), cytochrome b6f complex (cyt b6f), photosystem I (PSI) and ATP synthase. PSII uses the energy from adsorbed photons to split water, resulting in the generation of oxygen, a proton and an electron. This electron is transferred to cyt b_6f by plastoquinone (PQ), while also pumping protons across the membrane. This is then transferred on to PSI by plastocyanin (Pc). PSI, though intermediate proteins, uses this and energy from adsorbed photons to convert NADP to NADPH. ATP Synthase uses the generated proton gradient to convert ADP to ATP. B) A schematic of the generation of ferrocyanide at the substrate and its collection at the electrode tip.

In terms of flux measurements, scanning electrochemical microscopy (SECM) is particularly suited to detect a wide range of redox-active species with high spatial and temporal resolution.[14–18] A small electrode (tip) is immersed in solution close to a sample and the current response at the electrode, arising from electrochemical

processes taking place at the electrode, is recorded. A diagram of a typical SECM tip investigating a redox process ($Fe(CN)_6^{4-/3-}$) at a surface is shown in Figure 4.1 B. The spatial resolution of SECM is governed by the size of the electrode, which is typically in the region of 100 nm - 25 μm,[14] and the distance of the tip from the surface.[19] The geometry of the SECM tip, and the ability to place the tip at a defined distance from a sample, allows the flux of the redox-active species at the sample to be calculated from the current measured at the SECM tip, by solving the underlying mass transport problem.[20–22]

SECM is proving increasingly popular for studying living cell monolayers and individual cells.[23–31] Particularly relevant to this study are previous reports on aspects of photosynthesis, for example, measurements of the local oxygen flux from single stomata of Brassica juncea[32] and the local oxygen flux above individual guard cells in intact plant leaves.[33] Two-dimensional imaging of the oxygen evolution from a single protoplast[34] (a plant cell with the cell wall removed) and quantification of the steady-state oxygen generation from single protoplasts[35,36] has also been reported. An individual component of the light-dependent photosynthetic pathway, photosystem I, has been investigated electrochemically[37] and using SECM.[38] These studies have tended to provide measurements of steady-state oxygen generation rates, but have not exploited the ability of SECM to investigate processes with exquisite time resolution, an aspect we demonstrate to be particularly powerful for the studies herein.

SECM has also been used to measure local oxygen evolution using a small electrode inserted into the protoplast.[36,39] The insertion of an AFM tip with an integrated electrode into single algal cells and chloroplasts has also been recently demonstrated, with the direct extraction of electrons from the photosynthetic pathway and oxygen evolution in the cytosolic space reported.[40–42]

The fragile nature of individual chloroplasts makes them prone to lysis, and so it is important to establish the state of the chloroplasts within the experimental

configuration. Oxygen evolution in the presence of ferricyanide is a well established method for measuring the proportion of burst chloroplasts in an ensemble.[43–46] Ferricyanide is a well-known anionic, non-physiological electron acceptor (producing ferrocyanide) which can only freely interact with thylakoids upon bursting of the chloroplast envelope.[47] Once through the chloroplast envelope, the impermeability of the thylakoid membrane enables the ferricyanide/ferrocyanide redox couple to act only on the stromal side of photosystem II (PSII).[48–50] This reaction involves the light-driven transfer of electrons from water to the ferricyanide/ferrocyanide couple, with concomitant evolution of oxygen. This enables envelope intactness to be determined by measuring the flux of ferrocyanide generated under illumination.

The goals of this paper were several-fold: first, to use the SECM methodology to assess whether chloroplast (and by extension thylakoid membrane) films are a viable configuration in which to study photosynthesis. Such a configuration opens up the possibility of high resolution measurements of individual chloroplasts and thylakoid membranes. This was carried out by assaying the intactness of a chloroplast film by the electrochemical detection of ferrocyanide before and after osmotically shocking the film to burst all of the organelles. Second, we determine the oxygen evolution and consumption at isolated, immobilized chloroplast and thylakoid membrane films during photosynthesis by the direct detection of the oxygen. The temporal resolution of SECM allowed local oxygen generation and consumption rates to be measured on much shorter timescales than previously. Kinetic data are extracted, analyzed and interpreted by developing a finite element method (FEM) simulation, which faithfully represents the physicochemical processes and mimics the geometry of the SECM configuration. In addition, the effect of Mg^{2+} and Cl^{-}, which are thought to play a role in photosynthesis,[51–54] at chloroplast films is assessed. Finally, and with an eye to the future, we demonstrate the use of SECM to determine the turnover rate of the ferricyanide/ferrocyanide redox couple on a single thylakoid membrane.

4.3 Experimental

4.3.1 Instrumentation

An SECM mounted either on a confocal/fluorescence microscope (TCS SP5 MP, Leica) or an inverted microscope (Axiovert 25, Zeiss) was used for these studies. The electrode was positioned using micropositioners (Newport Corp) for coarse control and piezoelectric positioners, either a Nanocube P-611.3S (Physik Instrumente) or Trito 100 (Piezosystems Jena), for fine control. A two-electrode setup was used for dynamic electrochemical measurements, with the current measured using either a home-built current follower through a FPGA card (PCIe-7852R, National Instruments) controlled by LabVIEW software (LabVIEW 2011, National Instruments) or a potentiostat (CH730A, CH Instruments). The working electrode was the SECM tip, typically a 25 μm diameter Pt or Ag disk-ultramicroelectrode (UME), and a AgCl-coated AG wire was used as a quasi-reference counter electrode (QRCE), against which all potentials are quoted. The sample was illuminated by either the fluorescence microscope, with an I3 filter set (Leica, band pass filter 470 $\pm$ 20 nm and dichroic mirror 510 nm), or a halogen lamp (HL-2000-HP-232, Ocean Optics), with a 650 $\pm$ 80 nm bandpass filter, which was controlled via a personal computer (Faulhaber motion manager 2). The light intensity was measured using a silicon detector photodiode (NT 53-375, Edmund Industrial Optics). Confocal laser scanning microscopy (CLSM) of individual chloroplasts and thylakoid membranes was obtained with a Zeiss LSM 510 microscope, using a water immersion objective lens (Zeiss, Achroplan 63 $\times$ / 0.95 W) with an argon laser (λ = 488 nm) and 505 nm long pass filter.

4.3.2 Materials and Chemicals

Solutions: HS (50 mM HEPES (Sigma-Aldrich), 0.33 M sorbitol (Sigma-Aldrich) and KOH (Sigma-Aldrich) to adjust the pH to 8.0), 2$\times$HS (100 mM HEPES, 0.66

M sorbitol and KOH to adjust the pH to 8.0) and 5×HS (250 mM HEPES, 1.65 M sorbitol and KOH to adjust the pH to 8.0) buffers made in Milli-Q reagent grade water (resistivity of 18.2 MΩ cm at 25°C) was used for studies. HS+ buffer, HS buffer plus 2 mM EDTA (ethylenediaminetetraacetic acid (Sigma-Aldrich)), 1 mM $MgCl_2$ (Sigma-Aldrich) and 1 mM $MnCl_2$ (Sigma-Aldrich), was also used for chloroplast films. HM buffer (10 mM Hepes, 5 mM $MgCl_2$ (Sigma-Aldrich) and KOH to adjust the pH to 8.0) in Milli-Q reagent grade water was used for thylakoid membrane films. Percoll pads (2 ml of 5×HS buffer, 3.5 ml Percoll (Sigma-Aldrich), 4.5 ml H2O) were used in the preparation of the chloroplasts. Poly-L-lysine (PLL) (Sigma-Aldrich) was used to prepare the slide surfaces onto which chloroplasts and thylakoids were immobilized. Ferricyanide ($Fe(CN)_6^{3-}$, Fischer Chemicals) as the potassium salt was used as purchased.

Samples: Chloroplasts were isolated from 8 to 9 day old peas (*Pisum sativum*, var. Kelvedon Wonder) by the mechanical disruption method.[55] In brief, leaves were homogenized using a Polytron blender (Kinematica GmbH) in HS buffer, before being filtered through a double layer of Microcloth (Calbiochem) and centrifuged at 3300 g for 2 minutes. The chloroplast pellet was re-suspended in 2 ml of HS buffer and transferred onto a Percoll pad, centrifuged at 1400 g for 8 minutes and the supernatant discarded. The pellet was resuspended in 10 ml HS buffer, centrifuged at 3000 g for 2 minutes before being finally re-suspended in a minimum volume (0.5 - 0.8 ml) of HS buffer. The chlorophyll content was determined spectrophotometrically using the method of Arnon[56] and adjusted to 2.0 mg/ml. Thylakoid membranes were extracted from the chloroplast solution by taking 0.4 ml of chloroplast solution, centrifuged at 7000 rpm for 2 minutes and re-suspending in HM buffer for 5 minutes on ice to osmotically lyse the organelles. The lysed chloroplasts were washed twice in HS buffer and once in HM buffer by centrifuging at 14,000 rpm for 2 minutes. The thylakoid membranes were finally re-suspended in 0.4 ml HM buffer at a concentration of 2 mg/ml chlorophyll.

Deposition: Chloroplasts and thylakoid membranes were immobilized onto PLL covered slides, which were prepared by sonicating microscope slides in acetone and then water for 10 minutes, followed by drying with nitrogen and immersion in 0.1% (W/V) PLL solution for 5 minutes, and finally curing for 1 hour at 60 °C. 10 μl of either the chloroplast suspension or thylakoid membrane suspension was deposited onto each slide. After two to three minutes for the films and 30 seconds for the individual isolated thylakoid membranes, the slide was gently rinsed twice with the appropriate buffer. The films were relatively uniform and of high coverage, as shown by the inverted optical microscope images shown in Figure 4.2 A and B. Analysis of the optical images allowed the surface coverage to be determined as *ca.* 3.5×10^6 chloroplasts/cm^2 or 2.5×10^6 thylakoid membranes/cm^2. To further confirm the deposition of the chloroplast and thylakoid membrane films, CLSM z-stacks of individual chloroplasts and thylakoid membranes, shown in Figure 4.2 A and 2B respectively, were obtained using the intrinsic fluorescence of chlorophyll. These confirm the height dimensions expected of individual chloroplasts (4 - 5 μm) and thylakoid membranes (2.5 - 3.5 μm), and show clearly that immobilization results in the formation of a monolayer.

SECM Methods. All measurements were made in solutions which had been pre-chilled with solution temperatures between 4 and 6 °C during experiments. Prior to measurements, the electrochemical cell was typically equilibrated in the dark for 5 to 10 minutes and the Pt working electrode tips were pre-oxidized at 1.2 V for 10 seconds to activate them prior to measurements, while Ag UMEs were used without further pretreatment (after polishing with fine alumina powder).[57] The SECM tips were typically positioned at a distance of 12.5 μm (which corresponded to one electrode radius) above the sample by using the diffusion-controlled reduction of oxygen or ferricyanide (negative feedback control) for distance control.[22,58]

Chloroplast Intactness: The 25 μm diameter Pt disk UME was used to detect the production of ferrocyanide before and after osmotically shocking chloro-

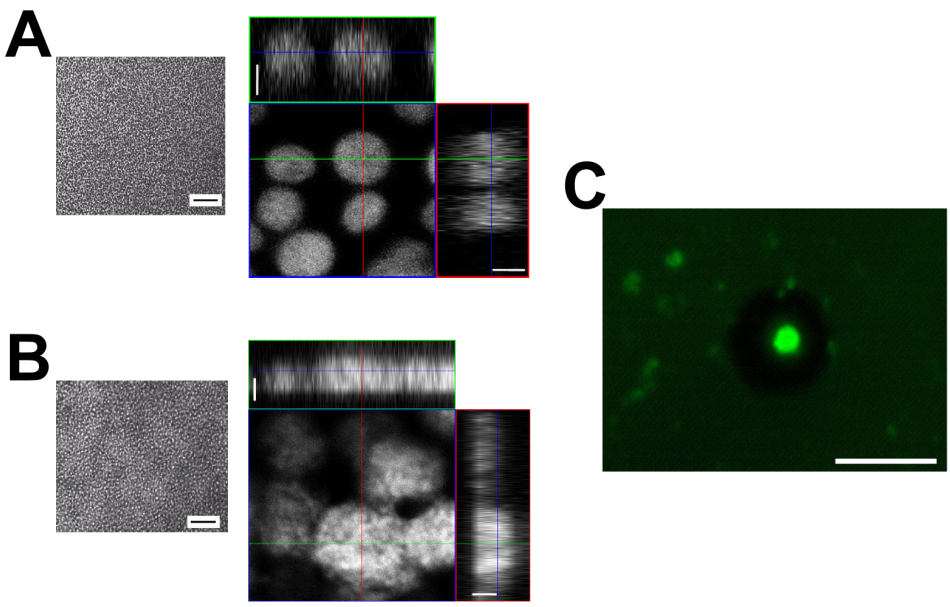

Figure 4.2: A) Optical (left) and z-stack confocal (right) images of chloroplast films. B) Optical (left) and z-stack confocal (right) images of thylakoid membrane films. Scale bar is 50 μm on the optical images (left of A and B) and 2 μm on the confocal microscopy images (right of A and B). C) A single thylakoid membrane seen as the bright green spot in the middle of the image, with a 25 μm diameter Pt disk electrode, seen as the dark halo around the thylakoid membrane, placed 12.5 μm above (see text). Scale bar 25 μm.

plast films during illuminated (650 nm, flux of 9.4×10^{14} photons cm^{-2} s^{-1}). The process of osmotically shocking the chloroplasts, adapted from that of Lilley et al.,[59] involved soaking the film of immobilized chloroplasts in a solution containing only 10 mM $MgCl_2$ for 1 minute, followed by the addition of double strength HS+ buffer. This was then replaced by HS buffer containing 1 mM ferricyanide as the redox mediator.

Oxygen Evolution/Consumption: The rate of oxygen evolution or consumption by immobilized chloroplast films, in HS and HS+ buffers, and thylakoid membrane films in HM buffer was monitored with an Ag disk UME with an SECM system mounted on an inverted microscope (*vida supra*). The electrode was used to monitor the local oxygen flux as the chloroplast, or thylakoid membrane, films were illuminated (650 nm at a maximum intensity of 9.4×10^{14} photons cm^{-2} s^{-1})

at four different light fluxes (16%, 26%, 60%, and 100% of maximum, as measured by the silicon photodiode), achieved using neutral density filters. The current-time transient responses for oxygen reduction at the electrode are presented relative to the background response for oxygen reduction at the electrode in the dark, typically 4 ± 0.3 nA (measured accurately immediately before and after illumination), which was subtracted.

Single Thylakoid Membrane Studies: A Pt disk UME was positioned above an individual isolated thylakoid membrane using the fluorescence microscope to aid lateral positioning. The tip was held at a potential (0.2 V) for the diffusion limited oxidation of ferrocyanide to ferricyanide, measured as a function of time, as the sample was illuminated (at 470 nm) at high light intensity (3.2×10^{16} photons cm^{-2} s^{-1}) through the fluorescence microscope, so as to saturate the photosynthetic pathway, without and with 3.3 mM ferricyanide present. Note, the single thylakoid membrane sample is illuminated using a different wavelength of light than the films, so to maximize photochemical efficiency. A typical optical image of a electrode positioned over a single thylakoid membrane is presented in Figure 4.2 C, which illustrates that lateral positioning of the UME over a single thylakoid membrane, as described, can be achieved with high accuracy.

4.4 Theory and Simulations

Oxygen is generated, as part of the light controlled photosynthetic electron transport pathway, from water splitting at the stromal side of photosystem II. The primary electron acceptor at PSII is plastoquinone (PQ), which accepts electrons (and protons) to become double reduced and protonated, diffuses within the thylakoid membrane, and then donates the electrons to cytochrome bf and protons to the thylakoid lumen. The oxidized PQ must then diffuse back to PSII in order to accept another electron in the chain. However, there is a limited number of PQ molecules

present, and under conditions where more energy is absorbed, and so electrons produced, than can be translated, the pool of PQ becomes reduced and acts to block electron transfer.[1,2,60,61] This, in turn, causes photoinhibition, which is the regulation and inactivation of PSII and its associated proteins.[60–63] Therefore at the short time periods, which we probe herein, oxygen production largely depends on the oxidization state of the PQ pool.[64–67]

4.4.1 Chloroplast Film Oxygen Generation

We develop FEM simulations based on a kinetic model in which the rate of oxygen generation at the chloroplast film depends on the concentration of oxidized PQ species (N_t) which are consumed (kinetic constant k_f) to produce a reduced PQ species (R_s), but are also regenerated (kinetic constant k_b) to produce the oxidized species.

$$N_t \underset{k_b}{\overset{k_f}{\rightleftharpoons}} R_s \tag{4.1}$$

Therefore the number of oxidized PQ species, N_t, at time t, where t is the time after the illumination, is:

$$\frac{\partial N_t}{\partial t} = -k_f N_t + k_b(N_0 - N_t) \tag{4.2}$$

where N_0 is the total number of available oxidized PQ species. The above equation can be integrated to give the number of PQ species at time t and therefore the flux of oxygen at the chloroplast film (boundary 3 in Figure 3), J, is:

$$J = \frac{k_f N_0(k_b + k_f \exp^{-(k_b+k_f)t})}{k_b + k_f} \tag{4.3}$$

4.4.2 Thylakoid Membrane Film Oxygen Generation

Thylakoid membranes lack many of the stabilizing components of the photosynthetic pathway, and so the initial oxygen generation, before any limiting factors,

was investigated and simulated. By focusing on the shortest times, a zeroth order rate constant was used for the generation of oxygen. Thus, the oxygen flux on the film boundary is set directly.

4.4.3 FEM Simulations

FEM simulations were developed using Comsol Multiphysics 4.3 (Comsol AB) on a 64 bit personal computer. The mass transport of oxygen within the SECM axisymmetric cylindrical configuration is confined to diffusion-only transport, and, as such, is described by Ficks second law:

$$\frac{\partial c}{\partial t} = D\nabla^2 c \tag{4.4}$$

where c is the concentration of oxygen, t is time, D is the diffusion coefficient of oxygen, which is set to 1.77×10^{-5} cm^2 s^{-1}.[68] The tip-current response was simulated using initial conditions and the appropriate boundary conditions representing the experimental and geometrical constraints of the system. The simulation domain and the boundary conditions are illustrated in Figure 4.3. The initial oxygen concentration within the domain of the simulation was set to 0.25 mM,[69] appropriate for aerated aqueous electrolyte solution.

The boundaries shown in Figure 4.3 have the following conditions (n is the surface normal). Boundary 1 represents the axial symmetry in the cylindrical system, and so is set to have no normal oxygen flux ($\nabla c.n = 0$). Boundary 2 is the electrode, at which the oxygen concentration is zero because the electrode is held at a potential to reduce oxygen at a transport-limited rate ($c = 0$). Boundary 3 represents the substrate containing the chloroplast or thylakoid membrane films, so the flux of oxygen at this boundary is time and light dependent and is governed by a rate law described in detail above. Boundaries 4 and 5 represent the glass surrounding the electrode, and have no normal flux ($\nabla c.n = 0$). Boundary 6 and 7

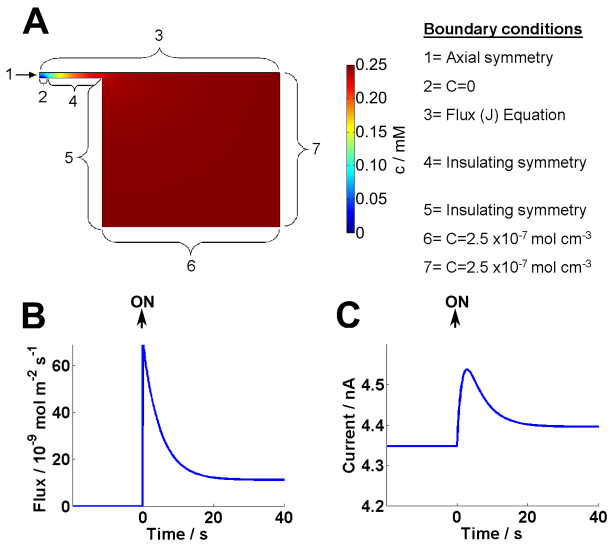

Figure 4.3: A) The geometry and boundary conditions of the finite element model of a 25 μm diameter disk electrode situated 12.5 μm above an active surface. Axial symmetry reduces the problem to a two dimensional domain. Boundary 1 is the axis of symmetry, boundary 2 is the electrode, boundary 3 is the chloroplast or thylakoid membrane film, boundaries 4 and 5 are the glass surrounds of electrode and boundaries 6 and 7 are the bulk solution. The color map shows the steady state oxygen concentration profile in the dark. B) Typical oxygen flux at the chloroplast or thylakoid membrane film (boundary 3) applied as part of the FEM simulation. C) Typical oxygen reduction current at the electrode (boundary 2) calculated from the FEM simulation.

represent the bulk solution, and are set to the bulk oxygen concentration ($c = 0.25$ mM).

The tip was held at a potential to detect oxygen naturally present in solution, before the light was switched on, and so the simulations evaluate this current which was allowed to reach steady state, with no oxygen flux at the chloroplast or thylakoid membrane films (boundary 3 condition set to $\nabla c.n = 0$). A typical example of the simulated oxygen concentration profile prior to illumination is illustrated in the FEM geometry in Figure 4.3 A. Upon illumination an oxygen flux is applied at the substrate and a current, from the reduction of oxygen, generated at the electrode. A typical simulated flux, and corresponding current response, is shown in Figure 4.3 B and C, respectively. The current at the electrode, i_{tip}, was determined from

the integral of the normal flux of oxygen at the electrode surface multiplied by the Faraday constant and the number of electrons in the reduction of oxygen (which was 4).

4.5 Results and Discussion

4.5.1 Chloroplast Intactness Measured Through Accessibility to Ferricyanide

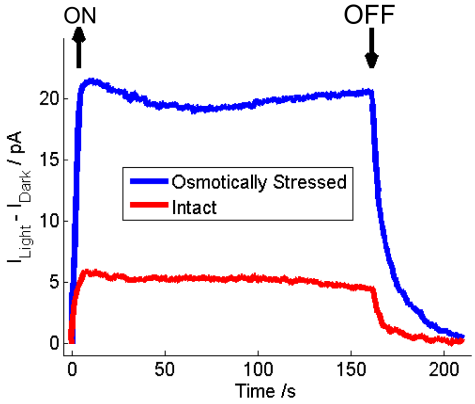

Figure 4.4: Current for the oxidation of ferrocyanide at a 25 μm diameter Pt disk electrode, held 12.5 μm above a film of isolated chloroplasts, in an HS buffer containing 1 mM ferricyanide, prior to, and after, osmotically shocking the chloroplasts. $\uparrow$ represents light on and $\downarrow$ represents light off.

The percentage of intact chloroplasts in a film immobilized on PLL covered glass slides was determined by comparing the current responses for the oxidation at the tip of ferrocyanide, generated at the chloroplast film during illumination, before and after osmotic shocking the chloroplasts in the film. Figure 4.4 shows example current-time traces for intact and osmotically shocked chloroplasts. The response upon illumination is fast, but finite, and is a combination of the response time of the photosynthetic system to illumination and the time taken for the ferrocyanide to diffuse from the substrate to the electrode, although the diffusion from the substrate to the electrode contributes most. The chloroplast envelope is known to be fairly

impermeable to ferricyanide,[47] but once the envelope has been ruptured, through osmotic shock, ferricyanide can freely diffuse to the thylakoid membrane and accept electrons at PSII.[48,50] The detection of ferrocyanide at the electrode demonstrates that the chloroplast envelope has been ruptured and that ferricyanide has been reduced at the illuminated thylakoid membrane.

The difference in the amount of ferrocyanide detected between the intact and osmotically shocked chloroplasts allows us to establish the percentage of intact chloroplasts in the immobilized film as ca. 75 %, by taking the ratio of current measured during illumination at intact and broken chloroplasts. It has been well documented that an average intactness of 70 - 80 % in solution is sufficient for studying photo-electron transport processes in chloroplasts and is typical for this method of chloroplast isolation.[43] Thus, the immobilization of the chloroplasts to a solid support results in minimal further rupture of the chloroplast envelope and allows the ready study of the photosynthetic pathway in this configuration.

4.5.2 Oxygen Evolution at Chloroplast Films

Oxygen evolution from chloroplast films without any artificial electron acceptors in solution was detected at an electrode placed close to the films upon illumination. Oxygen evolution is the result of the photolysis of water occurring during the light reactions at PSII. Figure 4.5 A shows example current transients for diffusion-limited oxygen reduction at an Ag UME positioned above a chloroplast film in isotonic HS at the four light intensities. As mentioned above, oxygen is detected at the SECM tip in the dark, as it is present naturally, and all currents are presented with respect to this. Figure 4.5 B shows the effect of the addition of $MgCl_2$, $MnCl_2$ and EDTA, present in the HS+ buffer, on the oxygen generation at chloroplast films. Mg^{2+} have been shown to play a role in photochemical activity and oxygen evolving rate,[51,54] and the stability of the chloroplast envelope.[70] While the need for chloride anions has been the subject of much debate.[52,71,72] EDTA is added as a chelating agent,

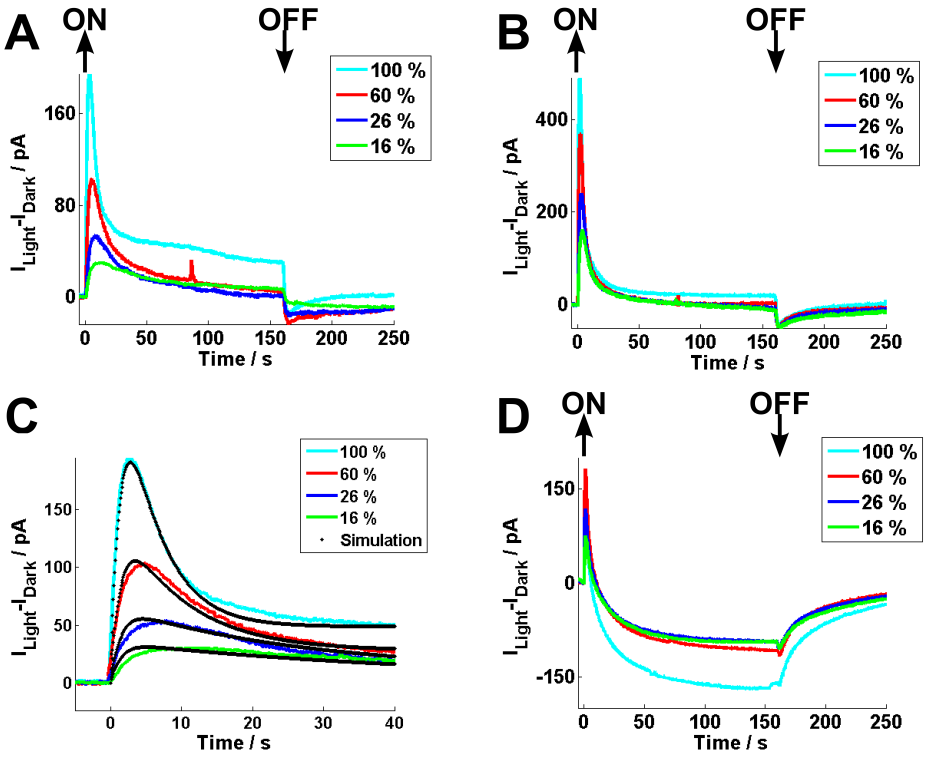

Figure 4.5: A) Current response from a 25 μm diameter Ag disk electrode held 12.5 μm above a chloroplasts film on a PLL covered substrate for the reduction of oxygen in HS buffer as the sample is illuminated at four different light intensities (100%, 60%, 26% and 16%). B) Current response from a chloroplast films, at a 25 μm diameter Ag disk electrode held 12.5 μm above a chloroplasts film, in HS+ buffer. C) The simulated current response, with the experimental data, for the oxygen reduction at the chloroplast film in HS buffer. The rates calculated from fitting the model to the data is shown in Table 1. D) The current response for the reduction of oxygen at a 25 μm Ag disk electrode held 12.5 μm above a thylakoid membrane film on a PLL covered substrate in HM buffer. $\uparrow$ represents light on and $\downarrow$ represents light off.

scavenging excess metal ions which are potentially detrimental.

Upon illumination of the immobilized chloroplast films a sharp increase (spike) in oxygen flux at the electrode was observed in both buffers. This spike in oxygen concentration rapidly decayed to a much lower steady-state net oxygen evolution rate which remained fairly constant until the illumination period was complete. Interestingly, oxygen consumption by the chloroplasts was observed when the

light was turned off. Increasing light intensity resulted in the initial oxygen concentration spike reaching larger current values, for example increasing from 30 pA to 190 pA with an increase of light intensity from 16 % to 100 %. The quasi steady-state oxygen generation during illumination showed a positive correlation with light intensity. The oxygen consumption at the end of the illumination period was virtually non-existent at low light intensities but became more apparent as the light intensity increased. Oxygen generation was larger in the HS+ buffer as compared to the HS buffer, with the lowest light fluxes (16 % and 26 %) showing a 5-6 times difference. These effects are consistent with the enhanced photosynthetic activity in the presence of the Mg^{2+} ions,[51,54,70] or could also have been due to the presence of chloride ions which has been thought to play a crucial role in the water splitting complex.[52,71,72]

The appearance of the initial oxygen concentration spike has been reported previously, with Fork observing an initial oxygen spike while investigated oxygen exchange at chloroplasts in solution in the absence of a Hill oxidant using a macro scale Clark type oxygen electrode[73] and Matsue observing an initial intracellular oxygen spike in algal protoplasts using micro electrodes with ring radii of approximately 2 μm.[35,36] The oxygen spike was attributed to the consumption of the limited number of, then unknown, electron acceptors by Fork, and to the consumption of the limited number of terminal species (such as NADP) by Matsue. However, we observe an initial oxygen concentration spike of the same magnitude over both chloroplast and thylakoid membrane (discussed below) films, suggesting that the limiting factor responsible for the initial oxygen concentration spike is not the terminal electron acceptors which are not present in the thylakoid membranes but a component of the linear electron transport pathway that is present in both systems, and we suggest that it is, in fact, the limited size, and regeneration, of the PQ pool.

The oxygen consumption after completion of the illumination period is most likely the result of oxygen acting as an electron acceptor at PSI, upon depletion

of the terminal electron acceptor, NADP, a process commonly referred to as the Mehler reaction.[1,2]

Table 4.1: Oxygen evolution rates of chloroplast films, in HS and HS+ buffers, calculated from fitting the finite element model to the experimental data.

Buffer	Light Intensity	N_0 / mol cm^{-2} ($\pm$ 0.01 $\times$ 10^{-11})	k_f / s^{-1} ($\pm$ 0.01)	k_b /s^{-1} ($\pm$ 0.01)
HS	100 %	4.05×10^{-11}	0.17	0.03
HS	60 %	3.75×10^{-11}	0.09	0.02
HS	26 %	4.79×10^{-11}	0.03	0.01
HS	16 %	4.0×10^{-11}	0.02	0.01
HS+	100 %	4.2×10^{-11}	0.84	0.02
HS+	60 %	4.35×10^{-11}	0.43	0.01
HS+	26 %	3.99×10^{-11}	0.25	0.01
HS+	16 %	3.79×10^{-11}	0.15	0.01

Using a FEM simulation the rate of oxygen evolution over the initial forty seconds of illumination at the chloroplast film, for both HS and HS+ buffers, was calculated. The first 40 seconds was chosen in order to incorporate the initial oxygen concentration spike and its subsequent decrease to a steady-state oxygen evolution current. The evolution of oxygen is based on the rate of consumption (k_f) and regeneration (k_b) of PQ, and the simulated response for the oxygen evolution in HS buffer is illustrated in Figure 4.5 C. The calculated rate constants (k_f, k_b and N_0) are shown in Table 4.1. These results show a proportional relationship between k_f and light intensity. This was expected due to oxygen evolution being centered on a light driven process in photosynthesis. The initial oxygen generation depends on the forward rate constant, k_f, but the longer time response depends on the regeneration of the limited PQ pool, k_b. Interestingly, the total amount of PQ, N_0, which we calculated as part of the model was fairly consistent between the different simulations.

We can compare the value of the total amount of PQ, N_0, to what we should expect within a chloroplast monlayer. We do so by using the ratio of the moles of chlorophyll to PQ in chloroplasts and from the ability to determine the surface

coverage of the slides under the electrode area from the microscopy images. The mass of chlorophyll per chloroplast is 1.01×10^{-15} moles.[67] The ratio of chlorophyll to PQ was determined as 70:1.[74] The optical microscope images, Figure 4.2 A, were used to calculate the number of chloroplasts under the probe (area of approximately 100 μm radius) and hence the total number of moles of PQ was calculated by multiplying the moles of PQ per chloroplast by the total number of chloroplasts. The effective concentration of PQ was finally determined by a division of the total moles of PQ by the area of chloroplasts under the electrode, to give a typical N_0 of *ca.* 5×10^{-11} mol cm^{-2}. This compares very well with the N_0 calculated as part of the model. This, again, reinforces the idea that it is the limited size of the PQ pool, and its state, that generates the oxygen generation profile.

4.5.3 Oxygen Evolution at Thylakoid Membrane Films

The local oxygen concentration in a film of immobilized thylakoid membranes in HM buffer was recorded under illumination. Thylakoid membranes contain the light-driven components of photosynthesis and are usually contained within chloroplasts; however isolated thylakoid membranes lack many other components of photosynthesis, most importantly the terminal electron acceptor, NADP. In the absence of an artificial electron acceptor, the oxygen concentration generated by the thylakoid membranes, when illuminated, was found to be similar at short times but different at long times when compared to that measured from intact chloroplasts. This is evident in Figure 4.5 D, which shows the current measured at an Ag electrode above a film of thylakoid membrane, at a series of different light fluxes. An initial cathodic spike at the electrode, corresponding to oxygen generation, was observed upon illumination. This initial oxygen concentration spike increased with increasing light intensity, as found for the films of chloroplasts. However, the spike was followed by a rapid decrease of oxygen flux at the electrode to a level which indicated oxygen consumption by the thylakoid membranes. A steady-state current was obtained af-

ter approximately 60 seconds of illumination for this net oxygen consumption. The current measured at the tip, indicative of steady-state oxygen consumption, was found to increase with light intensity. Once the illumination period of 160 seconds was complete the local oxygen flux at the electrode (tip current) returned to the dark steady-state current value.

As mentioned above, in the absence of the chloroplast envelope, as is the case with thylakoid membranes, crucial enzymes and redox mediators, such as NADP and ADP, are lost. It has been observed that during times of limited availability of such mediators, in particular electron acceptors for PSI, oxygen itself can act as the terminal electron acceptor.[1,2] The domination of oxygen consumption by the thylakoid membranes, at long times, following its generation, at short times, can be attributed to oxygen taking over as the main terminal electron acceptor and hence a competition is established between oxygen production and consumption.

In past work, the initial oxygen concentration spike, which was observed with the chloroplast films (see above), has been ascribed to the rapid consumption of the limited number of terminal electron acceptors,[35,36] However, we have observed that the initial oxygen concentration spike is of the same magnitude in both chloroplasts and thylakoid membranes. If the lack of terminal electron acceptors was responsible for controlling the oxygen generation rate then within thylakoid membranes one could reasonably have expected it to be significantly different (slower and less extensive) as compared to chloroplasts. As we have discussed, it is perhaps more reasonable to consider the oxidation state of the PQ pool, and its size, to control the initial photo generation of oxygen in both chloroplasts and thylakoid membranes.

The oxygen production rate was calculated at each of the four light intensities over the initial few seconds, therefore focusing on oxygen generation before the influence of any limiting factors such as oxygen acting as an electron acceptor. The calculated rate constants are given in Table 4.2 as the rate constant, k, divided by the total amount of PQ, (N_0, 4×10^{-11} mol cm^{-2}). The rate constants for oxygen

Table 4.2: Oxygen evolution rates for the initial 1 second of oxygen generation of thylakoid membrane films calculated by fitting the finite element model to experimental data.

Light Intensity	k/N_0 / s^{-1} ($\pm$0.01)
100 %	0.19
60 %	0.21
26 %	0.14
16 %	0.09

generation show an increasing trend proportional to the change in light flux, except for the 100 % light intensity which is less than expected. The rate constant for the generation of oxygen in thylakoid membrane films and the forward rate constant for chloroplasts films are broadly similar. This again suggests that it is the oxidative state of the PQ pool that controls the oxygen generation for thylakoid membranes, as opposed to the limited availability of the terminal species, NADP and ADP.

4.5.4 Single Thylakoid Membrane Ferricyanide Reduction

We now turn to the case where we monitor photosynthetic activity via the artificial electron acceptor ferricyanide, which produces ferrocyanide that is subsequently detected at the SECM tip. We investigate this process at the level of a single isolated thylakoid membrane using a 25 μm diameter Pt disk UME (as shown in Figure 4.2 C). Figure 4.6 shows typical current-time responses for the detection of ferrocyanide for the following scenarios: (a) when the electrode was placed over an individual thylakoid membrane with no ferricyanide present; (b) at the same thylakoid membrane with 3.3 mM ferricyanide present; and, (c) in the bulk solution with no thylakoid membrane but with 3.3 mM ferricyanide. Without ferricyanide present, or with the tip in bulk solution, no current is detected upon illumination of the membrane. When ferricyanide is present and the tip is directly above a thylakoid membrane, an increase in the current is measured at the electrode during illumination, indicating that ferricyanide is reduced at the thylakoid membrane and detected as ferrocyanide

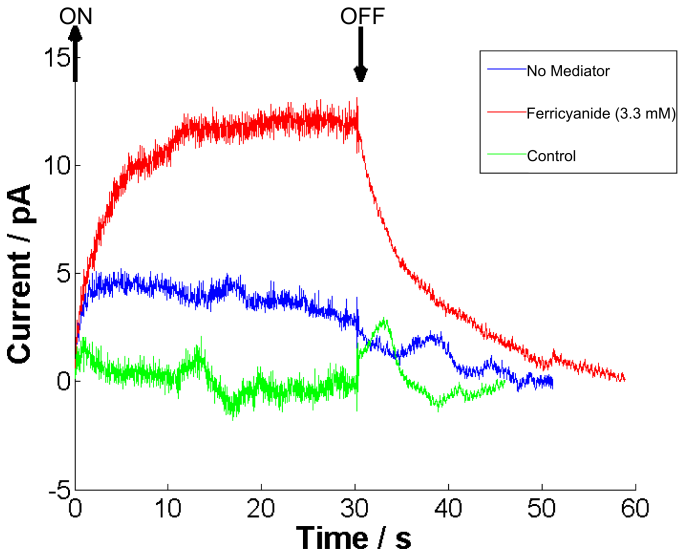

Figure 4.6: The current measured for the oxidization of ferrocyanide at a 25 μm Pt disk electrode held 12.5 μm above a single thylakoid membrane as it is illuminated for 30 seconds in the absence and presence of 3.3 mM ferricyanide, and in bulk solution with 3.3 mM ferricyanide. The detection of ferrocyanide from a single thylakoid membrane was successful 50% of the time (N $\approx$ 20).

at the electrode. The maximum current recorded corresponds to 1×10^{-16} mol s^{-1} of ferricyanide is being reduced by a single thylakoid membrane. The proximity of the electrode to the thylakoid membrane and the size of the electrode with respect to the thylakoid membrane result in the detection of close to 100 % of the ferrocyanide generated from an individual thylakoid membrane. Comparisons with the oxygen generation within films are complicated due to the use of different wavelengths of light, and intensities, to activate photosynthesis. However, this demonstrates that the activity of individual thylakoid membranes (and by extension chloroplasts) can be assessed by using a small, mobile electrode, when immobilized on a poly-L-lysine (PLL) covered substrate.

4.6 Conclusions

SECM has been demonstrated to be a powerful method for the quantitative measurement of the local flux of redox active species from isolated chloroplasts and thylakoid membranes during photosynthesis. The ability to place an electrode precisely, within a few microns of the sample, has allowed effective, real-time measurements of redox processes not only from monolayer films of chloroplasts and thylakoid membranes, but also at single isolated thylakoid membranes. SECM has also been shown to provide an assay, demonstrating that chloroplasts deposited on PLL-modified substrates suffer from minimal ruptures as determined by the measurement of the oxidation of ferrocyanide before and after osmotically rupturing.

Both oxygen generation and consumption has been determined directly at chloroplast or thylakoid membrane films under illumination. The chloroplast and thylakoid membrane films showed an initial oxygen concentration spike, with chloroplast films reverting to low steady-state oxygen production and thylakoid membrane films reverting to steady-state oxygen consumption at longer times. The spike is due to the initial rapid oxygen generation at the films, which then reduces. The underlying oxygen generation rate is most likely a result of the oxidation state of the PQ pool, and not, as previously reported, due to the limited availability of terminal electron acceptors.[35,36] The net oxygen consumption observed at long times on the thylakoid membrane films is the result of oxygen acting as a terminal electron acceptor (Mehler reaction).[1,2] The addition of $MgCl_2$, $MnCl_2$ and EDTA increases the generation of oxygen from chloroplast films, confirming that one, or more, of these do play a role in oxygen generation within photosynthesis. This aspect shows the possibility of using the SECM technique to study the role of various additives within photosynthesis.

Finite element modeling was used to calculate the dynamics of the oxygen generation rates at the films. The model of the chloroplast films takes account of

the regeneration and consumption of available oxidized species and is used model the initial oxygen generation spike and subsequent oxygen generation. Fitting the model to the experimental data shows that the rate of consumption of available oxidized species, k_f, is light dependent, while generation of the oxidized species, k_b, is not. The estimated PQ pool size compares well with values predicted from literature. The thylakoid membranes, which have lost crucial enzymes and redox mediators, present a more complicated system to model, and as such only the initial production of oxygen was considered. The oxygen generation rates, calculated using the FEM model, were consistent with those for chloroplasts, adding weight to the assumption that it is the PQ pool state, and size, which controls the initial oxygen generation rates.

4.7 Acknowledgments

We thank the EPSRC and MOAC for a studentship to K.M. P.R.U acknowledges support from a European Research Council Advanced Investigator Grant (ERC-2009-AdG247143 Quantif). Some of the equipment used in this work was obtained through the Science City Advanced Materials project with support from Advantage West Midlands and the European Regional Development Fund.

4.8 References

(1) Hall, D. O.; Rao, K. K. Photosynthesis; Cambridge University Press, 1999.

(2) Photosynthesis. A Comprehensive Treatise; A. S. Raghavendra, Ed.; Cambrideg University Press, 1998.

(3) Baker, N. R. *Annu. Rev. Plant Biol.* **2008**, 59, 89-113.

(4) Izabela, R.; Katarzyna, G.; Borys, K.; Agnieszka, M. In Photosynthesis. Energy from the Sun: 14th International Congress on Photosynthesis; Allen, J. F.; Grant, E.; Golbeck, J. H.; Osmond, B., Eds.; Springer, 2008; pp. 771-774.

(5) Vacha, F.; Bumba, L.; Kaftan, D.; Vacha, M. *Micron* **2005**, 36, 483-502.

(6) Hall, D. O.; Edge, H.; Kalina, M. *Cell* **1971**, 303, 289-303.

(7) Jensen, R. G.; J. A. Bassham *Proc. Natl. Acad. Sci. USA* **1966**, 56, 1095-1101.

(8) Shimoni, E.; Rav-Hon, O.; Ohad, I.; Brumfeld, V.; Reich, Z. *Plant Cell* **2005**, 17, 2580-2586.

(9) Kaftan, D.; Brumfeld, V.; Nevo, R.; Scherz, A.; Reich, Z. *EMBO J.* **2002**, 21, 6146-6153.

(10) Sturgis, J. N.; Tucker, J. D.; Olsen, J. D.; Hunter, C. N.; Niederman, R. A. *Biochemistry-US* **2009**, 48, 3679-3698.

(11) Dahn, D. C.; Cake, K.; Hale, L. R. *Ultramicroscopy* **1992**, 42-44, 1222-1227.

(12) Terai, T.; Nagano, T. *Curr. Opin. Chem. Biol.* **2008**, 12, 515-521.

(13) Ntziachristos, V. *Ann. Rev. Biomed. Eng.* **2006**, 8, 1-33.

(14) Edwards, M. A.; Martin, S.; Whitworth, A. L.; Macpherson, J. V.; Unwin, P. R. *Physiol. Meas.* **2006**, 27, R63-108.

(15) Sun, P.; Laforge, F. O.; Mirkin, M. V. *Phys. Chem. Chem. Phys.* **2007**, 9, 802-823.

(16) Amemiya, S.; Bard, A. J.; Fan, F.-R. F.; Mirkin, M. V.; Unwin, P. R. *Anal. Chem.* **2008**, 1, 95-131.

(17) Schulte, A.; Nebel, M.; Schuhmann, W. *Ann. Rev. Anal. Chem.* **2010**, 3, 299-318.

(18) Mirkin, M. V.; Nogala, W.; Velmurugan, J.; Wang, Y. *Phys. Chem. Chem. Phys.* **2011**, 13, 21196-21212.

(19) Bard, A. J.; Mirkin, M. V.; Unwin, P. R.; Wipf, D. O.; Wipf, David, O. *J. Phys. Chem.* **1992**, 96, 1861-1868.

(20) Amphlett, J. L.; Denuault, G. *J. Phys. Chem. B* **1998**, 102, 9946-9951.

(21) Cornut, R.; Griveau, S.; Lefrou, C. *J. Electroanal. Chem.* **2010**, 650, 55-61.

(22) Kwak, J.; Bard, A. J. *Anal. Chem.* **1989**, 61, 1221-1227.

(23) Diakowski, P. M.; Ding, Z. *Phys. Chem. Chem. Phys.* **2007**, 9, 5966-5974.

(24) Lin, Y.; Trouillon, R. R.; Safina, G.; Ewing, A. G. *Anal. Chem.* **2011**, 83, 4369-4392.

(25) Takahashi, Y.; Miyamoto, T.; Shiku, H.; Ino, K.; Yasukawa, T.; Asano, R.; Kumagai, I.; Matsue, T. *Phys. Chem. Chem. Phys.* **2011**, 13,16569-16573.

(26) Takahashi, Y.; Murakami, Y.; Nagamine, K.; Shiku, H.; Aoyagi, S.; Yasukawa, T.; Kanzaki, M.; Matsue, T. *Phys. Chem. Chem. Phys.* **2010**, 12, 10012-10017.

(27) Bard, A. J.; Li, X.; Zhan, W. *Biosens. Bioelectron.* **2006**, 22, 461-472.

(28) Beaulieu, I.; Kuss, S.; Mauzeroll, J.; Geissler, M. *Anal. Chem.* **2011**, 83, 1485-1492.

(29) Lee, C.; Kwak, J.; Bard, A. J. *Proc. Natl. Acad. Sci. USA* **1990**, 87, 1740-1743.

(30) Schulte, A.; Schuhmann, W. *Angew. Chem. Int. Edit.* **2007**, 46, 8760-8777.

(31) Bergner, S.; Wegener, J.; Matysik, F.-M. *Anal. Chem.* **2011**, 83, 169-174.

(32) Zhu, R.; Macfie, S. M.; Ding, Z. *Langmuir* **2008**, 24, 14261-14268.

(33) Tsionsky, M.; Cardon, Z. G.; Bard, A. J.; Jackson, R. B. *Plant Physiol.* **1997**, 113, 895-901.

(34) Yasukawa, T.; Kaya, T.; Matsue, T. *Anal. Chem.* **1999**, 71, 4637-4641.

(35) Yasukawa, T.; Uchida, I.; Matsue, T. *Biophys. J.* **1999**, 76, 1129-1135.

(36) Matsue, T.; Koike, S.; Abe, T.; Itabashi, T.; Uchida, I. *Biochim. Biophys. Acta* **1992**, 1101, 69-72.

(37) Faulkner, C. J.; Lees, S.; Ciesielski, P. N.; Cliffel, D. E.; Jennings, G. K. *Langmuir* **2008**, 24, 8409-8412.

(38) Ciobanu, M.; Kincaid, H. A.; Jennings, G. K.; Cliffel, D. E. *Langmuir* **2005**, 21, 692-698.

(39) Matsue, T.; Koike, S.; Uchida, I. *Biochem. Bioph. Res. Comm.* **1993**, 197, 1283-1287.

(40) Fasching, R.; Ryu, W.-H.; Bai, S.-J.; Park, J.-S.; Fabian, T.; Moseley, J.; Grossman, A.; Prinz, F. *IEEE Sensors* **2007**, 699-702.

(41) Ryu, W.; Bai, S.-J.; Park, J. S.; Huang, Z.; Moseley, J.; Fabian, T.; Fasching, R. J.; Grossman, A. R.; Prinz, F. B. *Nano Lett.* **2010**, 10, 1137-1143.

(42) Bai, S.-J.; Ryu, W.; Fasching, R. J.; Grossman, A. R.; Prinz, F. B. *Biotechnol. Lett.* **2011**, 33, 1675-1681.

(43) Hipkins, M. F. In Photosynthesis energy transduction a practical approach; Hipkins, M. F.; Baker, N. R., Eds.; IRL Press, 1986.

(44) Cerovi, Z. G.; Plesnicar, M. *Biochem. J.* **1984**, 223, 543-545.

(45) Robinson, S. P.; Wiskich, J. T. *Plant Physiol.* **1976**, 58, 156-162.

(46) Mourioux, G.; Douce, R. *Plant Physiol.* **1981**, 67, 470-473.

(47) Nakatani, H. Y.; Barber, J. *Biochim. Biophys. Acta* **1977**, 461, 510-512.

(48) Nicholls, D. G.; Ferguson, S. J. Bioenergetics; Academic Press, 2002.

(49) Barr, R.; Crane, F. L. *Plant Physiol.* **1981**, 67, 1190-1194.

(50) Banaszak, J.; Barr, R.; Crane, F. L. *J. Bioenerg.* **1976**, 8, 83-92.

(51) Shaul, O. *Biometals* **2002**, 15, 309-323.

(52) Rivalta, I.; Amin, M.; Luber, S.; Vassiliev, S.; Pokhrel, R.; Umena, Y.; Kawakami, K.; Shen, J.; Kamiya, N.; Bruce, D.; Brudvig, G. W.; Gunner, M. R.; Batista, V. S. *Biochem* **2011**, 50, 6312-6315.

(53) Critchley, C. *Biochim. Biophys. Acta* **1985**, 811, 33-46.

(54) Pier, P. A.; Berkowitz, G. A. *Plant Sci.* **1989**, 64, 45-53.

(55) Mills, W. R.; Joy, K. W. *Planta* **1980**, 148, 75-83.

(56) Arnon, D. I. *Plant Physiol.* **1949**, 24, 1-15.

(57) James, S. D. *J. Electrochem. Soc.* **1967**, 114, 1113-1119.

(58) McGeouch, C.-A.; Peruffo, M.; Edwards, M. A.; Bindley, L. A.; Lazenby, R. A.; Mbogoro, M. M.; McKelvey, K.; Unwin, P. R. *J. Phys. Chem. C* **2012**, 116, 14892-14899.

(59) Lilley, R. M.; Fitzgerald, M. P.; Rienits, K. G.; Walker, D. A. *New Phytol.* **1975**, 75, 1-10.

(60) Aro, E. M.; Virgin, I.; Andersson, B. *Biochim. Biophys. Acta* **1993**, 1143,

113-134.

(61) Müh, F.; Glckner, C.; Hellmich, J.; Zouni, A. *Biochim. Biophys. Acta* **2012**, 1817, 44-65.

(62) Vass, I. *Biochim. Biophys. Acta* **2012**, 1817, 209-217.

(63) Frigerio, S.; Campoli, C.; Zorzan, S.; Fantoni, L. I.; Crosatti, C.; Drepper, F.; Haehnel, W.; Cattivelli, L.; Morosinotto, T.; Bassi, R. *J. Biol. Chem.* **2007**, 282, 29457-29469.

(64) Joliot, P.; Johnson, G. N. *Proc. Natl. Acad. Sci. USA* **2011**, 108, 13317-13322.

(65) Kruk, J.; Strzalka, K. *Photosynth. Res.* **1999**, 62, 273-279.

(66) Kruk, J.; Karpinski, S. *Biochim. Biophys. Acta* **2006**, 1757, 1669-1675.

(67) Rochaix, J.-D. *Biochim. Biophys. Acta* **2011**, 1807, 375-383.

(68) Han, P.; Bartels, D. M. *J. Phys. Chem.* **1996**, 100, 5597-6052.

(69) Pletcher, D.; Sotiropoulos, S. *J. Electroanal. Chem.* **1993**, 356, 109-119.

(70) Liang, C.; Xiao, W.; Hao, H.; Xiaoqing, L.; Chao, L.; Lei, Z.; Fashui, H. *Spectrochim. Acta A* **2009**, 72, 343-347.

(71) Olesen, K.; Andrasson, L.-E. *Biochemistry-US* **2003**, 42, 2025-2035.

(72) Popelkov, H.; Yocum, C. F. *Photosynth. Res.* **2007**, 93, 111-121.

(73) Fork, D. C. *Plant Physiol.* **1963**, 38, 323-332.

(74) McCauley, S. W.; Melis, A. *Photosynth. Res.* **1986**, 8, 3-16.

Chapter 5

Development of Electrochemical Scanning Probe Microscopy Instruments

As described in the introduction, electrochemical scanning probe microscopy (EC-SPM) techniques use a mobile electrochemical probe to measure the local flux or concentration of redox active species at, or near, a surface or interface. EC-SPM methods have developed from scanning electrochemical microscopy (SECM)[1–7] and scanning ion conductance microscopy (SICM),[8,9] and now include a large number of related techniques such as alternating current SECM (AC-SECM),[10] shear force SECM,[11,12] intermittent contact-SECM (IC-SECM),[13] SICM-SECM,[14–17] atomic force microscopy (AFM)-SECM[18] and scanning electrochemical cell microscopy (SECCM).[19]

The Warwick Electrochemistry and Interfaces group has been at the forefront of developing and deploying new EC-SPM techniques. In particular, the group has done pioneering work on the development of AFM-SECM,[18] scanning micropipet contact method (SMCM),[20] and more recently IC-SECM,[13] SECCM[19] and SICM-

SECM.[21]

With the recent development of IC-SECM, SECCM and SICM-SECM, and an expansion of internal users, a range of new and improved EC-SPM instruments were constructed. These instruments were capable of running the new techniques (IC-SECM, SECCM and SICM-SECM) as well as the standard techniques (such as SECM and SICM). Both the hardware and software was designed so that new, currently unknown, techniques could be developed in future. A common software interface (and data format) was used so non-technical users could run, and analyse, sophisticated EC-SPM experiments

The EC-SPM instruments were developed based on the many years of experience within the group and best practice, and innovations, observed within both commercial and academic instruments. The hardware design was evolved from existing instruments, and many people contributed to this. The software was completely new and the structure is described for the first time here. I was responsible for the software design and implementation, as well as part of the hardware design.

5.1 Previous Instruments

The previous generation of EC-SPM instruments, built and used within the Warwick Electrochemistry and Interfaces group, were designed for the SECM, SICM and TPM-SECM techniques and have been described previously.[13,19] A number of EC-SPM instruments are available from commercial suppliers, such as UniScan, CH Instruments, HEKA, Princeton Applied Research and Sensolytics. These are general instruments which are capable of a range of techniques such as SECM, SICM, scanning vibrating electrode technique, scanning kelvin probe, scanning droplet system, etc.

5.1.1 Probe Positioning

The previous instruments within the group worked in a probe scanning configuration in which the sample was held still and the probe was moved, in three dimensions, over the sample. Fine control of the probe was achieved using three piezoelectric positioners while coarse control was achieved with manual micropositioners or computer controlled stepper motors. Interestingly, a number of other research groups use a sample scanning mode where the probe was held still and the sample moved [22,23] or the sample was moved laterally and the probe moved normal to the surface. [21]

Commercial instruments typically offer an integrated positioning system using both stepper motors and piezoelectric positioners. Of note is the instrument offered by Sensolytics which offers advanced nanoscale tip positioning through the use of shear force SECM. [24]

5.1.2 Electrochemical Measurements

Previous instruments measured electrochemical signal (current or potential) using either custom made bipotentiostats (and galvanostats) or commercial bipotentiostats (CH instruments). The custom instrumentation proved to have higher resolution and bandwidth compared to commercial instrumentation. Other research groups use commercially available equipment.

5.1.3 Shielding

The electrochemical signals measured during EC-SPM can be small, typically in the order of pA. Therefore, all previous instruments were mounted within a Faraday cage, to cut out electrical interference, which is lined with acoustic foam, to cut out acoustic interference, on granite slabs, which cut out vibrations. Recently, a temperature controlled instrument has been shown to reduce the thermal drift of piezoelectric positioners and so improve the spatial resolution. [25]

5.1.4 Data Acquisition and Control

The previous instruments within the group were controlled, and data measured, through either data acquisition (DAQ) or field programmable gate array (FPGA) cards from PCs running LabVIEW (National Instruments). The LabVIEW software platform proved to be flexible with powerful inbuilt functions and libraries for communicating with hardware. In addition, it is conceptually one of the simplest programming languages to learn, as it is a visual programming language, which is important for users who are not from a computing/programming background. Previous EC-SPM instruments have used a variety of different methods to communicate with the hardware, for instance some piezoelectric positioners were controlled through a dedicated digital board while others were controlled through external amplifiers/servos from the DAQ/FPGA card. However, DAQ and FPGA cards work differently and require different software solutions. The end result was different instruments used different code and innovations/improvements could not be easily or quickly replicated across instruments.

The use of DAQ cards with a multiplexed sampling architecture restricted the rate of concurrent sampling of multiple channels. Within a multiplexed DAQ card many channels are sampled one after another by a single amplifier and analog to digital converter circuit. This restricts the sampling frequency when multiple channels are sampled. Interference between channels can, and has, been observed using existing DAQ cards.

A FPGA is a reprogrammable silicon chip that allows customised dedicated parallel logic to be embedded within the hardware. This allows fast and flexible computations, such as data filtering and probe movement logic, to be completed on the chip. The FPGA cards employed use a dedicated amplifier and analog to digital converter circuit for each channel and so allow fast data sampling rates (up to 750 kHz) of multiple (up to 8) channels. FPGA based systems, which offer faster data acquisition and control, are starting to be used by other research groups and are

also used in commercial AFM instruments.[26–28]

5.1.5 Scanning Schemes

All EC-SPM instruments control the position of the probe with respect to a surface, frequently with a feedback response generated by applying an oscillating signal to the probe. A number of different methods to move a probe across the surface have been reported with a line scan pattern[15,16,19,29] and a picking or hopping mode[27,28,30,31] being popular.

5.2 Design

The new EC-SPM instruments were designed based on improvements to the existing instruments and innovations observed in other instruments. These instruments were capable of running both the new and standard EC-SPM techniques. However, they were also flexible to allow the development of new techniques and probe movement schemes. A number of interesting techniques, such as AFM-SECM and shear force SECM, require specialized equipment and so were not accommodated.

Piezoelectric positioners were used for nanoscale probe positioning. A sample scanning scheme was used where possible. Within the sample scanning scheme the sample was mounted on two piezoelectric positioners that allow the lateral movement and the probe was mounted on a separate piezoelectric positioner that moves the probe normal to the surface. This splits the axis which is usually oscillated from the other axes, and therefore reduces any possible interference. Coarse control of the tip position was achieved using mircropositioners, which offered a cost effective solution.

Previously, a number of methods to control the piezoelectric positioners, such as through digital cards or external amplifiers/servos, were used. These control methods required different software solutions. To simplify this, all piezoelectric po-

sitioners were controlled through an external amplifier/servo using analog channels. This reduced the amount of instrument specific code and also allowed piezoelectric positioners to be moved between instruments.

A number of techniques, such a SICM, SECCM, IC-SECM, utilize a feedback mechanism that is based on oscillating the probe and measuring the induced alternating current (AC) components. This is typically achieved using a software or hardware based lock-in amplifier. Based on experience with both configurations a hardware based lock-in amplifier was used within all instruments.

Finally, all instruments used a LabVIEW (National Instruments) based software interface to control, and measures signals from, the hardware through a FPGA card. LabVIEW was used to maintain continuity with previous EC-SPM instruments and because it is a simple programming language for inexperienced users. A FPGA card was used to allow fast data acquisition from multiple channels, and quick data averaging and probe position control.

Six new EC-SPM instruments were constructed. These EC-SPM instruments have a range of different capabilities, with three mounted on microscopes (a fluorescence, reflected light and confocal microscope). Four instruments used a sample scanning configuration, while the other instruments used a probe scanning configuration. Different piezoelectric positioners, with different travel distances, were used on each instrument. However, all piezoelectric positioners were controlled using external servos/amplifiers. A FPGA card was used to measure all electrochemical signals, and control the position of the probe. This allowed a common software solution to control and measure from the hardware.

5.3 Hardware

A typical EC-SPM instrument, with labelled components, is shown in Figure 5.1. The sample (2 in Figure 5.1) was mounted on a sample holder (3 in Figure 5.1)

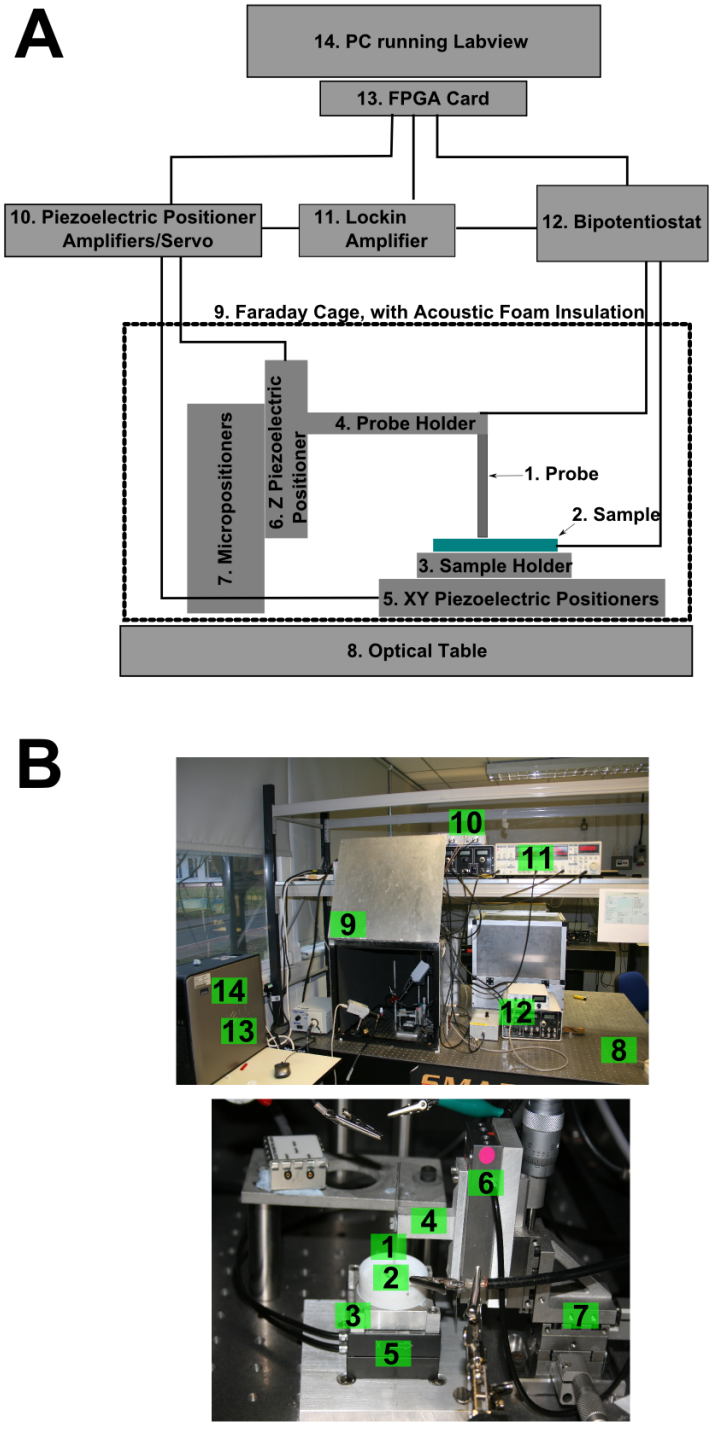

Figure 5.1: **A.** Schematic of a typical EC-SPM instrument. **B.** Photo of a typical EC-SPM instrument. The individual labelled components are discussed, in detail, in the main text.

that was in turn mounted on two (X and Y) piezoelectric positioners (typically P-622.1CD, Physik Instrumente, 5 in Figure 5.1) that allowed the lateral movement of the sample. Care was exercised with the mass and strain that the sample holder places on the XY piezoelectric positioners. The sample holder was frequently made from PTFE or other light weight materials. For the SECCM technique, a moat, which was filled with electrolyte solution to create a humidity cell, was also built into the sample holder. Piezoelectric positioners are delicate devices and were treated with extreme care especially when working with solutions.

The probe (1 in Figure 5.1) was mounted on a third (Z) piezoelectric positioner (typically P-753.31C, Physik Instrumente, 6 in Figure 5.1) that allowed movement normal to the sample surface. The probe was held in position by a holder, which was typically a solid bar with a 'v' shaped grove and PTFE screw to hold the probe in place (4 in Figure 5.1).

The peizoelectric positioners were controlled through amplifiers/servos (10 in Figure 5.1) by analog channels. Each amplifier/servo was calibrated to an individual piezoelectric positioner and a control signal (typically 0 V - 10 V) was used to control the position. Coarse control of the probe position was achieved using manual micropositioners (7 in Figure 5.1).

A custom bipotentiostat (or galvanostat) (12 in Figure 5.1), designed and built in house by Dr Alex Colburn, was used to measure electrochemical signals at the probe. This equipment was controlled through, and the electrochemical signals measured as, analog signals. This unified the method of control and allowed components to be switched between instruments. A number of techniques, such as IC-SECM and SECCM, use an oscillating probe and the oscillating signal was generated, and the resulting oscillating current signal measured, using an external lockin amplifier (SR830, Stanford Research Systems, 11 in Figure 5.1).

A FPGA card (7852R, National Instruments, 13 in Figure 5.1) mounted directly into the motherboard of the PC was used to collect all the data measured

by the bipotentiostat (or galvanostat) and control the position and potential of the probe. Eight analog channels (Substrate Current, Barrel Current, Barrel AC Magnitude, Barrel AC phase, X Position, Y Position, Z Position, Current3) were measured though the FPGA card and four analog channels (X Position, Y Position, Z Position and Voltage) generated at the card. The FPGA card allowed complex calculations, such as data filtering and probe position control logic, to be completed on the card and this is discussed in full within the software section below. A 32 bit PC running Windows XP and the latest version of LabVIEW (LabVIEW2011, National Instruments) was used (14 in Figure 5.1). A home built break out box, with BNC connectors, was used connect the input and output channels of the FPGA card to the various components of the instrument.

Electrical, acoustic and vibrational isolation are essential for high resolution current measurements and positional control. All instruments were mounted on vibration isolation tables (8 in Figure 5.1), within a Faraday cage (custom made) that also had acoustic foam to reduce acoustic vibrations (9 in Figure 5.1). Cameras, or alternatively a microscope, were used to aid positioning of the probe over a sample. Finally, it was necessary to align the system, so that the tip and sample were perpendicular to each other, before use.

5.4 Software

Instrument control, and data acquisition, was achieved using a LabVIEW interface through a FPGA card. This section describes the structure of the software. A list of the input and output variables for the main components is given in Sections 5.7.1, 5.7.2 and 5.7.3.

The use of a FPGA card enabled fast data acquisition and control of the probe position and potential through embedded instructions, however it also restricted the structure of the EC-SPM software. The software was designed in three layers, the

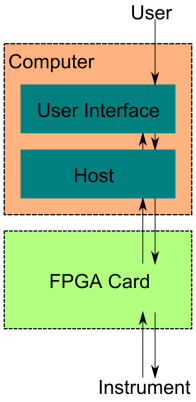

Figure 5.2: Schematic of software structure with the three components: the user interface, the host and the FPGA card.

user interface, the host and the FPGA card, as shown in Figure 5.2. The user interface and host were executed on the PC. A user defined a set of instructions using a user interface. The host translated the instructions and transferred them to the FPGA card, while also collecting data from the FPGA card and saving it to the hard drive of the PC. The FPGA card collects data and generates control signals, based on the instruction that have come from the user, to control the instrument.

The FPGA card required host running on the PC. By adding the third component, the user interface, the logic for communicating with the card was separated from the logic that interacted with the user. This allowed many different techniques to use one set of logic (the host and FPGA card) to control the instrument. This also allowed new probe movement schemes to be quickly generated.

A way-point scheme was used to encode the instructions on the FPGA card. A set of points (positions and potentials), and instructions on how to move between these points, was generated by the user. The FPGA card read the instructions and generated the signals to carry out these instructions. The user specified where and how to move the probe, but a single dedicated set of logic on the FPGA card was responsible for carrying out these instructions. This allowed many different probe movement protocols to be quickly and easily generated without the user having to

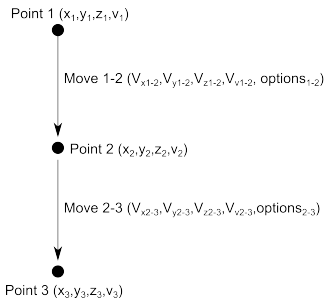

Figure 5.3: Schematic of the way-point scheme.

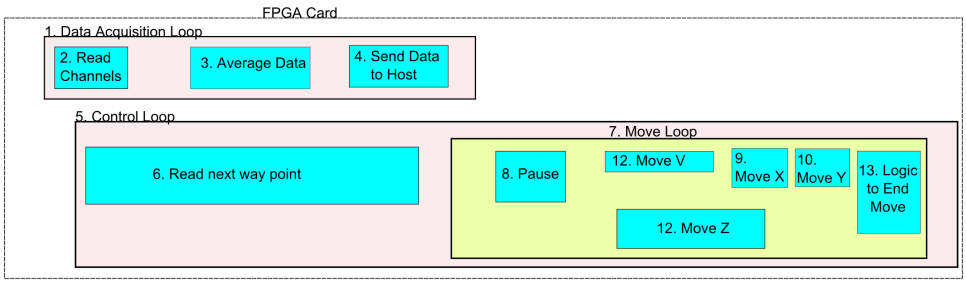

Figure 5.4: Schematic of structure of the FPGA card.

generate individual signals. A schematic of the way-point scheme is shown in Figure 5.3.

5.4.1 FPGA Card

The logic embedded on the FPGA card controlled how the data was collected, from the various components of the instrument, and the position and potential of the probe. Figure 5.4 shows a schematic of the structure of the card. The code on the FPGA card was separated into two parts that run in parallel, the data acquisition and the positional (and voltage) control. The data acquisition component was responsible for collecting data, averaging this data and then transferring the averaged data to the PC. The control code was responsible for reading the instructions, in the form of way-points, and computing the signals to control the hardware components based on these instructions.

Data Acquisition

The data acquisition code acquired a sample (from an analog channel), averaged a number of samples into a single data point and then transferred this to the PC. A loop was employed (1 in Figure 5.4) and every time interval (user-defined) a sample was taken from each (X Position, Y Position, Z Position, Current 1, Current 2, Current 3, AC Amplitude and AC Phase) analog channel (2 in Figure 5.4). The value was then stored in memory on the FPGA card (3 in Figure 5.4). The next time the loop ran, another sample was taken and added to the previous value. Once a number of samples (user-defined, but restricted to be a power of 2) had been taken, the accumulated value within memory was divided by the number of samples (which is a power of 2) creating a single data point. The data point was then transferred to the PC using a first-in first-out (FIFO) buffer (4 in Figure 5.4) and the memory value was set to zero ready for the next sample.

The values from the analog lines (samples) were measured as I16 variables (integers between -2^{15} and 2^{15}). A value of -2^{15} was equal to -10 V, and 2^{15} was equal to 10 V. These values depend on the type and accuracy of the particular FPGA card, in this case a 16 bit FPGA card with a range of $\pm$ 10 V used. Note, the accumulation variable must be large enough to store the sum of many measurements and therefore an I64 type variable was used which can store upto 2^{64-15} samples. Division on a FPGA card is a costly calculation and therefore resources were conserved by restricting the number of samples to a power of 2, which allowed a bit shifting division operation to be used.

A FIFO buffer is a communication routine that is available through LabVIEW for communicating between a PC and a FPGA card. This was used because the FPGA card and the PC can run at very different speeds. The FPGA card can generate data at a rate such that the PC cannot keep up when it is reading individual data points. However, if the data points are put into a buffer the PC can read a number of data points at once and keep up with the data being generated.

Instrument Control

The instrument control segment of the FPGA card took instructions from the user, in the form of way-points, and generated the output signals that control the instrument. The user specified a series of way-points (x,y,z,v) through which to move along with the speed (dx,dy,dz,dv) of the movement and additional options. The FPGA card took these points and generated the values for the output channels based on an internal clock.

For example, a cyclic voltammogram (CV) could be generated by specifying four points and three velocities. The four points would be (0,0,0,V1), (0,0,0,V2), (0,0,0,V3), and (0,0,0,V1), where V1 is the initial voltage, V2 is one end potential of the CV and V3 is the other end potential. The velocities would be (0,0,0,ScanRate), (0,0,0,-ScanRate) and (0,0,0,ScanRate), where ScanRate is the potential scan rate within the CV. Also the options specify that only the voltage changes.

Practically, the code read the position, the velocity and options (6 in Figure 5.4) from the host via a FIFO buffer. If no new position was available, the code waited until a new position was generated by the host. Once a new position, velocity and set of options were read, a loop (7 in Figure 5.4) was used to move the probe position (and potential) from the current position to the new position. The movement was based on an internal timer and the velocities. Each axis (X,Y,Z or V) calculated its position, and generated the out signal independently (9 - 12 in Figure 5.4). Once all four axes finished moving, the loop was terminated (13 in Figure 5.4) and the next movement was read from the FIFO buffer. Note that movement could be paused or stopped by the user at any time (8 in Figure 5.4).

All the position variables were specified in I16 units and time was measured in ticks (where one tick was 25 ns, although the FPGA card can be configured to run faster or slower). Therefore, the velocities on the FPGA card were specified in units of I16 per tick. These units were hidden from the end user as the host translates values specified by the user, which have units of μm, volts or amps, into

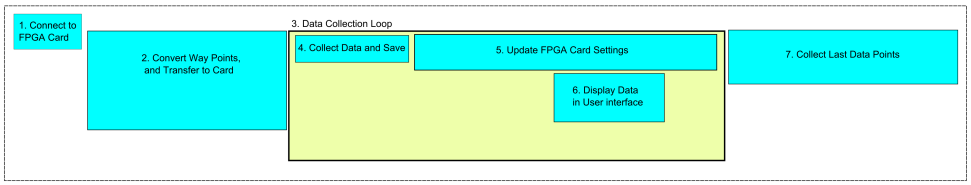

Figure 5.5: Schematic of the host

the units required for the card. Note that there is an additional scaling factor for the velocity units that depended on the absolute magnitude of the fastest velocity. This was implemented to allow both very slow or very fast movements.

In many situations the FPGA card was used to change the height of the probe (or sometimes the potential of the probe) based on a signal measured by the card. For instance in SECCM, the probe was moved laterally and the height of the probe was controlled by a simple proportional feedback loop running on the card to maintain a constant AC magnitude.

5.4.2 Host

The host was executed on the PC and was responsible for communicating with, and collecting data from, the FPGA card. The host code translated instructions from the user and relayed them to the FPGA card. Only one version of the host was run at any one time and therefore only one action could be performed by the user at any time.

On initialisation, the host connected to the running FGPA card or started the FGPA card running (1 of Figure 5.5). Once a connection was established the host translated instructions from the user into the appropriate units for the FPGA card (2 of Figure 5.5). The host then transferred these instructions to the FPGA card through a FIFO buffer (2 in Figure 5.5). The host collected data from the FPGA card using a loop (3 of Figure 5.5). The loop collected the data from the FIFO and then stored the data on the hard drive in a binary file (this file was over-

written with every new action that the user requests, 4 in Figure 5.5). The host could display the data that was collected within graphs that were visible in the user interface (6 in Figure 5.5). Once a set of instructions had been completed, or the user pressed stop, the host transferred the last data points from the FPGA card (7 in Figure 5.5). The format of all inputs for the host is specified in Section 5.7.2.

5.4.3 User Interface

Many different user interfaces can be, and have been, constructed. Each carried out a specific task, for example run a CV, run an approach curve or undertake a SECCM scan. Each interface gave the user a range of options through which the particular task could be customized.

Figure 5.6 shows the structure of the front and back panel of a typical user interface, for a CV. A user interface needs to accomplish 3 tasks: i) generate the set of way-points and options; ii) run the host; and iii) translate the saved data into a .txt file, and also create a .set file in which all the user options are saved.

The data collected was initially saved, by the host, in a binary format but this was then translated into an ascii text file. This file format allowed a range of programs to be used to analyse and plot the data. Note that for long scans, or when data was being collected at high rates, the .txt file becomes large and it was easier to work directly with the binary version. The format of the .txt data file is specified in Section 5.7.3.

5.4.4 Data Processing

Data processing was not built into the LabVIEW EC-SPM software and therefore must be accomplished after a scan is finished (post processing) in an appropriate software package, such as Matlab. Processing, and plotting, of the data was separated from the generation and acquisition because LabVIEW did not provide usable data manipulation and plotting routines, and to minimise the use of EC-SPM in-

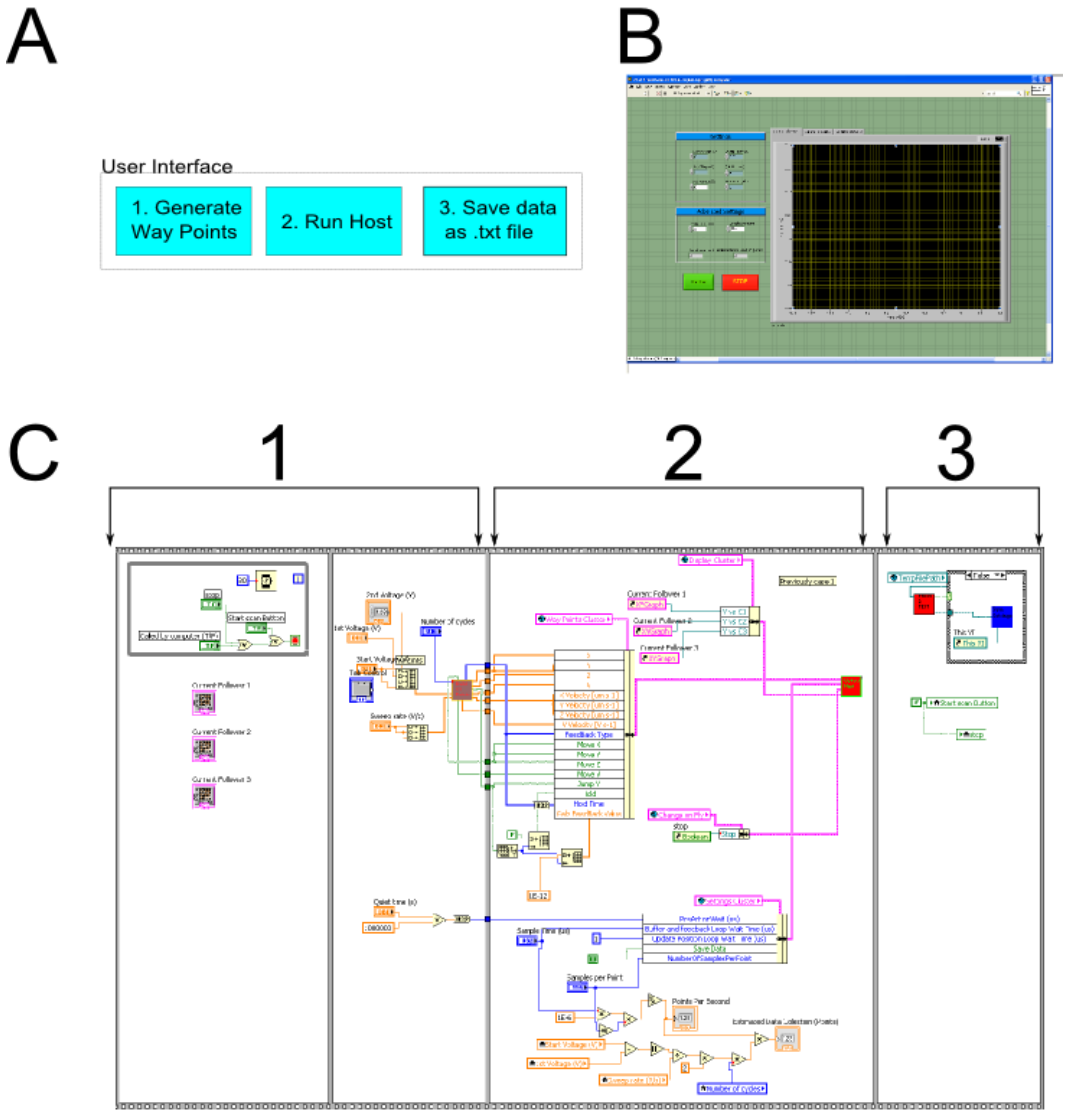

Figure 5.6: **A.** General structure of a user interface. Three tasks need to be completed by the user interface. 1. The set of instructions must be generated. 2. The FPGA card, through the host, must be run to carry out these instructions. 3. The data generated must be saved. **B.** Example of a front panel for the CV program. **C.** Example of the back panel (code) for the CV program, with the three tasks labelled.

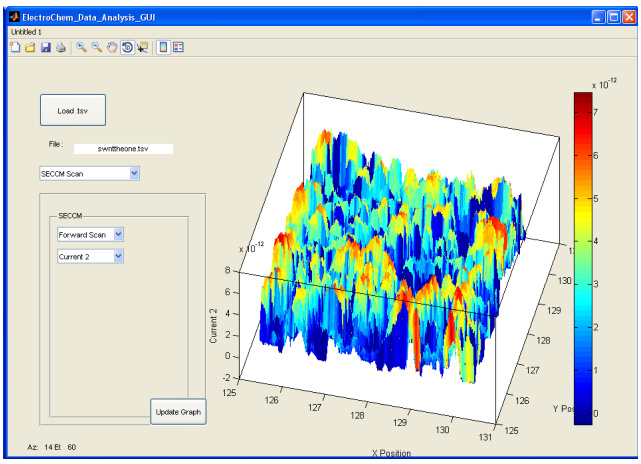

Figure 5.7: Screen capture of Matlab data viewer.

struments. A data inspection program, with a graphic user interface, was written in Matlab to allow data to be inspected quickly and easily. This program read the .txt files and displays a variety of graphs (such as time series, 2D or 3D graphs) based on the electrochemical data. Figure 5.7 shows a screen capture of the Matlab data viewer program.

5.4.5 Unified Code Base

All instruments used the same software and therefore were capable (allowing for hardware differences) of running the same techniques. To maintain code consistency across instruments a version control server (subversion), with the authoritative version of the code, was used. This allowed code changes to be tracked and new changes to be quickly and easily, with one click of a button, moved between instruments.

5.5 Evaluation

There are currently six EC-SPM instruments which are used by ca. 13 members of the Warwick Electrochemistry and Interfaces group and have to date generated 7 published papers,[32–38] with more in preparation. The new EC-SPM instruments have been used for a range of techniques (SECM, SECCM, SICM and SICM-SECM).

A number of new techniques that were not identified prior to construction have been used. Nanoscale SECCM, SICM and SICM-SECM probes are now used routinely. Also, the common software interface allowed new probe movement schemes to be quickly generated and shared between instruments. New probe movements schemes, new functionality such as synchronizing an external light source the probe movement, and bug fixes are regularly applied to all instruments.

5.6 Acknowledgements

The construction of the EC-SPM instruments was achieved with contributions from: Michael A. O'Connell, Neil Ebejer, Stanley C. S. Lai, Michael E. Snowden, Massimo Peruffo, Aleix G. Güell, Barak Aaronson, Marc Baghdadi, Sophie Kinnear, Alexander W. Colburn, Julie Macpherson and Patrick R. Unwin

5.7 Input and Output Variables

5.7.1 FPGA API

The input and output variables for the code executed on the FPGA card (version 97, 2 November 2012) are defined in Tables 5.1 and 5.2. Note that all local variables on the FPGA card can be monitored using the host.

The Host_to_FPGA_FIFO buffer defined the instructions read by the FPGA card. Each movement was defined by four I64 values. The first defined the velocities (X Velocity, Y Velocity, Z Velocity, Voltage Velocity), the second and third defined the options (line feedback type, moveX, moveY, moveZ, moveV, jumpV, hold position, holdtimer and Galvanostatic current set point) and the four defined the new position (X position, Y position, Z position, V position).

The FPGA_To_Host_FIFO buffer passed data back to the PC. For each time point four I64 values were used to transfer the data. The first value contained the X (AI0, I16), Y (AI1, I16), Z (AI2, I16) and Current1 (AI3, I16) values. The second

I64 contained the X (AO0, I16), Y (AO1, I16), Z (AO2, I16) and Voltage (AO3, I16) values. The third the Current 2 (AI4, I16), Line feedback type (I16), Sample per data point (I16) and Line number (I16) values, and the fourth the AC Amplitude (AI5, I16), AC Phase (AI7, I16), Current 3 (AI6, I16) and Galvanostatic current set point (I16) values.

Table 5.1: FGPA input variables

Variable	Description
Host_to_FPGA_FIFO	Buffer for defining way-points, velocities and options.
External Stop	Command to stop the card
DistanceToBulk	Distance to move when retracting the bulk
Update Position Loop Wait Time (ticks)	Update rate for positional control
External Pause	Command to pause the card
Current SetPoint For Voltage Feedback	Feedback value for galvanostatic mode
P for Voltage	Gain for galvanostatic mode
VoltageFeedback_useuserDefined?	Command to switch how galvanostatic setpoint is defined
dV for Voltage Feedback	maximum V movement per update for galvanostatic mode
V on Fly	Voltage Value
ExpandVelScaller X	Velocity scaler for the movement in the X direction
ExpandVelScaller Y	Velocity scaler for the movement in the Y direction
ExpandVelScaller Z	Velocity scaler for the movement in the Z direction
ExpandVelScaller V	Velocity scaler for the movement of the potential
Feedback Type	Control to change what type of feedback signal is used
Feedback_Threshold	Feedback Value
GreaterThan	Control to change how the feedback signal is compared to the measured value
Upper limit of dZ	Maximum movement in the Z direction for the feedback updates
EndCurrentLine	Control for the user to end the current line
Buffer Loop Wait Time (tICKS)	Update rate for data acquisition
2^(-n)	Scaler for number of data acquisition points to average over

Table 5.2: FGPA output variables

Variable	Description
FPGA_To_Host_FIFO	Buffer of collected data.
Internal Pause	Indicator that the card has paused.

5.7.2 Host API

The input variables used by the host code (version 97, 2 November 2012) are defined in Tables 5.3, 5.4, 5.5, 5.6 and 5.7.

5.7.3 General Settings

The data collected were saved as an ascii text file. The data was saved as 14 rows, and N columns, where N is the number of samples measured by the card. The time

Table 5.3: Host input variables

Variable	Description
Way Points Cluster	Defines instructions (positions, velocities and options) for the FPGA card.
Settings Cluster	Defines settings for the host and FPGA card.
Change on Fly	Defines extra setting that may be changed at any time.
Display Cluster	Defines the graphs in which data may be displayed in real time

Table 5.4: Host Way Points Cluster

Variable	Description	Range
X	1D array of X positions	± X piezo range in μm
Y	1D array of Y positions	± Y piezo range in μm
Z	1D array of Z positions	± Z piezo range in μm
V	1D array of Potentials	± 10 V
Xvel	1D array of X velocities	$\pm\infty$ in μm s^{-1}
Yvel	1D array of Y velocities	$\pm\infty$ in μm s^{-1}
Zvel	1D array of Z velocities	$\pm\infty$ in μm s^{-1}
Vvel	1D array of potential velocities	$\pm\infty$ in V s^{-1}
feedback type	1D array of probe movement types	0 -13
hold timer	1D array of hold timer value	0 - ∞ s
Galv Feedback Value	1D array of set points for galvanostic feedback	0 - ∞ A
moveX	1D array controlling the use of the X axis	boolean
moveY	1D array controlling the use of the Y axis	boolean
moveZ	1D array controlling the use of the Z axis	boolean
moveV	1D array controlling the use of the V axis	boolean
Hold	1D array controlling if to hold the probe at the end of the current movement	boolean
JumpV	1D array controlling if to jump, or move linearly, the potential	boolean

Table 5.5: Settings Cluster

Variable	Description
Buffer and feedback loop wait time (us)	Time between data acquisitions (μs)
Update position loop wait time (us)	Time between probe position updates (μs)
Number of Sample Per Point	Number of samples to average over (restricted to 2^n)
Save Data	Option to save the collected data on the PC
Change V on fly	Option on how to change V
DistanceToBulk / um	Distance to move when retracting the bulk (μm)
StopCond_GreaterThan	Control of how feedback signal is compared to measured value
Use WayPoint Galv SetPoint	Command to switch how galvanostatic setpoint is defined
FilePath2	NOT USED
BulkAtEndOfLine	NOT USED
DistanceToBulk	NOT USED
ReverseScanDistance	NOT USED
XMajor	NOT USED
preActionWaite(us)	NOT USED

between each sample was (Number of Sample Per Point+1)*(Buffer and feedback loop wait time (us)), where these variables are defined in Table 5.5. The 14 rows are: X, Y, Z, current1, dX, dY, dZ, potential, current2, feedback type, line number, lockin Amplitude, lockin phase and current 3. A general setting file defines the global settings, and the variables are shown in Table 5.8.

Table 5.6: Change on Fly

Variable	Description
Stop	Stop the current set of instruction
pause	Pause the current movement
EndCurrentLine	End the current instruction and start the next one
Threshold	Setpoint for probe position feedback loop (A)
Threshold type	Defines what type of threshold
P	multiplier in P feedback loop for probe height
Upper limmit of dZ	Maximum movement per update step in probe height feedback (U16)
P Voltage	multiplier in P feedback loop for potential
Upper limit Of dZ votlage	Maximum movement per update step in probe potential feedback (U16)
Threshold Voltage	Setpoint for probe potential feedback loop (A)
on Fly Voltage	Voltage value (V)

Table 5.7: Display Cluster

Variable	Description
X	Indicator of X position
Y	Indicator of Y position
Z	Indicator of Z position
V	Indicator of V position
Amp	Indicator of amplitude
Phase	Indicator of phase
TvsZ	Graph of time vs z position
TvsZ	Graph of time vs current 1
TvsZ	Graph of time vs current 2
TvsZ	Graph of time vs current 3
TvsZ	Graph of z position over time
VvsC1	Graph of potential vs current 1
VvsC2	Graph of potential vs current 2
VvsC3	Graph of potential vs current 3
ZvsC1	Graph of z position vs current 1
ZvsC2	Graph of z position vs current 2
ZvsC3	Graph of z position vs current 3
X/Y/Z forward	2D (X and Y) graph of Z position from forward line scans
X/Y/C1 forward	2D (X and Y) graph of current 1 from forward line scans
X/Y/C2 forward	2D (X and Y) graph of current 2 from forward line scans
X/Y/C3 forward	2D (X and Y) graph of current 3 from forward line scans
X/Y/Z reverse	2D (X and Y) graph of Z position from reverse line scans
X/Y/C1 reverse	2D (X and Y) graph of current 1 from reverse line scans
X/Y/C2 reverse	2D (X and Y) graph of current 2 from reverse line scans
X/Y/C3 reverse	2D (X and Y) graph of current 3 from reverse line scans
Hop X,Y,Z	2D graph(X and Y) of Z position from a hopping scheme
Hop X,Y,C1	2D graph(X and Y) of current 1 from a hopping scheme
Hop X,Y,C2	2D graph(X and Y) of current 2 from a hopping scheme
Hop X,Y,C3	2D graph(X and Y) of curretn 3 from a hopping scheme
numberoflines	Input for formatting line scan graph defining the number of lines
umperpixel	Input for formatting line scan graph defining the resolution to display data
umperline	Input for formatting line scanning defining distance between lines
Xcenter	Input for defining center of scan area
hoppingdistance	Input for define distance between approaches for the hopping graphs
Xwidth	Width of the line scan graph
Ywidth	Hieght of the line scan graph

Table 5.8: Settings

Variable	Description
dtms file out	Defines the location to save the binary data file
FOPGA speed	Indicator of the speed at which the FPGA card runs (Hz)
Host Path	Path of the host program
HostToFPGAFIFO Length	Number of elements in the buffer
FIFOU64PerWayPoint	Number of data points needed to specify one way-point
FIFOU64PerSamlpe	Number of data points needed to pass a sample back from the card
Z Piezo maximum range	Range of Z piezoelectric positioner (μm)
X Piezo maximum range	Range of X piezoelectric positioner (μm)
Y Piezo maximum range	Range of Y piezoelectric positioner (μm)
Current Follower 1	Current follower 1 sensitivity (A/V)
Current follower 2	Current follower 2 sensitivity (A/V)
current follower 3	Current follower 3 sensitivity (A/V)
lockin sensitivity	External lockin sensitivity (V)
Expand	Expand scaler on external lockin amplifier
Percentage offset	Offset on external lockin amplifier
Current X	Indicator of current X position (μm)
Current Y	Indicator of current Y position (μm)
Current Z	Indicator of current Z position (μm)
Current V	Indicator of current potential (V)
FPGA running	Indicator that the host is connected to the FPGA card
FPGA Reference	Indicator of reference number to the FPGA card
Channel Names	List of channel names used to save data

References

[1] Bard, A. J.; Fan, F.-r. F.; Kwak, J.; Lev, O. *Anal. Chem.* **1989**, *61*, 132–138.

[2] Kwak, J.; Bard, A. J. *Anal. Chem.* **1989**, *61*, 1221–1227.

[3] Kwak, J.; Bard, A. J. *Anal. Chem.* **1989**, *61*, 1794–1799.

[4] Amemiya, S.; Bard, A. J.; Fan, F.-R. F.; Mirkin, M. V.; Unwin, P. R. *Ann. Rev. Anal. Chem.* **2008**, *1*, 95–131.

[5] Bard, A. J.; Mirkin, M. V. *Scanning Electrochemical Microscopy*; Marcel Dekker Inc: New York, 2001.

[6] Mirkin, M. V.; Nogala, W.; Velmurugan, J.; Wang, Y. *Phys. Chem. Chem. Phys.* **2011**, *13*, 21196–21212.

[7] Sun, P.; Laforge, F. O.; Mirkin, M. V. *Phys. Chem. Chem. Phys.* **2007**, *9*, 802–823.

[8] Hansma, P. K.; Drake, B.; Marti, O.; Gould, S. A.; Prater, C. B. *Science* **1989**, *243*, 641–643.

[9] Chen, C.-c.; Zhou, Y.; Baker, L. A. *Ann. Rev. Anal. Chem.* **2012**, *5*, 207–228.

[10] Eckhard, K.; Schuhmann, W. *Analyst* **2008**, *133*, 1486–1497.

[11] Ludwig, M.; Kranz, C.; Schuhmann, W.; Gaub, H. E. *Revi. Sci. Instru.* **1995**, *66*, 2857–2860.

[12] Karrai, K.; Grober, R. D. *Appl. Phys. Lett.* **1995**, *66*, 1842–1844.

[13] McKelvey, K.; Edwards, M. A.; Unwin, P. R. *Anal. Chem.* **2010**, *82*, 6334–6337.

[14] Takahashi, Y.; Shevchuk, A. I.; Novak, P.; Murakami, Y.; Shiku, H.; Korchev, Y. E.; Matsue, T. *J. Am. Chem. Soc.* **2010**, *132*, 10118–10126.

[15] Comstock, D. J.; Elam, J. W.; Pellin, M. J.; Hersam, M. C. *Anal. Chem.* **2010**, *82*, 1270–1276.

[16] Morris, C. A.; Chen, C.-C.; Baker, L. A. *Analyst* **2012**, *137*, 2933–2938.

[17] Takahashi, Y.; Miyamoto, T.; Shiku, H.; Ino, K.; Yasukawa, T.; Asano, R.; Kumagai, I.; Matsue, T. *Phys. Chem. Chem. Phys.* **2011**, *13*, 16569–16573.

[18] Macpherson, J. V.; Unwin, P. R. *Anal. Chem.* **2000**, *72*, 276–285.

[19] Ebejer, N.; Schnippering, M.; Colburn, A. W.; Edwards, M. A.; Unwin, P. R. *Anal. Chem.* **2010**, *82*, 9141–9145.

[20] Williams, C. G.; Edwards, M. A.; Colley, A. L.; Macpherson, J. V.; Unwin, P. R. *Anal. Chem.* **2009**, *81*, 2486–2495.

[21] Takahashi, Y.; Shevchuk, A. I.; Novak, P.; Zhang, Y.; Ebejer, N.; Macpherson, J. V.; Unwin, P. R.; Pollard, A. J.; Roy, D. D.; Clifford, C. A.; Shiku, H.; Matsue, T.; Klenerman, D.; Korchev, Y. E. *Angew. Chem. Int. Edit.* **2011**, *50*, 9638–9642.

[22] Oyamatsu, D.; Kanaya, N.; Shiku, H.; Nishizawa, M.; Matsue, T. *Sensors Actuat. B-Chem.* **2003**, *91*, 199–204.

[23] Nebel, M.; Eckhard, K.; Erichsen, T.; Schulte, A.; Schuhmann, W. *Anal. Chem.* **2010**, *82*, 7842–7848.

[24] Sensolytics SECM. 2012; www.sensolytics.com/en/products2/secm.

[25] Kim, J.; Shen, M.; Nioradze, N.; Amemiya, S. *Anal. Chem.* **2012**, *84*, 3489–3492.

[26] Takahashi, Y.; Shiku, H.; Murata, T.; Yasukawa, T.; Matsue, T. *Anal. Chem.* **2009**, *81*, 9674–9681.

[27] Zhukov, A.; Richards, O.; Ostanin, V.; Korchev, Y.; Klenerman, D. *Ultramicroscopy* **2012**, *121*, 1–7.

[28] Takahashi, Y.; Murakami, Y.; Nagamine, K.; Shiku, H.; Aoyagi, S.; Yasukawa, T.; Kanzaki, M.; Matsue, T. *Phys. Chem. Chem. Phys.* **2010**, *12*, 10012–10017.

[29] Macpherson, J. V.; Unwin, P. R. *Anal. Chem.* **2001**, *73*, 550–557.

[30] Novak, P.; Li, C.; Shevchuk, A. I.; Stepanyan, R.; Caldwell, M.; Hughes, S.; Smart, T. G.; Gorelik, J.; Ostanin, V. P.; Lab, M. J.; Moss, G. W. J.; Frolenkov, G. I.; Klenerman, D.; Korchev, Y. E. *Nat. Methods* **2009**, *6*, 279–281.

[31] Happel, P.; Dietzel, I. D. *J. Nanobiotech.* **2009**, *7*, 7.

[32] Lai, S. C. S.; Patel, A. N.; McKelvey, K.; Unwin, P. R. *Angew. Chem. Int. Edit.* **2012**, *51*, 5405–5408.

[33] Güell, A. G.; Ebejer, N.; Snowden, M. E.; Macpherson, J. V.; Unwin, P. R. *J. Am. Chem. Soc.* **2012**, *134*, 7258–7261.

[34] Snowden, M. E.; Güell, A. G.; Lai, S. C. S.; McKelvey, K.; Ebejer, N.; O'Connell, M. A.; Colburn, A. W.; Unwin, P. R. *Anal. Chem.* **2012**, *84*, 2483–2491.

[35] Güell, A. G.; Ebejer, N.; Snowden, M. E.; McKelvey, K.; Macpherson, J. V.; Unwin, P. R. *Proc. Natl. Acad. Sci. USA* **2012**, *109*, 11487–11492.

[36] Patel, A. N.; Collignon, M. G.; O'Connell, M. A.; Hung, W. O. Y.; McKelvey, K.; Macpherson, J. V.; Unwin, P. R. *J. Am. Chem. Soc.* **2012**, *134*, 20117–20130.

[37] Kleijn, S. E. F.; Lai, S. C. S.; Miller, T. S.; Yanson, A. I.; Koper, M. T. M.; Unwin, P. R. *J. Am. Chem. Soc.* **2012**, 18558–18561.

[38] Patel, A. N.; McKelvey, K.; Unwin, P. R. *J. Am. Chem. Soc.* **2012**, *134*, 20246–20249.

Chapter 6

Fabrication, Characterisation and Applications of Dual Carbon Electrodes

SECM can be productively expanded by using dual electrode probes which allow two independent electrochemical signals to be measured simultaneously. A quick and simple method to construct dual carbon electrodes was developed which involved the pyrolytic deposition of carbon into the barrels of a dual barrelled pipet. The dual carbon electrodes were used to investigate the oxidation of ascorbic acid and also the interaction of an artificial electron acceptor with the photosynthetic electron transport pathway.

This chapter consists of the communication, currently in preparation, detailing the preparation, characterisation and initial experiments with the dual carbon electrodes. Binoy Paulose Nadappuram and myself were jointly responsible for conducting the experiments, while I undertook the FEM simulations and wrote the majority of the communication. Yasufumi Takahashi provided probe construction advice.

Fabrication, Characterisation and Applications of Dual Carbon Electrodes

Kim McKelvey, Binoy Paulose Nadappuram, Yasufumi Takahashi, Tomokazu Matsue, Yuri E. Korchev, Colin Robinson, Patrick R. Unwin

in preparation.

6.1 Abstract

Dual carbon electrodes (DCEs) are quickly, easily and cheaply fabricated by pulling a quartz theta pipet to a sharp point and filling the two barrels with pyrolytic carbon. This produces probes, of between 100 nm and 50 μm in size, with two planer semi-elliptical electrodes separated by a small septum. When DCEs are operated in generation/collection mode, in which an active species is electrogenerated at one electrode and collected at the other electrode, the small separation between the electrodes leads to collection efficiencies, the ratio of species collected to generated, of up to 30 %. Nanoscale probes are difficult to characterize and use for quantitative measurements, therefore a 3 dimensional finite element method (FEM) simulation was used to estimate the apparent geometry of nanoscale DCEs from in-situ current measurements. Firstly, nanoscale DCEs was used to investigate the oxidation of ascorbic acid by electrogenerated ferrocenylmethyl trimethylammonium^{2+} (FcTMA^{2+}), and the FEM simulation was used to determine the apparent probe geometry, and then assess the apparent homogeneous rate constant, k, for the oxidation of ascorbic

acid by $FcTMA^{2+}$. This highlighted the challenges of using nanoscale probes for quantitative analysis, and in particular the difficulty in using FEM models to calculate the nanoscale probe geometry based on in-situ current measurements. Probes, both nanoscale and micronscale, were then employed in a scanning electrochemical microscopy (SECM) configuration, and approaches curves to insulating and conducting surfaces conducted. The interaction of $FcTMA^{2+}$ with the photosynthetic light dependent electron transport pathway that is embedded within the thylakoid membranes of higher plants was then investigated. A micron scale probe was placed precisely over a sparse monolayer of isolated thylakoid membranes and changes in $FcTMA^{+}$ and $FcTMA^{2+}$ concentration were measured as the sample was illuminated. To our knowledge this is the first report of the use of $FcTMA^{2+}$ as an artificial electron acceptor within photosynthesis. Finally, in generation/collection mode, using the $FcTMA^{+/2+}$ couple, a 2 dimensional image of a single thylakoid membrane was constructed by scanning a DCE, at a constant height, over the surface.

6.2 Introduction

Ultramicroelectrodes offer high mass transport rates, low ohmic (IR) drop effects, low double layer charging,[1–3] and as such are optimized for measuring the kinetics of fast electron transfer reactions. Moreover, when used as probes in a scanning electrochemical microscopy (SECM) configuration, they allow high spatial resolution interrogation of surfaces and interfaces. As an imaging tool, SECM has been widely used in studying the structure and process on the nanoscale, especially in electrocatalysis to detect and image regions with different catalytic activities,[4–6] and in biological systems for imaging living cells,[7–10] monitoring respiration and other cellular functions,[11–13] investigating biological redox systems[14,15] and the transport of molecules across biological membranes.[16–18] SECM has also been re-

ported for probing electron transfer kinetics at solid/liquid interfaces,[19,20] lateral mass/charge transfer across various interfaces[21−23] and used to fabricate nanostructures on surfaces.[24−26]

However, SECM can be productively extended to increasingly complex and challenging systems by developing dual electrode probes. This allows two redox-active species to be detected concurrently or permits a single redox-active species to be generated at one electrode and collected at the other electrode.[27,28]

Dual electrode systems, consisting of two independently controlled electrodes positioned close together, are widely used to study the kinetics of redox reactions.[29,30] Usually, but not exclusively,[31] such devices operate in an amperometric/voltametric mode where each electrode is held at a potential to oxidize or reduce a target species of interest, and the current measured at each electrode relates to the flux of that active species arriving at the electrode. In generation/collection mode, one electrode generates the species of interest (oxidizes or reduces the analyte (A) to produce an active species (S1)) that is then collected at the other electrode (via oxidation or reduction to produce the starting material back or another species (S2)):

$$\text{Electrode1} : A \pm e^- \rightleftharpoons S1$$

$$\text{Electrode2} : S1 \pm e^- \rightleftharpoons S2$$

The quantity, or flux, of active species generated and collected depends on the geometry of the dual electrode system and the mass transport between the electrodes. Generation/collection mode is often characterized by the collection efficiency, N, which is defined as the ratio of the current measured at the collector electrode to that measured at the generator electrode, usually under steady state conditions. Among a wide arrange of possible systems,[32] SECM tip generation substrate collection mode for analogous thin layer cell geometries offers the highest collection efficiency (essentially 100 %).

Interestingly, the active species can also interact with another species (B) present in solution; and this interaction can be observed by changes in the generation and collection currents:

$$\text{Solution} : S1 + B \rightleftharpoons S2 + C$$

Dual electrode systems that are constructed in a probe configuration, such as ring-disk,[33,34] dual-ring[35] and dual-disk[36–39] electrodes, allow the investigation of spatial heterogeneities of surfaces and interfaces, and thus combine the advantages of both systems. Probe-based dual electrode systems have been constructed from both single and dual (theta) barrel pipets by either sealing metallic wires into the probe or depositing carbon or metal electrodes within or on the barrels.[36,40] However, collection efficiencies for the majority of these systems have been low because the inter-electrode distance has often been large with respect to the electrode size, allowing species to escape before reaching the collector electrode. A range of electrode sizes from 50 μm[36] to nanometers[38] have been reported but the wider adoption of these systems has been limited due to difficulties in fabricating and characterizing the probes, which in turn introduces difficulties in the quantitative analysis of results.

Herein, we present a quick and simple method for the fabrication of a probe based dual-electrode system comprising of dual carbon electrodes (DCEs). This method allows the fabrication of a wide range of DCE sizes (between 100 nm to 50 μm) with a high success rate. DCEs are prepared from a laser pulled theta quartz pipet by in-situ carbon filling by pyrolytic decomposition of butane. This is a development of a recent method reported to make scanning ion conductance-scanning electrochemical microscopy (SICM-SECM) probes.[40] Pyrolytic deposition of carbon to form electrodes is a popular method and has been used to form a number of different SECM probes.[35,41–43] Nanoscale DCEs are challenging to char-

acterize and extract accurate geometrical parameters. Therefore, we developed a FEM model that allowed the effective geometry of individual nanoscale probes to be determined from current measurements. Firstly, we measure indirectly the oxidation of L-ascorbic acid (vitamin C) by $FcTMA^{2+}$ using a nanoscale DCE, and then use the FEM model to calculate the probe geometry and then the approximate kinetic rate constant for this oxidation. To demonstrate the versatility of these probes, approach curves, to insulating (inert) and conductive (active) surfaces, were recorded in generation/collection mode using intermittent contact-SECM (IC-SECM), which provides a current independent measure of the tip-substrate distance.[44–47] Thirdly, a DCE was positioned close to a monolayer of thylakoid membranes, and the reduction of $FcTMA^{2+}$, a previously unreported artificial electron acceptor, by the light driven components of photosynthesis was observed. Finally, a DCE was positioned precisely above a single thylakoid membrane, and 2 dimensional images were constructed, from both the generation and collection currents, by scanning the probe laterally over the sample at a constant height.

6.3 Experimental

6.3.1 Materials and reagents.

Solutions containing 1 mM ferrocenylmethyl trimethylammonium ($FcTMA^+$) hexafluorophosphate (obtained from the metathesis of ferrocenylmethyltrimethylammonium iodide and silver hexafluorophosphate (Strem Chemicals)),[48] or 1 mM L-ascorbic acid (Sigma Aldrich) with 1 mM $FcTMA^+$, in phosphate buffered saline (Sigma-Aldrich) was used for the ascorbic acid redox titration experiments. 1 mM $FcTMA^+$ in Milli-Q water (Millipore Corp., resistivity ca. 18.2 MΩ at 25 °C) with 0.1 M potassium chloride (Sigma-Aldrich, AR grade) as supporting electrolyte was used for IC-SECM approach curves measurements. 1 mM $FcTMA^+$ in aqueous HM buffer (10 mM HEPES (Sigma-Aldrich), 5 mM $MgCl_2$ (Sigma-Aldrich) and KOH

(Sigma-Aldrich) to adjust the pH to 8.0) was used for the thylakoid membrane measurements. Thylakoid preparation used aqueous HS buffer (50 mM HEPES, 0.33 M Sorbitol (Sigma-Aldrich) and KOH to adjust the pH to 8.0), 5×HS buffer (250 mM HEPES, 1.65 M Sorbitol, KOH to adjust pH to 8.0) and Percoll pads (2 ml of 5×HS, 3.5 ml Percoll and 4.5 ml H_2O). In addition, Poly-L-lysine (Sigma-Aldrich) was used to immobilize thylakoid membranes on a substrate. 3-(3,4-dichlorophenyl)-1,1-dimenthylurea (DCMU) was used to inhibit linear electron flow within immobilized thylakoid membranes. All the solutions containing redox-active species were prepared freshly on the day of use.

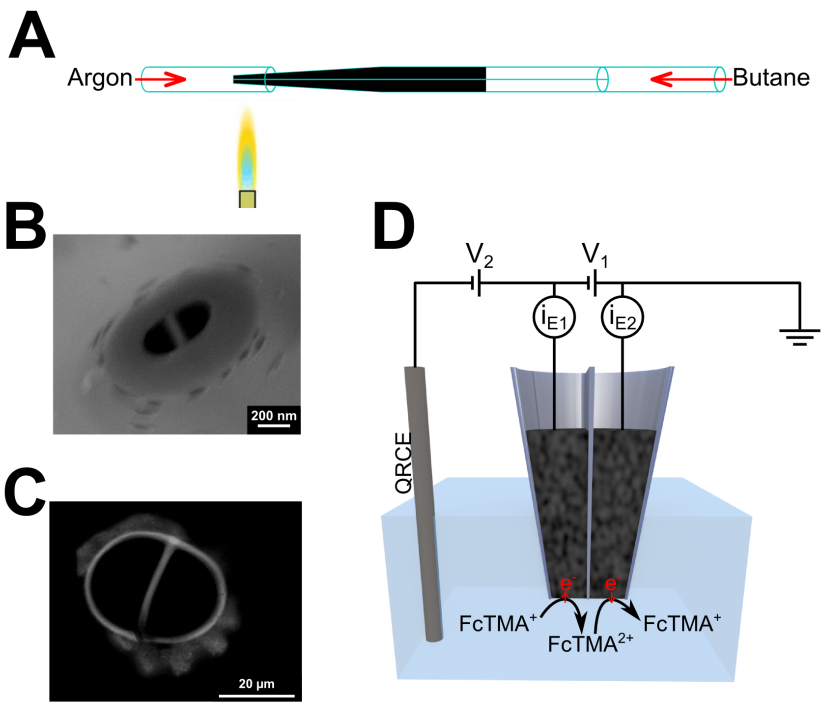

Figure 6.1: **A.** Schematic of the carbon deposition step of dual electrode fabrication, in which butane is passed through the pulled theta pipet and pyrolyzed using a hand held butane torch under an argon atmosphere. **B.** SEM of a typical nanoscale DCE. **C.** Optical image of micron scale DCE. **D.** Schematic of dual electrode configuration, with two working electrodes in the barrel of the probe, and a Ag/AgCl QRCE in solution. The current is measured at each working electrode (i_{E1} and i_{E2}), while the potential of the working electrodes, with respect to the QRCE, is controlled by V_1 and V_2. In generation/collection mode $FcTMA^+$ is oxidized at one electrode and $FcTMA^{2+}$ is reduced at the other electrode.

6.3.2 Electrode fabrication.

DCEs were fabricated based on the method described by Takahashi et al ,[40] with some modifications. Briefly, quartz theta pipets (O.D. 1.2 mm, I.D. 0.9 mm, Intracell) were pulled in a laser puller (P-2000, Sutter Instruments) to a sharp point. Butane was passed through the pulled pipet, via tubing, under an argon atmosphere. The tip of the probe was heated with a butane torch for 35 s, to pyrolytically deposit carbon from the butane, as illustrated in Figure 6.1 A. An electrical contact was established by inserting a copper wire through the top end of the pipet barrel to make contact with the carbon layer. Field-emission scanning electron micrograph (SEM) (Supra 55-VP, Zeiss) of a typical nanoscale DCE is shown in Figure 6.1 B, and an optical image of a larger DCE is shown in Figure 6.1 C. A range of electrode sizes, between 100 nm and 5 μm, were easily constructed by changing the laser pulling parameters during fabrication, while the larger DCEs were constructed by polishing smaller DCEs on diamond lapping disks (Buehler).

6.3.3 Electrochemical measurements.

A three electrode configuration was used, with two working electrodes (the two electrodes of the probe) and a single Ag/AgCl quasi reference/counter electrode (QRCE) in the bulk of the solution, as illustrated in Figure 6.1 D. In generation/collection mode the potential of one electrode was set to 0.5 V with respect to the QRCE for the diffusion limited oxidation of $FcTMA^{+}$, and the other electrode was at 0 V with respect to the QRCE for the diffusion limited reduction of $FcTMA^{2+}$, and this was achieved in our electrochemical configuration by setting V_1 = 0.5 V and V_2 = -0.5 V. The current induced at each working electrode was measured using a custom-built high sensitivity bipotentiostat.

Two SECM instruments were used, and are based on a previously described configurations.[44] Briefly, for the oxidation of L-ascorbic acid and the IC-SECM approach curve measurements a DCE was mounted on a bender piezoelectric positioner

(P-871.112, Physik Instrumente), which was in turn mounted on a 3 axis piezoelectric positioner (611.3S Nanocube, Physik Instrumente). The bender piezoelectric positioner was used to oscillate the probe normal to the surface; and also measure the oscillation amplitude of the probe, through the inbuilt strain gauge sensor for the approach curves that used IC-SECM mode.[44] For the thylakoid membrane measurements a DCE was mounted directly on a 3 axis piezoelectric positioner (611.3S Nanocube, Physik Instrumente). This was situated on a confocal/fluorescence microscope (TCS SP5 MP, Lieca). Within both configurations the piezoelectric positioners were mounted on micropositioners (Newport Corp.) inside a Faraday cage with vibration isolation (granite slab or an optical table). The piezoelectric positioners were controlled and the currents recorded through either a DAQ card (E-671, National Instruments) or a FPGA card (PCIe-7852R, National Instruments), which was, in turn, controlled using custom code from a PC running LabVIEW 2010 or LabVIEW 2011 (National Instruments).

6.3.4 Thylakoid membrane sample preparation.

Thylakoid membranes were prepared from the leaves of 8 to 9 day old peas (*Pisum sativum*, var. Kelvedon Wonder) using a mechanical disruption method.[49] Firstly, chloroplasts were prepared by homogenizing pea leaves using a Polytron blender (Kinematica GmbH) in HS buffer, this solution was then filtered through Microcloth (Calbiochem) and then centrifuged (3300 g for 2 minutes). Then the chloroplast pellet was re-suspended in 2 ml of HS buffer and moved onto a Percoll pad, before being centrifuged (1400 g for 8 minutes). The supernatant was discarded and the pellet resuspended in 10 ml HS buffer before being centrifuged (3000 g for 2 minutes) and finally being re-suspended in HS buffer (0.5 ml). Thylakoid membranes were prepared from the chloroplasts by taking 0.4 ml of the solution, centrifuging (7000 rpm for 2 minutes) and then re-suspending in HM buffer on ice for 5 minutes to osmotically lyse the chloroplasts, and so expose the thylakoid membranes that they

contain. This solution was then washed twice in HS buffer and once in HM buffer by centrifuging (14,000 rpm for 2 minutes) and re-suspending. Thylakoid membranes were then re-suspended in 0.4 ml HM buffer and kept on ice. Finally, thylakoid membranes were deposited on PLL covered glass bottomed petri dishes immediately before experiments.

6.4 Simulations and Theory

Nanoscale electrodes are extremely difficult to characterize,[50] and therefore a steady-state three-dimensional FEM simulation of nanoscale DCEs in bulk solution was used to estimate the probe geometry from the in-situ current measurements. In addition, simulations at varying concentrations of ascorbic acid and at series of distances from a surface (active and inactive) were conducted to compare the results of the simulation to experiments. A stationary reaction-diffusion equation describes the transport of species in this system and can be written as

$$D_i \nabla^2 c_i + R_i = 0 \tag{6.1}$$

where D_i is the diffusion coefficient for species i , c_i is the concentration of species i and R_i is the reaction term for species i. Up to three species were present: $FcTMA^+$ (i = 1), $FcTMA^{2+}$ (i = 2) and ascorbic acid ($C_6H_8O_6$, i = 3). The diffusion constants were 6.0 $\times$ 10^{-6} cm^2 s^{-1}, 6.0 $\times$ 10^{-6} cm^2 s^{-1} and 1.0 $\times$ 10^{-5} cm^2 s^{-1}, respectively.[48,51] The reaction term, R_i, describes the oxidation of ascorbic acid by $FcTMA^{2+}$, which in turn is reduced to $FcTMA^+$:

$$C_6H_8O_6 + 2FcTMA^{2+} \xrightarrow{k} C_6H_6O_6 + 2FcTMA^+ + 2H^+ \tag{6.2}$$

where k is the homogeneous rate constant. Note the FEM simulation does not account for the $C_6H_6O_6$ or the H^+ species because the former is electrochemically

inert, and measurements are made in a buffer solution.

Two configurations were simulated for calculating the geometry: (i) a single electrode oxidizing $FcTMA^+$ to $FcTMA^{2+}$ at a diffusion-limited rate while the other electrode was not connected and; (ii) a generation/collection configuration where $FcTMA^{2+}$ was generated from the oxidation of $FcTMA^+$ at one electrode, while being collected by reduction back to $FcTMA^+$ at the other electrode. In addition, two configurations were simulated for comparing experimental results with simulations: (i) a probe in generation/collection configuration, in bulk solution, with various concentrations of ascorbic acid and; (ii) a probe in generation/collection configuration at a series of distances from an active and inert substrate. Ascorbic acid (i = 3) and the reaction terms, R_i, were included in the simulations only when needed, otherwise they were excluded for computational efficiency.

Based on the probe geometry and dimensions observed in SEM images of typical nanoscale DCEs (e.g. Figure 6.1 B) a FEM model of the probe geometry was developed. The geometry and boundary condition of three dimensional FEM model is summarized in Figure 6.2. Each electrode is semi-elliptical in shape and its size is defined by major and minor axes. The major axis is the distance from the center of the electrode to the outside edge perpendicular to the septum separating the electrodes. The minor axis is the distance from the middle of the electrode to the edge of the electrode parallel to the septum. The size of the minor axis is the average of the two major axes, which is typical of what is observed within SEM images of nanoscale DCEs. The septum width and width of the glass surround of the electrodes is set as a fifth of the minor axis size. These proportions are based on typical SEM images of nanoscale DCEs, and, as such, the model is specifically for probes of this size. The outer wall of the probe has a taper angle of 10 degrees, which was typical. Configuring the model in this way means that there are only two independent variables in the FEM model ie. the major axis for each of the electrodes. Thus, in principle, only two current measurements are needed to deter-

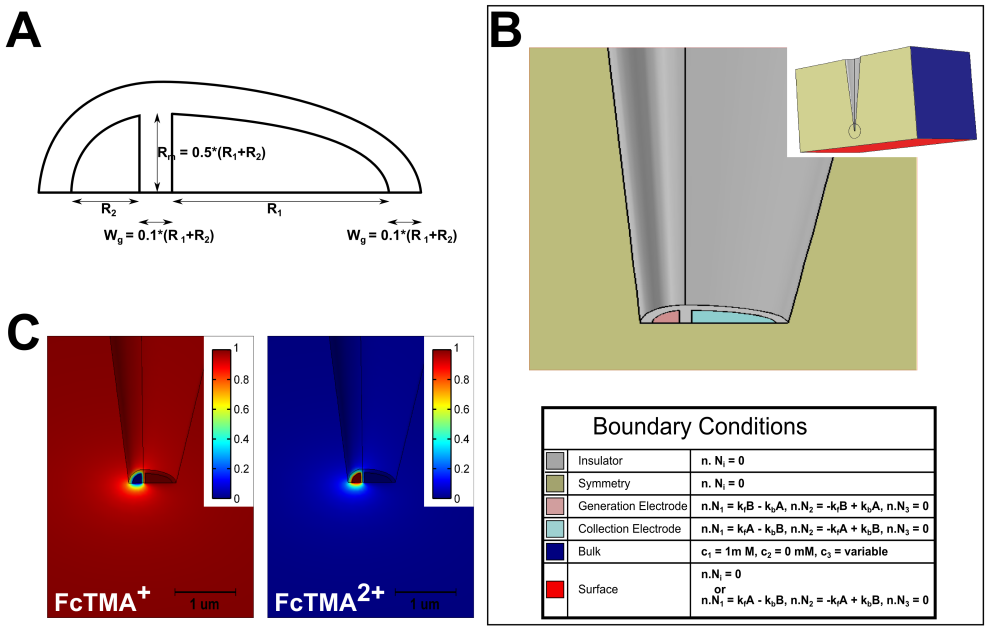

Figure 6.2: **A.** 2D diagram of the end of the probe showing dimensions used in the FEM model. R_1 is the major axis size of electrode 1 and R_2 the major axis size for electrode 2. W_g is the width of the glass surround and is set to $0.1 * (R_1 + R_2)$. R_m is the size of the minor axis of both electrodes, and is set to $0.5 * (R_1 + R_2)$. **B.** 3D geometry of the FEM model, with color coded boundary conditions. **C.** Typical diffusion profiles for $FcTMA^+$ and $FcTMA^{2+}$, when $FcTMA^{2+}$ is generated at the left electrode and collected at the right electrode.

mine the geometry of the probe. Recession, or protrusion, of the carbon from the probe is a possibility, however this is not considered in this simple initial model. Also the carbon electrode is assumed to have a uniform activity; although probes formed by pyrolytic carbon deposition have been shown to have a combination of conducting sp2 (graphitic) and non-conducting sp3 carbon.[52] A 2D representation of the dimensions of the end of the probe in Figure 6.2 A, the full 3D geometry of the model in Figure 6.2 B with the boundary conditions, and examples of typical diffusion profiles of $FcTMA^+$ and $FcTMA^{2+}$ is shown in Figure 6.2 C.

The concentration of $FcTMA^+$ and $FcTMA^{2+}$ at the electrode surfaces are described by Butler-Voltmer kinetics, with $\alpha = 0.5$, an over potential, E-E0, of 0.5 V, and $k^0 = 1$ cm s^{-1}. Therefore, the flux of electroactive species, A and B, is defined

as $n.N_{\mathrm{FcTMA^+}} = k_f[\mathrm{FcTMA^+}] - k_b[\mathrm{FcTMA^{2+}}]$ and $n.N_{\mathrm{FcTMA^{2+}}} = -k_f[\mathrm{FcTMA^+}] + k_b[\mathrm{FcTMA^{2+}}]$, where $k_f = k^0 \exp^{-\alpha F(E-E0)/RT}$ and $k_b = k^0 \exp^{(1-\alpha)F(E-E0)/RT}$, n is the surface normal, R is the molar gas constant, T is the temperature (295 K) and F is Faradays constant. The initial condition for the simulations were 1 mM of $\mathrm{FcTMA^+}$, no $\mathrm{FcTMA^{2+}}$ and the ascorbic acid concentration, when present, was varied. The current at an electrode is calculated as

$$i = 2n_e F \int (Fl_i.n)dA \tag{6.3}$$

where n_e is the number of electrons in the redox reaction, A is the electrode surface and Fl_i is the flux of species i. Comsol 4.2a (Comsol) was used on a PC running Windows64 (Microsoft).

6.5 Results and Discussion

DCEs were quickly and easily fabricated with a high success rate on the day of use, taking approximately 3 minutes per tip. Due to the simplicity of fabrication, and possible fouling of the carbon electrodes between experiments, the DCEs were used for only one experiment before being discarded. A typical DCE (see Figure 6.1 B and C) consists of two planar semi-elliptical electrodes, separated by a septum and surrounded by a small amount of glass. The septum size and small surround of glass are typical for probes constructed from theta pipets by the laser pulling technique.[39,40,53]

Generally, the individual electrodes in a single probe are not the same size; this was attributed to asymmetries in the individual barrel sizes in the original theta pipet, in heating by the laser puller or in asymmetries induced during pyrolysis of the carbon. For an individual probe the steady-state currents for the oxidation of $\mathrm{FcTMA^+}$ was obtained from linear sweep voltammograms, for each electrode, while the other electrode was unconnected. Anodic LSVs were obtained by sweeping the

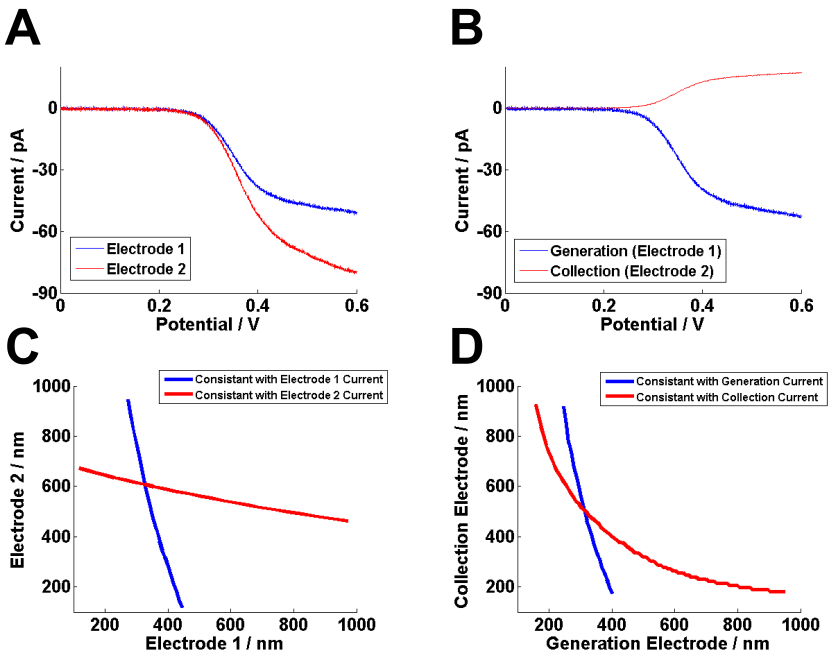

Figure 6.3: **A.** LSVs for the oxidation of $FcTMA^{+}$ to $FcTMA^{2+}$ at each individual electrode in a nanoscale DCE, while the other electrode was unconnected. **B.** LSVs for the generation and collection currents for $FcTMA^{+}/FcTMA^{2+}$. **C.** The set of geometry, for electrode 1 in blue and electrode 2 in red, calculated from a FEM model that is consistent with the single barrel currents. These two sets of geometries are self consistent at electrode 1 major axis radius 325 nm, and electrode 2 major axis radius 610 nm. **D.** The set of geometries, for electrode 1 in blue and electrode 2 in red, calculated from the FEM model that is consistent with the generation and collection currents. The two are self consistent at electrode 1 major axis radius 315 nm, and electrode 2 major axis radius 505 nm.

potential of the working electrode between 0 V and 0.6 V with respect to the QRCE for the oxidation of $FcTMA^{+}$ to $FcTMA^{2+}$ and are shown, for each electrode, in Figure 6.3 A. The LSVs show a reasonable, though not ideal, sigmoidal response, indicating a good seal between the carbon and the glass. The different magnitude of the limiting currents for each electrode, within an individual probe, indicates that the electrodes are not the same size.

This particular DCE was then used in generation/collection mode, with the $FcTMA^{+/2+}$ redox couple. The potential of the generation electrode was swept from 0 V to 0.6 V with respect to the QRCE for the oxidation of $FcTMA^{+}$ to $FcTMA^{2+}$

while potential of the collection electrode was held constant at 0 V for the reduction of $FcTMA^{2+}$ back to $FcTMA^{+}$. The resulting generation and collection currents are shown in Figure 6.3 B. The generation current shows the typical sigmoidal shape, however the magnitude of the limiting current is larger than that observed for the single electrode generation, as the second electrode is now regenerating $FcTMA^{+}$ and so providing a positive feedback component. The collection current shows a similar sigmoidal shape, resulting from the change in local $FcTMA^{2+}$ concentration induced by the generation electrode. The ratio of collection current to generation current defines the collection efficiency for a dual electrode system, and this probe had a diffusion limited collection efficiency of 30 %, which is typical. This high collection efficiency is achieved because of the small distance between the two electrodes allows a high rate of mass transport, through diffusion, between the electrodes.

6.5.1 Nanoscale DCE Characterization.

While nanoscale electrodes can be routinely fabricated,[54,55] the resulting probe geometry is often difficult to determine precisely.[50] In principle it is possible to determine the individual probe geometry for a DCE by SEM after experiments; however, this was found to be problematic due to crystallization of the redox species and supporting electrolyte on the probe on removal from the solution and exposure to air and rinsing of the probes in water was inefficient in removing this debris. Practically, the estimation of probe geometry is usually achieved by using analytical expressions, or simulations, to relate the experimental current responses to electrode dimension. Expressions for common geometries, such as planer disk electrodes,[56] are routinely used. More complex geometries, such as the probes used herein, need custom FEM simulations to determine probe geometries from in-situ current measurements. In formulating the FEM model the geometry and size of the glass surrounds and minor axis are assigned based on the size of the major axes of the two electrodes, this restricts the model to probes which are of this shape. However, from observing

typical SEM images of nanoscale DCEs, we believe this model captures the general geometry and so provides a reasonable basis by which to analysis initial experiments.

Using the FEM model the geometry of the nanoscale DCE used in Figure 6.2 A and B was calculated. Firstly, the geometry was calculated from the diffusion limited generation currents (Figure 6.2 A). The probe geometry (defined by the size of the axes) consistent with the diffusion limited current measured at electrode 1 was calculated and is shown in blue in Figure 6.3 C, while the probe geometry consistent with the measured limiting current for electrode 2 is shown in red. The point at which these two curves intersect, 325 nm for electrode 1 and 610 nm for electrode 2, is the only possible probe geometry, constrained by the model assumptions, which could produce the two individual electrode currents.

The geometry of the probe can also be calculated from the diffusion limited generation/collection currents, shown in Figure 6.3 B, using the FEM model. With electrode 1 generating $FcTMA^{2+}$ and electrode 2 collecting $FcTMA^{2+}$, the geometry consistent with the measured generation current was calculated and is shown in blue in Figure 6.3 D, while the geometry consistent with the measured collection current is shown in red. Again, the point at which these two sets of electrode sizes intersect, electrode 1 size of 315 nm and electrode 2 size of 505 nm, was the geometry of the probe, constrained by the model assumptions, calculated from the generation/collection currents. The size of electrode 1 was consistent, 315 nm versus 325 nm, between the two geometry calculations, however the size of electrode 2 differs by 105 nm, 505 nm compared to 610 nm. The difference in the calculated geometry suggests that the model captures the general probe geometry, although not to a high accuracy. Again, we must make clear that the geometry calculated for the nanoscale DCE is constrained by the model assumptions, such as the size of the glass surround, septum and minor axis, uniform activity of the electrode surface, and so reflects the apparent probe geometry of the probe which could, potentially, differ from the real probe geometry. However, this initial characterization of the

apparent probe geometry of an individual nanoscale DCE does allow subsequent experiments to be assessed.

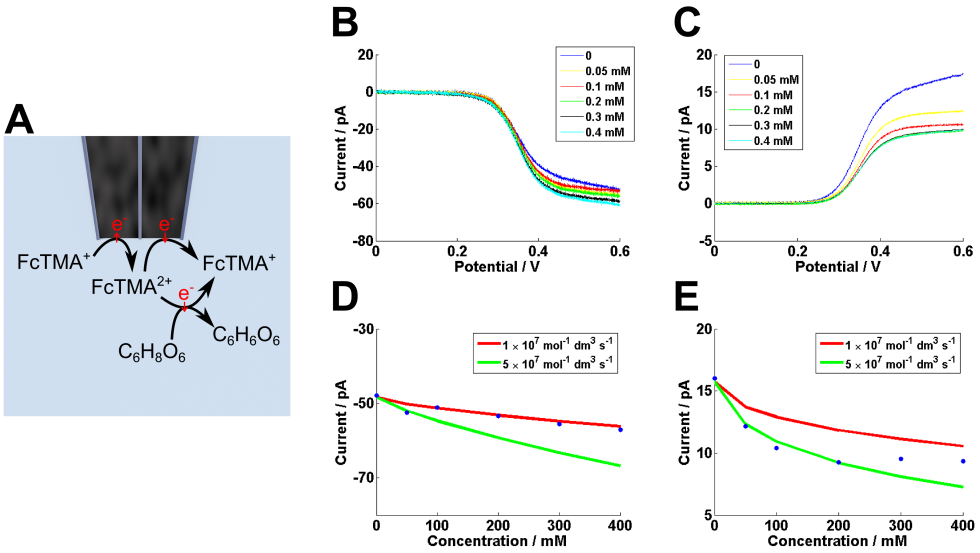

Figure 6.4: **A.** Schematic of a DCE in generation/collection mode, with the $FcTMA^{+/2+}$ couple, and ascorbic acid also reducing $FcTMA^{2+}$ in solution. **B.** and **C.** LSVs for the generation and collection of $FcTMA^{2+}$ at different concentrations of ascorbic acid. **D.** and **E.** Diffusion limited generation and collection currents at different ascorbic acid concentrations, and predicted responses from the FEM model. Changes in the generation and collection currents were detected in multiple experiments (N = 3), although the magnitude of the current changes varied (due to tip shape differences).

6.5.2 $FcTMA^{2+}$ oxidation of ascorbic acid.

The generation/collection configuration allowed the interaction of $FcTMA^{2+}$ with the important physiological agent, ascorbic acid, to be investigated. The nanoscale DCE described above, whose apparent geometry was calculated using the FEM model, was used in generation/collection mode in the presence of varying concentrations of ascorbic acid. The system, illustrated in Figure 6.4 A, is described by:

$$\text{Electrdoe1 : } FcTMA^{+} - e^{-} \rightarrow FcTMA^{2+}$$

$$\text{Electrdoe2 :FcTMA}^{2+} + e^- \rightarrow \text{FcTMA}^+$$

$$\text{Solution :2FcTMA}^{2+} + \text{C}_6\text{H}_8\text{O}_6 \xrightarrow{k} 2\text{FcTMA}^+ + \text{C}_6\text{H}_6\text{O}_6 + 2\text{H}^+$$

The probe was immersed in 1 mM FcTMA^+ solution, with different concentration of ascorbic acid, and a LSV, for the oxidation of FcTMA^+ at the generation electrode while the collection electrode was held at a constant potential for the collection of FcTMA^{2+}, was run. The resulting generation and collection currents are shown in Figure 6.4 B and C. The steady-state generation currents increased in magnitude with ascorbic acid concentration indicating that ascorbic acid was being oxidized by FcTMA^{2+}. At the same time the collection currents decreased, as the local concentration of FcTMA^{2+} in the neighborhood of the collection electrode reduced.

The FEM model, with a generation electrode with a major axis of 315 nm and a collection electrode with a major axis of 505 nm, was used to predict the changes in generation and collection currents at the range of ascorbic acid concentrations with a range of homogeneous rate constants, k. Figure 6.4 D and E show the changes in the diffusion limited generation and collection currents with different concentrations of ascorbic acid, and also the simulation results for two different rate constants. The predicted homogeneous rate constant, k, for the oxidation of ascorbic acid by FcTMA^{2+} is not consistent, with the generation current predicting 1×10^7 $\text{dm}^3\ \text{s}^{-1}\ \text{mol}^{-1}$ and the collection current predicting 5×10^7 $\text{dm}^3\ \text{s}^{-1}\ \text{mol}^{-1}$. These compare to values of 2.24×10^6 $\text{dm}^3\ \text{s}^{-1}\ \text{mol}^{-1}$ calculated using $[Fe(CN)_6]^{3-}$ [57] and 5.45×10^5 $\text{dm}^3\ \text{s}^{-1}\ \text{mol}^{-1}$ using FcTMA^{2+} from work in preparation (Eleni 2012 in preparation for Anal. Chem.). The size of the generation electrode was consistent for both methods of calculating the geometry and so it is not surprising the rate constant calculated from fitting the model to the generation electrode is closer to previously predicted values. However, this result highlights the difficulty in using the apparent electrode geometry to quantify experimental results, as any difference

with the real geometry will distort the result as the diffusion distance between the electrodes, and so the time that the active species ($FcTMA^{2+}$) has to interact with the third species (ascorbic acid).

6.5.3 Approach curves.

We now move onto using DCEs in a SECM configuration and investigated the behavior, in generation/collection mode, close to a surface. With $FcTMA^{+/2+}$ being oxidized and reduced respectively, DCEs were translated towards insert and active surfaces in IC-SECM mode.[44] Within IC-SECM the probe is oscillated normal to the surface (in this case at an amplitude of 32 nm at 70 Hz), and damping of the oscillation amplitude is detected when the tip comes into physical contact with the surface. This allows a current independent measure of the distance between the tip and the surface, which, in turn, allows for the conclusive determination of the distance between the probe tip and the surface during the approach curve measurements.

The generation and collection currents for approaches to glass (inert) and gold (active) surfaces are shown in Figure 6.5 A and B. The position at which the tip comes into contact with the surface is seen in the tip position oscillation amplitude, Figure 6.5 C and D, as a sharp drop, and this point is assigned a distance of 0 μm between the probe and the surface. When approaching to the inert substrate the generation current decreased, however the collection current increased before dropping when the tip is very close to the substrate. The increase in the collection current is a result of a blocking effect creating a thin layer cell between the end of the probe and the surface. The substrate confines the generated species, $FcTMA^{2+}$, close to the electrodes and results in a positive feedback response between the two electrodes. However, once the tip gets closer to the surface a decrease in the generation current is observed because of the blocking effect of the substrate restricting the availability of $FcTMA^{+}$. The generation/collection efficiency increased with the

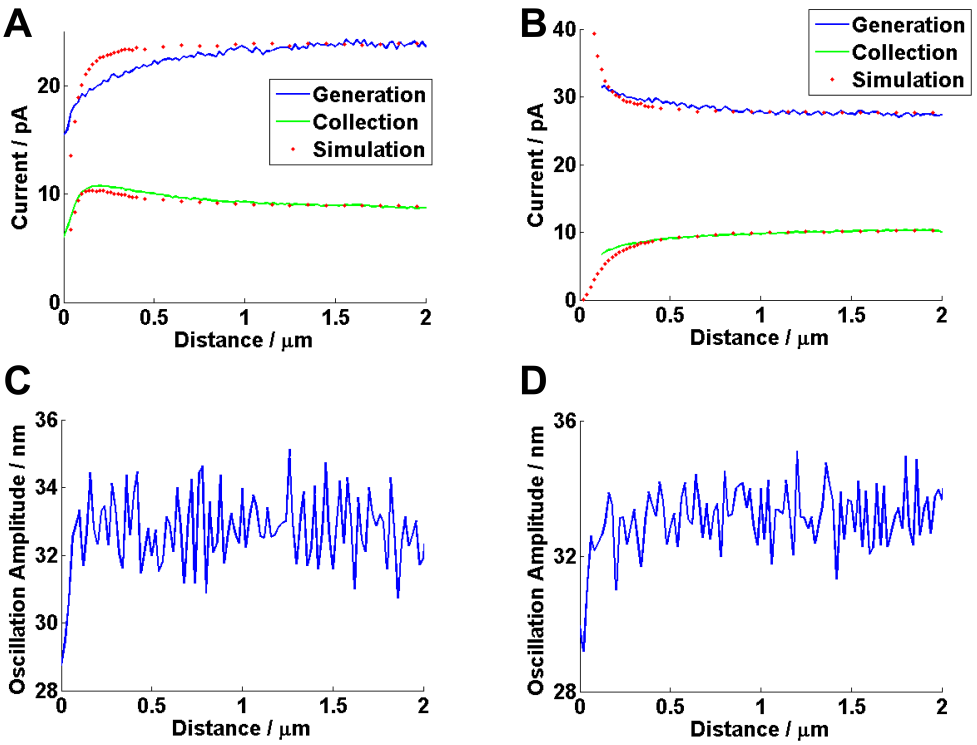

Figure 6.5: **A.** Generation and collection currents for an approach to an insulating (glass) substrate. Also shown, in red, are the results of a FEM model. **B.** Generation and collection currents, for an approach to a conducting (gold) substrate. Also shown, in red, are the results of a FEM model. **C.**and **D.** Probe oscillation amplitude for the approach shown in **A** and **B** respectively. IC-SECM worked consistently with dual electrode probes (N $\approx$ 10).

decrease in distance to the surface, and this continued even as the absolute generation and collection currents decrease. The approach to a conducting substrate shows that the generation current increased with the reduction of the distance to the substrate (positive feedback) while the collection electrode is in competition with the substrate and thus as the tip gets closer to the substrate the current on this electrode dropped. Note that the probe was not perfectly aligned to the surface, as both generation and collection currents fail to fall to zero over the insulating substrate. It is interesting that there is a point over the insulating surface at which the collection current reaches a maximum, and a probe positioned at this distance would be expected to have increased sensitivity to changes in the surface activity,

as measured by the collection current.

The FEM model is now used to assess the approach curve currents. The size of the individual probes was calculated from the steady-state generation and collection currents, as described above. For the approach to the insulating surface the apparent probe dimensions were calculated as 200 nm for the generation electrode and 490 nm for the collection electrode, while for the approach to the conducting surface the generation electrode was calculated as 160 nm and the collection electrode as 440 nm. Simulation results for approach curves, with the probe perfectly aligned to the surface, to both insulating and conducting substrates were calculated and are shown, as dots, in Figure 6.5 A and B. These show the same features as observed in the experimental results, most obviously the increase in collection current when approaching an insulating substrate. The generation current over the insulating surface shows some variation between the predicted current and the measured current, suggesting that the probe is at an angle with respect to the surface, or that the electrode size is larger than the apparent electrode size calculated from the steady state currents.

6.5.4 $FcTMA^{2+}$ reduction at thylakoid membranes.

Photosynthesis is the source of virtually all metabolic energy, hence represents an interesting and relevant biological system to investigate, and probe based electrochemical methods offer a new perspective on this system. Of particular interest are the light dependent components of photosynthesis which are, in higher plants, embedded within thylakoid membranes, which are themselves contained within chloroplasts. Within thylakoid membranes light is absorbed by chlorophyll, and other pigments, and this energy is transferred to photosystem II (PSII) where it is used to split water, producing molecular oxygen, protons and electrons.[58] An electron transport pathway, embedded within thylakoid membranes, then transfers the electrons through a number of intermediates, such a plastoquinone, the cytochrome b_6f complex, plas-

tocyanin and photosystem I, until ultimately the energy rich molecules NADPH and ATP are formed.[58] These are then be used in other processes, such as CO_2 fixation in the Calvin cycle, that take place outside the thylakoid membrane.[58] Interestingly, a number of artificial electron acceptors, such as potassium ferricyanide, methylviologen, 2,5-dichloro-p-benzoquinone, phenyl-p-benzoquinone, silicomolybdate and 2,6-dichlorophenol-indophenol,[58,59] can interact and be reduced by various components of this thylakoid membrane bound electron transport pathway. Electrochemical methods are ideal for directly detecting these artificial electron acceptors, as they can potentially be easily oxidized on an electrode surface. In particular, using a SECM configuration allows the electrode to be placed close but not touching, which could physically damage the sample, a thylakoid membrane and so gives very good temporal resolution measurements of the local artificial electron acceptor concentration.

The interaction of $FcTMA^{2+}$ with thylakoid membranes was investigated using the DCE shown in Figure 6.1 C in generation/collection mode, as illustrated in Figure 6.6 A. The probe was placed over a sparse monolayer of thylakoid membranes (a typical surface coverage is shown in Figure 6.6 B) and approached in the dark to the point of maximum collection current, as shown in the approach curve in Figure 6.6 C. The probe was then held stationary while the sample was illuminated using the fluorescence microscope (at a wavelength of 470 nm with an intensity of 3.5×10^{16} photons s^{-1} cm^{-2}) for 30 seconds and the generation and collection currents during this time were measured. Figure 6.6 D and E shows the relative change in the current-time transients during this period. Upon illumination it was apparent that $FcTMA^{2+}$ is reduced at the thylakoid membranes as an increased in the generation current and a decreased collection current was observed. Interestingly, a steady state response is quickly reached, with a ca. 30 pA increase in the generation current and a corresponding ca. 30 pA decrease in the collection current. The rate of $FcTMA^{2+}$ reduction decreases immediately on a return to the dark, as the number of electrons

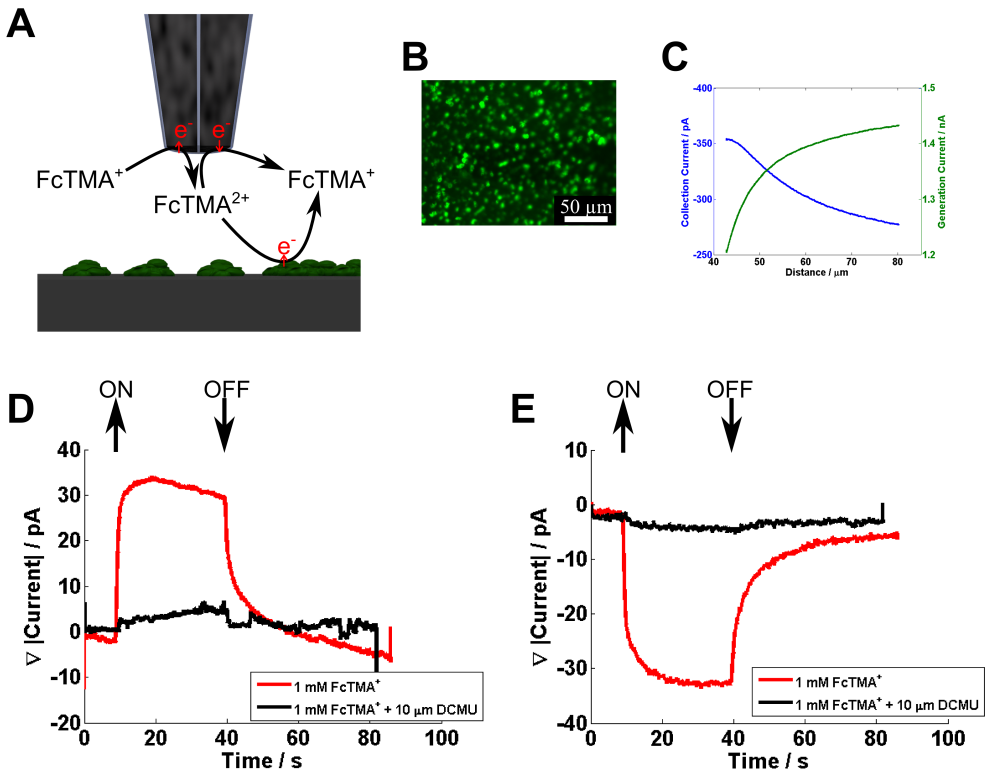

Figure 6.6: **A.** Schematic of the DCE in generation/collection mode, with the $FcTMA^{+/2+}$ couple, above a sparse monolayer of thylakoid membranes. **B.** Fluorescence microscopy image of a sparse monolayer of thylakoid membranes, observed as green spots on the surface. **C.** Approach curve for placing the DCE above the surface containing thylakoid membranes. **D.** Generation current response as the monolayer of thylakoid membranes is illuminated. **E.** Collection current response as the monolayer of thylakoid membranes is illuminated. The light stimulation response, and DCMU inhibitor response, was observed 50 % of the time (N = 4).

present within the electron transport pathway decreases, until the initial state is once again achieved.

To confirm the $FcTMA^{2+}$ interaction, the herbicide, DCMU, which blocks the binding site for plastioquinone to PSII, and in doing so blocks the linear electron transport pathway was added.[58] As observed in Figure 6.6 D and E the addition of 10 μm DCMU almost entirely eliminated the light mediated response. This confirms that $FcTMA^{2+}$ is being reduced by a component, currently unidentified, of the photosynthetic electron transport pathway. We can exclude the possibility of $FcTMA^{2+}$

accepting electrons directly from PSII, as is the case with silicomolybdate,[58] because DCMU has an effect on the $FcTMA^{2+}$ reduction.

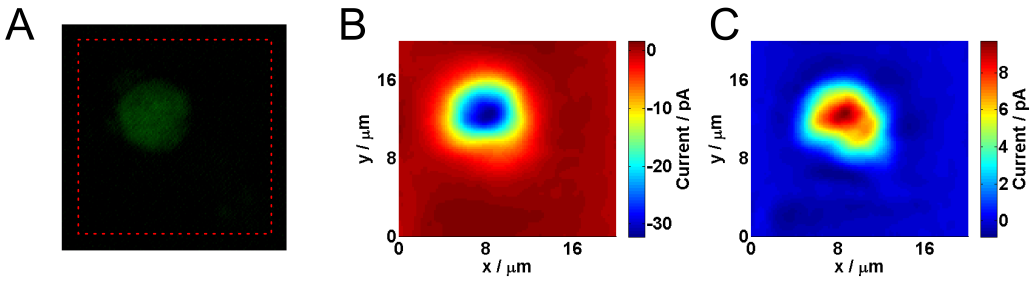

Figure 6.7: **A.** Fluorescence image of the single thylakoid membranes, with the scan area indicated by the red dotted line. **B.** Generation current image of the thylakoid membrane. **C.** Collection current image of the thylakoid membrane. SECM imaging using dual electrode probes was successful except when the probe was place very close to the surface and made direct contact with the thylakoid membrane, dragging it along the surface.

6.5.5 Thylakoid membrane imaging.

Finally, a DCE was used to obtain an image of a single thylakoid membrane. The probe was placed directly above a thylakoid membrane at the point of maximum collection current and then scanned laterally across the sample at a constant height in generation/collection mode. The sample was illuminated (470 nm, at 3.5×10^{16} photons s^{-1} cm^{-2}) during the scan. Two images of the surface, one from the generation current and one from the collection current, are shown, along with an image of the thylakoid membrane, in Figure 6.7. The single thylakoid membrane is present in all images, including both the generation current and collection current images. Thylakoid membranes are typically 2-4 μm in height, and therefore the features in both current images are predominantly produced from local topography changes and not from the local changes in substrate activity. Although, a simple constant height SECM imaging technique, that used no position feedback mechanism, was presented here, more complex techniques, such as using one electrode to sense topography and the other to sense substrate activity,[37] can be utilized using these probes.

6.6 Conclusions

DCEs are simple and fast to fabricate and a wide range of electrode sizes, from 100 nm to 50 μm, can be constructed. The probes are well suited to SECM experiments because of the relatively large electrode size, with respect to the total size of the end of the probe, and the small interelectrode distance. In particular, when operated in generation/collection mode generated collection efficiencies of up to 30 % were recorded, and therefore both the generation and collection currents provide a measure of the local activity.

For nanoscale DCEs a FEM model was developed to assist in characterizing the probe geometry based on in-situ current measurements. The geometry of the probe was calculated from either the single barrel $FcTMA^+$ oxidation currents, or alternatively the generation/collection currents. This allowed us to calculate the apparent probe geometry from two different measurements and compare them. The geometry was largely consistent between the two calculation methods. The FEM simulation was then used to assess the homogeneous rate constant for the oxidation of ascorbic acid by $FcTMA^{2+}$. However, inconsistencies between the rate constant that best fit the generation current and the rate constant that best fit the collection current were observed. This was attributed to differences between the calcaulted geometry (apparent geometry) and the real probe geometry. This highlighted the difficulty of relying on the apparent probe geometry, calculated from current measurements, when extracting quantitative parameters.

We also demonstrated that DCEs can be used to interrogate interfaces and surfaces. The interaction of $FcTMA^{2+}$ with the thylakoid membrane bound photosynthetic electron transport pathway was observed for the first time. The DCE was used to first assess the changes in local changes in $FcTMA^+$ and $FcTMA^{2+}$ concentration during illumination of thylakoid membranes, and then, finally, a 2 D image, of a single thylakoid membrane was constructed by laterally scanning the

probe over the surface.

DCEs offer a platform, which is simple and quick to construct, from which many interesting interfacial reactions can be investigated. Further work to understand how to extract the geometry from current based measurements is expected to expand the quantitative capabilities of these probes. In addition, individual probes within the DCE can be functionalized, and therefore a wide range of different systems easily investigated when starting from a DCE probe.

6.7 Acknowledgements

The authors thank Marc Baghdadi and Neil Ebejer for probe fabrication advice, and Alexander Colburn for customized electronics. We thank the ERC for funding for P.R.U and B.P.N., EPSRC for a MOAC/DTC studentship for K.M. and the University of Warwick for a CS for B.P.N. Some equipment used in this research was obtained through Advantage West Midlands (AWM).

6.8 References

(1) Mirkin, V.; Fan, F.; Bard, J. *J. Electroanal. Chem.* **1992**, 328, 47-62.

(2) Mirkin, M. V.; Bard, A. J. *Anal. Chem.* **1992**, 64, 2293-2302.

(3) Bard, A. J.; Mirkin, M. V.; Unwin, P. R.; Wipf, D. O.; Wipf, David, O. *J. Phys. Chem.* **1992**, 96, 1861-1868.

(4) Zhou, J.; Zu, Y.; Bard, A. J. *J. Electroanal. Chem.* **2000**, 491, 22-29.

(5) Rodrguez-Lpez, J.; Alpuche-Avils, M. A.; Bard, A. J. *J. Am. Chem. Soc.* **2008**, 130, 16985-16995.

(6) Ahmed, S.; Shan, J.; Petrik, L.; Linkov, V. A. *Anal. Sci.* **2004**, 20, 1283-1287.

(7) Klenerman, D.; Korchev, Y. E.; Davis, S. *J. Curr. Opin. Chem. Biol.* **2011**, 15, 1-8.

(8) Takahashi, Y.; Shevchuk, A. I.; Novak, P.; Murakami, Y.; Shiku, H.; Korchev,

Y. E.; Matsue, T. *J. Am. Chem. Soc.* **2010**, 132, 10118-10126.

(9) Takahashi, Y.; Shevchuk, A. I.; Novak, P.; Babakinejad, B.; Macpherson, J.; Unwin, P. R.; Shiku, H.; Gorelik, J.; Klenerman, D.; Korchev, Y. E.; Matsue, T. *Proc. Natl. Acad. Sci. USA* **2012**, 1-6.

(10) Kurulugama, R. T.; Wipf, D. O.; Takacs, S. A.; Pongmayteegul, S.; Garris, P. A.; Baur, J. E. *Anal. Chem.* **2005**, 77, 1111-1117.

(11) Zhu, R.; Macfie, S. M.; Ding, Z. *J. Exp. Bot.* **2005**, 56, 2831-2838.

(12) Holt, K. B.; Bard, A. *J. Biochem.* **2005**, 44, 13214-13223.

(13) Yasukawa, T.; Kaya, T.; Matsue, T. *Electroanal.* **2000**, 12, 653-659.

(14) Pierce, D. T.; Unwin, P. R.; Bard, A. J. *Anal. Chem.* **1992**, 64, 1795-1804.

(15) Wang, W.; Li, X.; Wang, X.; Shang, H.; Liu, X.; Lu, X. *J. Phys. Chem. B* **2010**, 114, 10436-10441.

(16) Guo, J.; Amemiya, S. *Anal. Chem.* **2005**, 77, 2147-2156.

(17) Tsionsky, M.; Zhou, J.; Amemiya, S.; Fan, F.-R. F.; Bard, A. J.; Dryfe, R. A. W. *Anal. Chem.* **1999**, 71, 4300-4305.

(18) Amemiya, S.; Bard, A. J. *Anal. Chem.* **2000**, 72, 4940-4948.

(19) Sun, P.; Mirkin, M. V. *Anal. Chem.* **2006**, 78, 6526-6534.

(20) Gell, A. G.; Ebejer, N.; Snowden, M. E.; Macpherson, J. V.; Unwin, P. R. *J. Am. Chem. Soc.* **2012**, 134, 7258-7261.

(21) Liu, S.; Li, Q.; Shao, Y. *Chem. Soc. Rev.* **2011**, 40, 2236-2253.

(22) Wei, C.; Bard, A. J.; Mirkin, M. V. *J. Phys. Chem.* **1995**, 99, 16033-16042.

(23) Edwards, M. A.; Martin, S.; Whitworth, A. L.; Macpherson, J. V.; Unwin, P. R. *Physiol. Meas.* **2006**, 27, R63-108.

(24) Husser, O.; Craston, D. *J. Vac. Sci. Technol. B* **1988**, 78712, 1873-1876.

(25) Mandler, D.; Bard, A. J. *J. Electrochem. Soc.* **1990**, 137, 1079-1086.

(26) De Abril, O.; Mandler, D.; Unwin, P. R. *Electrochem. Solid St.* **2004**, 7, C71.

(27) Kueng, A.; Kranz, C.; Mizaikoff, B. *Biosens. Bioelectron.* **2005**, 21, 346-353.

(28) Matysik, F.-M. *Electrochim. Acta* **1997**, 42, 3113-3116.

(29) Barnes, E. O.; Lewis, G. E. M.; Dale, S. E. C.; Marken, F.; Compton, R. G. *Analyst* **2012**, 137, 1068-1081.

(30) Albery, W. J.; Hitchman, M. L. Ring-Disc Electrodes; Clarendon Press: Oxford, 1971.

(31) Slowinska, K.; Feldberg, S. W.; Majda, M. *J. Electroanal. Chem.* **2003**, 554-555, 61-69.

(32) Bard, A. J.; Mirkin, M. V. Scanning Electrochemical Microscopy; Bard, A. J., Ed.; Marcel Dekker Inc: New York, 2001.

(33) Zhong, M.; Zhou, J.; Lunte, S. M.; Zhao, G.; Giolando, D. M.; Kirchhoff, J. R. *Anal. Chem.* **1996**, 68, 203-207.

(34) Liljeroth, P.; Johans, C.; Slevin, C. J.; Quinn, B. M.; Kontturi, K. *Electrochem. Commun.* **2002**, 4, 67-71.

(35) Fushimi, K.; Matsushita, K.; Hasegawa, Y. *Electrochim. Acta* **2011**, 56, 9602-9608.

(36) Yasukawa, T.; Kaya, T.; Matsue, T. *Anal. Chem.* **1999**, 71, 4637-4641.

(37) Isik, S.; Etienne, M.; Oni, J.; Blchl, A.; Reiter, S.; Schuhmann, W. *Anal. Chem.* **2004**, 76, 6389-6394.

(38) Gao, N.; Lin, X.; Jia, W.; Zhang, X.; Jin, W. *Talanta* **2007**, 73, 589-593.

(39) Yang, C.; Sun, P. *Anal. Chem.* **2009**, 81, 7496-7500.

(40) Takahashi, Y.; Shevchuk, A. I.; Novak, P.; Zhang, Y.; Ebejer, N.; Macpherson, J. V.; Unwin, P. R.; Pollard, A. J.; Roy, D.; Clifford, C. A.; Shiku, H.; Matsue, T.; Klenerman, D.; Korchev, Y. E. *Angew. Chem. Int. Edit.* **2011**, 50, 9638-9642.

(41) Matsue, T.; Koike, S.; Abe, T.; Itabashi, T.; Uchida, I. *Biochem. Biophys. Acta* **1992**, 1101, 69-72.

(42) Wong, D. K. Y.; Xu, L. Y. F. *Anal. Chem.* **1995**, 67, 4086-4090.

(43) Morton, K. C.; Morris, C. A.; Derylo, M. A.; Thakar, R.; Baker, L. A. *Anal. Chem.* **2011**, 83, 5447-5452.

(44) McKelvey, K.; Edwards, M. A.; Unwin, P. R. *Anal. Chem.* **2010**, 82, 6334-

6337.

(45) McKelvey, K.; Snowden, M. E.; Peruffo, M.; Unwin, P. R. *Anal. Chem.* **2011**, 83, 6447-6454.

(46) McGeouch, C.-A.; Peruffo, M.; Edwards, M. A.; Bindley, L. A.; Lazenby, R. A.; Mbogoro, M. M.; McKelvey, K.; Unwin, P. R. *J. Phys. Chem. C* **2012**, 116, 14892-14899.

(47) Patten, H. V.; Meadows, K. E.; Hutton, L. A.; Iacobini, J. G.; Battistel, D.; McKelvey, K.; Colburn, A. W.; Newton, M. E.; Macpherson, J. V.; Unwin, P. R. *Angew. Chem. Int. Edit.* **2012**, 51, 7002-7006.

(48) Bertoncello, P.; Ciani, I.; Li, F.; Unwin, P. R. *Langmuir* **2006**, 22, 10380-10388.

(49) Mills, W. R.; Joy, K. W. *Planta* **1980**, 148, 75-83.

(50) Nogala, W.; Velmurugan, J.; Mirkin, M. V. *Anal. Chem.* **2012**, 84, 5192-5197.

(51) Shamim, M.; Baki, S. M. A. *Aust. J. Chem.* **1980**, 123, 1857-1861.

(52) Pollard, A. J.; Faruqui, N.; Shaw, M.; Clifford, C. A.; Takahashi, Y.; Korchev, Y. E.; Ebejer, N.; Macpherson, J. V.; Unwin, P. R.; Roy, D. *MRS Proc.* **2012**, 1422.

(53) Snowden, M. E.; Gell, A. G.; Lai, S. C. S.; McKelvey, K.; Ebejer, N.; O'Connell, M. A.; Colburn, A. W.; Unwin, P. R. *Anal. Chem.* **2012**, 84, 2483-2491.

(54) Mirkin, M. V.; Nogala, W.; Velmurugan, J.; Wang, Y. *Phys. Chem. Chem. Phys.* **2011**, 13, 21196-21212.

(55) Sun, P.; Laforge, F. O.; Mirkin, M. V. *Phys. Chem. Chem. Phys.* **2007**, 9, 802-823.

(56) Wightman, R. M.; Wipf, D. O. In Electroanalytical Chemistry Vol. 15; Bard, A. J., Ed.; Marcel Dekker: New York, 1988; pp. 268-353.

(57) Rajantie, H.; Strutwolf, J.; Williams, D. E. *J. Electroanal. Chem.* **2001**, 500, 108-120.

(58) Hall, D. O.; Rao, K. K. Photosynthesis; Cambridge University Press, 1999.

(59) Shevela, D.; Messinger, J. *Biochem. Biophys. Acta* **2012**, 1817, 1208-1212.

Chapter 7

Meniscus Confined Fabrication of Nanoscale Multidimensional Conducting Polymer Structures with Positional Feedback

Scanning electrochemical cell microscopy (SECCM) is a EC-SPM technique that uses a liquid meniscus at the end of a dual barrelled pipet to create a positionable nanoscale electrochemical cell. We show that SECCM can be used to fabricate, through the electropolymerisation and deposition of conducting polymer, nanoscale structures on conducting surfaces and over insulating surface.

This chapter contains the communication that is in preparation. I was responsible for the experimental work, analysis and paper preparation. Michael A. O'Connell contributed to the AFM studies.

Meniscus Confined Fabrication of Nanoscale Multidimensional Conducting Polymer Structures with Positional Feedback

Kim McKelvey, Michael A. O'Connell, Patrick R. Unwin

In preparation

The fabrication of individual nanoscale structures is a huge field of burgeoning interest due to numerous potential applications spanning electronic devices,[1,2] sensors,[3,4] energy[5] and lifescience technologies.[6−9] While many fabrication methods abound,[10−12] probe-based techniques, such as dip pen[13,14] and fountain pen[15,16] lithography, electrospinning,[17,18] scanning electrochemical microscopy (SECM)[19−21] and meniscus-based methods[22−28] offer particularly exciting new ways to fabricate novel structures. Here, we show that multidimensional conducting polymer nanostructures can be created by electropolymerization using a meniscus-based technique that utilizes a dual barrel pipet probe, in a scanning electrochemical cell microscopy (SECCM) format.[29−32] Unlike previous meniscus-based techniques, which have used a single barrel pipet,[22−28] the use of a dual barrel (theta) pipet provides a positional feedback mechanism to control the distance between the end of the pipet and the surface, thus preventing pipet crash, or the meniscus becoming detached from, the surface (*vide infra*). We note that the structures demonstrated with single channel probes have tended to make contact with a substrate surface at a limited number of points.[22−28]

Theta pipets have previously been used to pattern biomolecules and water droplets on electrically insulating surfaces.[33,34] The studies herein show that the approach can be developed towards reactive systems by using a liquid meniscus at the end of a dual barrel probe to carry out electropolymerization and the deposition of extended multidimensional conducting polymer structures. Moreover, because we use a probe which is, in essence, a nanoscopic electrochemical cell, we have a means of controlling the rate of deposition as well as analyzing and adjusting the rate in real time. This greatly expands the usability of meniscus-based fabrication techniques.

Intrinsically conducting polymers, such a polyaniline (PANI), polypyrrole and poly(p-phenylene vinylene), possess both metallic (such as electronic conductivity) and polymeric (such as flexibility) properties,[35] making them attractive materials from which to fabricate novel devices, such as one dimensional nanowires.[36,37] The focus herein is PANI which offers highly tuneable conductivity, good environmental stability and ease of synthesis.[38,39] Electrochemical polymerization in aqueous media at a neutral pH typically results in a non-conducting emeraldine base form of PANI, however at acidic pH (pH $<$ 3) the polymer is doped and a conducting emeraldine salt form of PANI is produced.[39]

For the approach herein, the meniscus at the end of the dual barrel pipet was used to deliver aniline to an electrode surface in a defined manner, and, by adjusting the potential of the surface, localized electropolymerization could be carried out, with a resolution defined by the size of the meniscus. Figure 7.1 A shows a scanning electron micrograph (SEM) of a typical probe, created from a borosilicate glass theta pipet, pulled using a laser puller. Each barrel is approximately equal in size and separated by a small septum at the centre. The pipet was filled with solution containing aniline, and supporting electrolyte (*vide infra*), and an Ag/AgCl quasi reference counter electrode (QRCE) was inserted into each barrel.

An ionic conductance current, i_{Barrel}, was induced across the meniscus by

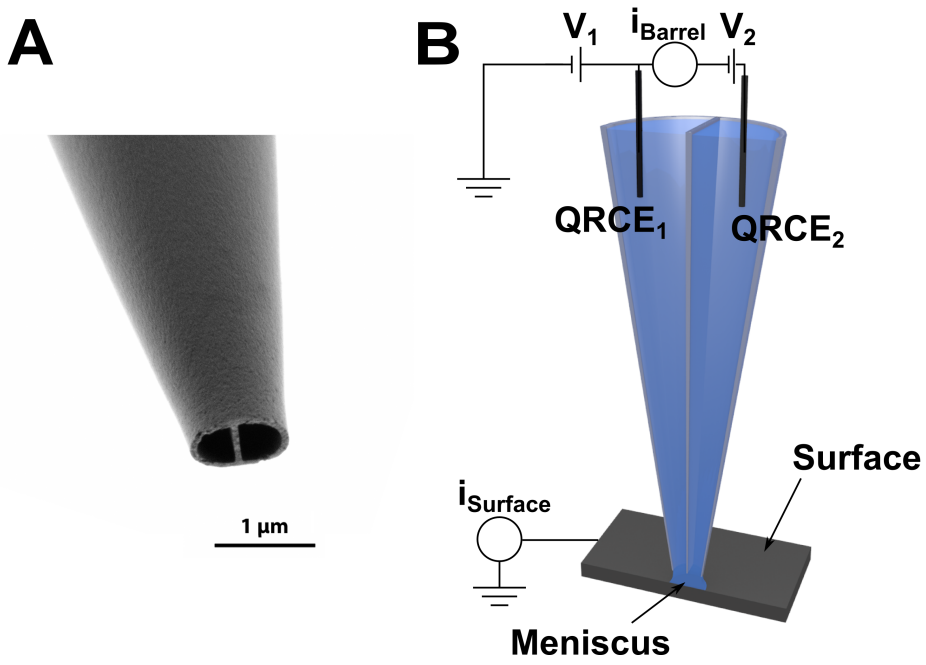

Figure 7.1: **A.** SEM image of a typical SECCM probe. **B.** Schematic of the electrochemical configuration for the SECCM patterning studies. The surface electrode was held at ground, and the surface current was measured as $i_{Surface}$. A potential difference of V_2 was applied between QRCEs in each barrel and the current between the barrels measured as i_{Barrel}. The two QRCEs were floated, with respect to ground, by a potential V_1. Because the pipet is highly symmetric, and the contact area is small, the effective potential of the surface electrode with respect to the QRCEs is ca. -(V_1+V_2/2).

applying a potential difference (V_2 in Figure 7.1 B), typically 100 mV, between the QRCEs using a custom bipotentiostat. Positional feedback was achieved by oscillating the probe normal to the surface of interest (typically 230 Hz and 80 nm amplitude), such that the meniscus deformed at the probe oscillation frequency when it came into contact with the substrate. The resulting AC component of the conductance current, extracted using a lock-in amplifier, was used as a set point for positional feedback of the probe.[29,30] In essence, a constant AC value maintained the distance between the end of the pipet and the surface, avoiding the probe either crashing into the surface or the meniscus becoming detached from the surface, as the surface was moved laterally under the probe.

PANI was formed through electropolymerization, from aniline, at the interface of the meniscus and the substrate. See supporting information Figure 7.5 for a characteristic cyclic voltammogram for electropolymerization from an SECCM probe on a gold substrate, which highlights an onset potential of ca. 0.8 V for electropolymerization[39,40] and that little detectable over-oxidation occurs at potentials where patterning was carried out. The driving force for polymerization was controllable precisely, because the substrate electrode was held at a potential of ca. -(V_1+V_2/2) with respect to the QRCEs (Figure 7.1 B).[30] In addition, the current induced by electropolymerization was measured at the substrate ($i_{Surface}$ in Figure 7.1 B) to provide direct information on the process. A galvanostatic operation mode was also assessed, in which the substrate (polymerization) current was maintained at a user-defined value by automatically adjusting the potential, V_1 in Figure 7.1 B, of the substrate with respect the QRCEs.

Patterns of conducting polymer can be constructed on conducting (gold) surfaces by either: (i) controlling the position at which the liquid meniscus makes contact with the surface, held at a potential that always drives the reaction; or (ii) by controlling the potential of the surface so that the reaction is 'on' or 'off' with the meniscus always in contact. To demonstrate the first approach, patterns of dots on a conducting surface (gold) were created by controlling the position of contact. Figure 7.2 A shows a SEM image of an array of ca. 200 nm radius PANI. The array took 641 seconds to construct, of which the meniscus was only in contact with the surface for ca. 33 seconds. The dots were made by approaching the meniscus to the surface at 50 nm s^{-1} until contact was detected, and then retracting a distance of 1 μm at a speed of 200 nm s^{-1}. The probe was then moved laterally to the next dot position (at 5 μm s^{-1}) and again approached towards the surface. Throughout, the surface was held at a potential of 1.2 V with respect to the QRCEs to drive the oxidative polymerization of aniline (pH 7.2) whenever the meniscus was in contact with the surface. In this case, PANI was deposited in the non-conducting form,

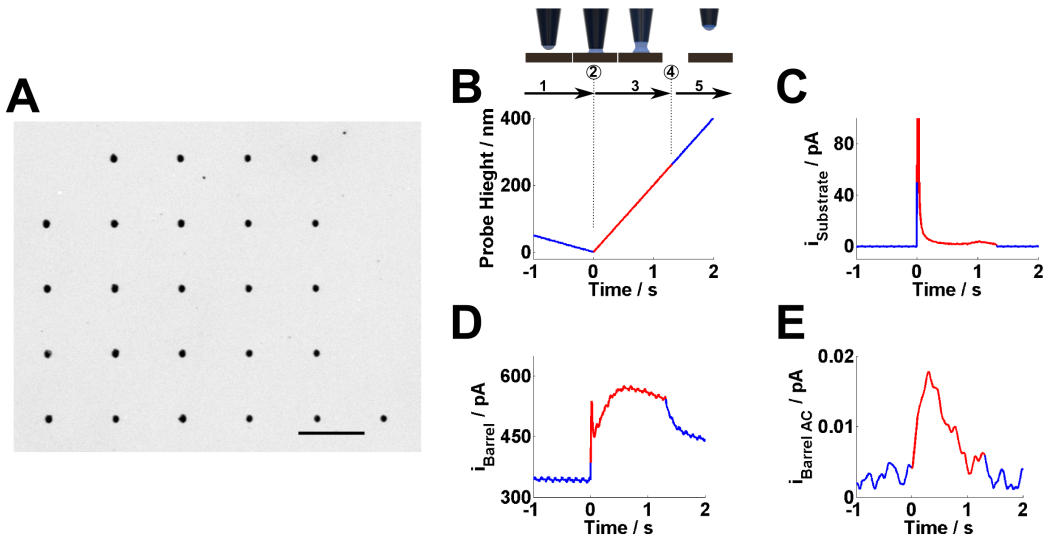

Figure 7.2: **A.** SEM of an array of 25 dots created by controlling the contact points between the liquid meniscus and the surface. The left top dot was created first, and the right bottom the last. Scale bar represents 5 μm. Typical current responses for one dot is shown on the right with the probe position (**B**), substrate current (**C**), barrel current (**D**), and ac barrel current magnitude (**E**). The different stages of the probe movement are highlighted on B: 1 probe approaches the surface; 2 meniscus comes into contact with the surface; 3 probe is retracted from the surface; 4 the meniscus detaches; 5 the probe continues to move away from the surface. The fabrication of dots was consistently successful on gold (N = 8), however on other surfaces (such as HOPG) some leaking of the meniscus was observed.

from the phosphate buffer (pH 7.2) solution, so that the process was self-limiting.

The tip position (probe height), substrate current ($i_{Surface}$) and both DC and AC components of the barrel current (i_{Barrel}) are recorded during deposition, and a typical response for each is shown in Figure 7.2 B through E. For clarity, the different stages of the probe movement scheme during the creation of one dot are illustrated in Figure 7.2 B. In the region marked 1, the tip is brought towards the surface, with a probe height of zero assigned as the point where the meniscus makes contact with the surface. During this period, with the probe and meniscus in air, there is no substrate current (Figure 7.2 C), a constant DC current of 330 pA between the barrels (Figure 7.2 D) and a barely detectable AC current (Figure 7.2 E). When the meniscus makes contact with the substrate, point 2, there is a significant change

in all 3 current measurements. First, a current flows through the substrate due to the electropolymerization process (Figure 7.2 C). There is a surge in the barrel current, largely due to a increase in the thickness of the meniscus, as a consequence of a jump to contact with the surface, while the AC magnitude increases due to the periodic modulation of the meniscus trapped between the oscillating probe and the surface.[30]

The procedure implemented was to translate the probe away from the surface immediately at contact (Figure 7.2 B, region 3 - 5). The AC and DC between the barrels indicate that the meniscus maintains contact with the surface for about 200 nm and then detaches (Figure 7.2 B, point 4). During this contact, the electropolymerization process proceeds, although the rate (substrate current) decreases significantly, after an initial rapid rise, because the PANI was deposited in a non-conducting form, passivating the surface and preventing significant PANI formation. Individual dot size, extracted from the SEM image, and surface charge, extracted from the integrated area of the surface current, were analyzed (see supporting information Figure 7.6), and this shows a consistency of dot size (area) over the array of dots (0.37 ± 0.04 μm^2), and that there is generally an increase in surface charge (8.0 ± 0.5 pC), associated with increased dot size.

Next, patterns were produced by the second method, moving the meniscus laterally across the surface while controlling the effective potential of the substrate surface, $V_{Substrate}$, with respect to the QRCEs in the barrels of the probe, by changing V_1, while V_2 was fixed, as is demonstrated in Figure 7.3 A(i). A 1 μm diameter probe was used, and for this study, and all following studies, PANI was deposited in its conducting form from a pH 1.6 aniline solution. The probe was moved laterally over the substrate, with the meniscus kept in contact with the surface throughout (see supporting information Figure 7.7 which shows a strong AC current signal used for positioning). A substrate current, of ca. 20 - 30 pA (Figure 7.3 A(ii)), was measured when the potential of the surface (1.2 V) was sufficient to drive the for-

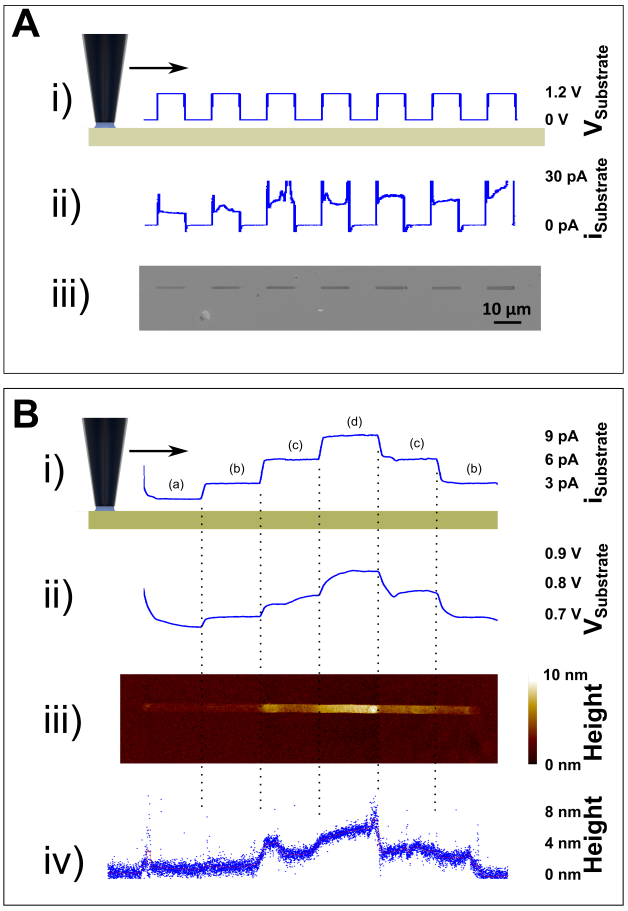

Figure 7.3: **A.** Patterning of PANI on a gold surface by controlling the surface potential (i) while the meniscus is scanned across surface. The measured substrate current (ii) indicates the magnitude of the polymerization rate as does the SEM micrograph of the resulting PANI pattern (iii). **B.** Galvanostatic control of PANI electrodeposition as a meniscus is moved, in contact, laterally across a gold surface electrode surface: (i) measured substrate current stepped through values of (a) 1 pA (b) 3 pA (c) 6 pA and (d) 9 pA and corresponding applied surface potential (ii) to drive the surface current. The AFM image of the resulting pattern (iii) and cross section height (iv) qualitatively reflects the different applied substrate currents. The fabrication of patterns on active surfaces, in both potentiometric and galvanostatic modes, was successful 90 % of the time (N = 15), with leaking of the meniscus occasionally observed.

mation of PANI, while no current was measured when it was not (0 V). The SEM image (Figure 7.3 A(iii)) confirms the oxidative polymerization of aniline, producing PANI, only occurs when the potential of the surface was 1.2 V with respect to the

QRCEs. The result is a well-defined 'dashed line' with a width of ca 1 μm. The substrate current is consistently larger than observed for the fabrication of the dots, above, because PANI was deposited in its conducting form.

It can be seen that although the approach in Figure 7.3 A was successful, there is some variation in current during the deposition period and more control, particularly for the deposition of small amounts of material, might be achieved using a galvanostatic approach, in which a user-defined substrate current is maintained or applied in a defined fashion during patterning. This procedure and typical results are illustrated in Figure 7.3 B showing: (i) the current measured at the substrate (which closely matches the applied values, left to right, of 1 pA, 3 pA, 6 pA, 9 pA, 6 pA, and 3 pA); (ii) potential required to maintain the prescribed current; (iii) an AFM image of the resulting pattern; and (iv) the average cross-sectional height of the deposited line deduced from the AFM image. As a probe was moved laterally across the surface (at 300 nm s^{-1}) a user defined substrate current was maintained for 5 μm by adjusting the potential of the surface (V_1). A surface current of 1 pA generated a 0.9 $\pm$ 0.6 nm thick layer of PANI, while a surface current of 9 pA deposited a 5 $\pm$ 0.7 nm thick layer of PANI. This experiment demonstrates that it is possible to move a meniscus based probe across a surface, using one feedback loop to control the contact of the meniscus with the surface, while another feedback loops controls the quantity of PANI deposited on the surface.

Finally, we show that structures protruding out from the surface can be constructed by drawing the meniscus away from the surface while depositing PANI. Note that previous reports, using single barrel meniscus probes, have retracted the pipet at a set rate to make towers and vertical wires, with the rate of pipet movement selected (by trial and error) to correspond to the growth rate of the structure.[23,24] In contrast, in the SECCM method, the ion conductance (AC) feedback is used to follow the structure as it grows, and to move the probe accordingly.

Figure 7.4 shows a three-dimensional structure that started on a conducting

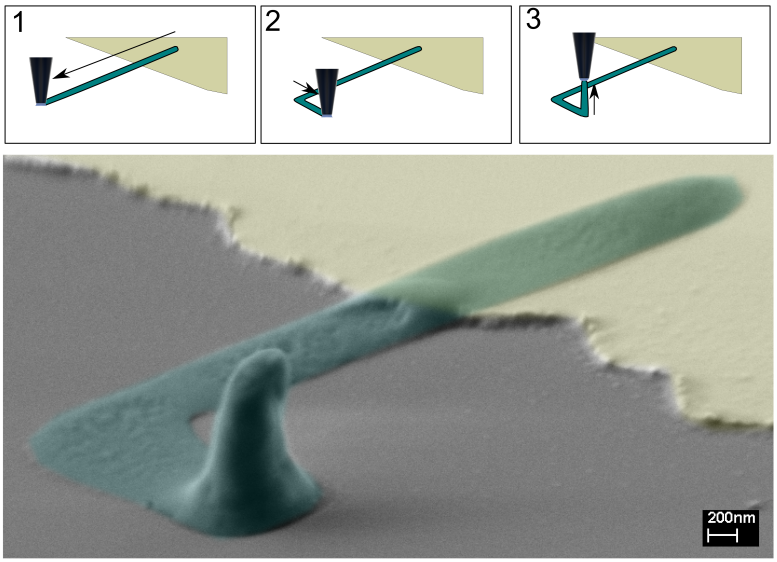

Figure 7.4: SEM (false color) of a three dimensional PANI structure (green) created on a conducting (gold) and non-conducting (grey) surface. The probe movement steps are shown as: 1 the lateral movement from a conducting substrate and over an insulating substrate; 2 the change in lateral movement direction on an insulating substrate; and 3 moving the probe away from the surface. Fabrication of 3D structures over insulating backgrounds was successful 40 % of the time (N = 20), due to disruption of PANI deposition at the edge of the gold.

substrate but then moved out across an insulating substrate (shown in schematic 1 of Figure 7.4). The laterally direction of the probe was then changed to turn a 1-D nanowire into a 2-D pattern on the insulating substrate (shown in schematic 2 of Figure 7.4). This highlights that good electrical contact is maintained between the polymeric nanowire and the gold contact, even when the wire is on an insulating substrate. Finally, a three-dimensional structure was created by growing a tower out of the surface by moving the probe away from the surface (shown in schematic 3 of Figure 7.4). This experiment illustrates the power of using a dual barrel pipet, with positional feedback, to construct multidimensional nanostructures.

In conclusion, we have demonstrated the use of a dual barrel SECCM-based meniscus method to create multidimensional PANI nanostructures on conducting substrates, across insulating (inert) areas of a surface, and ultimately to produce 3D

structures. Positional feedback of the probe and meniscus is generated from the ionic conductance barrel current between the QRCEs in each barrel of the SECCM probe. This affords positional control of the probe, with respect to the surface, allowing the probe to track a variety of surfaces, without fear of the meniscus losing contact or the probe crashing into the surface. Patterns on a conducting substrate were demonstrated by controlling either the position at which the liquid meniscus came into contact with the substrate, or the potential of the substrate (with the meniscus always in contact). Finally, to illustrate the possibility of constructing complex patterns, a multidimensional structure was constructed on a surface with conducting and insulating regions. Given the wide range of materials that can be created by electrodeposition, we expect the SECCM nanofabrication technique to have a wide application in the future, particularly for the creation of novel nanodevices and sensing elements using soft materials that maybe difficult to deposit with other techniques.

7.1 Experimental

Solutions. 20 mM aniline hydrochloride (Sigma-Aldrich) in phosphate buffer pH 7.2 (Sigma Aldrich) or 20 mM aniline hydrochloride in Milli-Q water (Millipore Corp.) with 75 μml HCl (36 %, Sigma-Aldrich) solutions (pH 1.6) were used.

Substrates. Gold electrodes (100 - 200 nm thick) on SiO_2 substrates were created by a lift off process.

Probes. Dual barrel borosilicate glass theta capillaries (o.d. 1.5 mm, i.d. 0.23 mm, Harvard Apparatus) were pulled using a laser puller (Model P-2000, Sutter Instruments) to produce tapered capillaries between 400 nm and 1 μm. The dimensions were accurately characterized by SEM (*vide infra*).

Electrochemical Instrumentation. Probes were filled with the appropriate electrolyte solution, and Ag/AgCl QRCEs inserted into each barrel. The QRCEs were

connected to a custom bipotentiostat, and the substrate was connected to a custom current follower. The probe was mounted on a piezoelectric positioner (P-753 LISA, Physik Intrumente) which was, in turn, mounted on micropositioners (Newport Corp.) and the substrate was mounted on XY piezoelectric positioners (Nano-Bio300, MadCityLabs). This was situated on an optics table (RS2000, Newport Corp.) within a faraday cage. A lock-in amplifier (SR830 DSP, Stanford Research Systems) was used to extract the AC components of the ionic conductance current between the QRCEs. The bipotentiostat and piezoelectric positioners were controlled, and the currents measured, through a PC running custom LabVIEW2011 (National Instruments) code through a FPGA card (7852R, National Instruments). The procedure used to control the position of the probe with respect to the substrate has been describe in detail previously [29].

Scanning Electron Microscopy. A Zeiss Supra 55-VP, at acceleration voltage of 1 kV, was used.

7.2 Acknowledgments

We thank Massimo Peruffo, Aleix Gell, Stanley Lai and Anisha Patel for useful discussions. We thank Aleix Gell for substrate preparation and the EPSRC and MOAC for a studentship to K.M. P.R.U acknowledges support from a European Research Council Advanced Investigator Grant (ERC-2009-AdG247143 Quantif). Some of the equipment used in this work was obtained through the Science City Advanced Materials project with support from Advantage West Midlands and the European Regional Development Fund.

7.3 References

(1) Wang, Z. L. *Adv. Mater.* **2012**, 24, 4632-46.

(2) Lee, Y. T.; Jeon, P. J.; Lee, K. H.; Ha, R.; Choi, H.-J.; Im, S. *Adv. Mater.*

2012, 24, 3020-3025.

(3) Shim, J. H.; Lee, Y.; Kang, M.; Lee, J.; Baik, J. M.; Lee, Y.; Lee, C.; Kim, M. H. *Anal. Chem.* **2012**, 84, 3827-3832.

(4) Penner, R. M. Ann. Rev. *Anal. Chem.* **2012**, 5, 461-485.

(5) Hochbaum, A. I.; Chen, R.; Delgado, R. D.; Liang, W.; Garnett, E. C.; Najarian, M.; Majumdar, A.; Yang, P. *Nature* **2008**, 451, 163-167.

(6) Xie, C.; Lin, Z.; Hanson, L.; Cui, Y.; Cui, B. *Nat. Nanotechnol.* **2012**, 7, 185-190.

(7) Shalek, A. K.; Robinson, J. T.; Karp, E. S.; Lee, J. S.; Ahn, D.-R.; Yoon, M.-H.; Sutton, A.; Jorgolli, M.; Gertner, R. S.; Gujral, T. S.; MacBeath, G.; Yang, E. G.; Park, H. *Proc. Natl. Acad. Sci. USA* **2010**, 107, 1870-1875.

(8) Robinson, J. T.; Jorgolli, M.; Shalek, A. K.; Yoon, M.-H.; Gertner, R. S.; Park, H. *Nat. Nanotechnol.* **2012**, 7, 180-184.

(9) Duan, X.; Gao, R.; Xie, P.; Cohen-Karni, T.; Qing, Q.; Choe, H. S.; Tian, B.; Jiang, X.; Lieber, C. M. *Nat. Nanotechnol.* **2012**, 7, 174-179.

(10) Xia, Y.; Rogers, J. A.; Paul, K. E.; Whitesides, G. M. *Chem. Rev.* **1999**, 99, 1823-1848.

(11) Smith, E. J.; Makarov, D.; Schmidt, O. G. *Soft Matter* **2011**, 7, 11309-11313.

(12) Nam, K. H.; Park, I. H.; Ko, S. H. *Nature* **2012**, 485, 221-224.

(13) Salaita, K.; Wang, Y.; Mirkin, C. A. *Nat. Nanotechnol.* **2007**, 2, 145-155.

(14) Basnar, B.; Willner, I. *Small* **2009**, 5, 28-44.

(15) Deladi, S.; Tas, N. R.; Berenschot, J. W.; Krijnen, G. J. M.; de Boer, M. J.; de Boer, J. H.; Peter, M.; Elwenspoek, M. C. *App. Phys. Lett.* **2004**, 85, 5361-5363.

(16) Kim, K.-H.; Moldovan, N.; Espinosa, H. D. *Small* **2005**, 1, 632-635.

(17) Sun, D.; Chang, C.; Li, S.; Lin, L. *Nano Lett.* **2006**, 6, 839-842.

(18) Bisht, G. S.; Canton, G.; Mirsepassi, A.; Kulinsky, L.; Oh, S.; Dunn-Rankin, D.; Madou, M. J. *Nano Lett.* **2011**, 11, 1831-1837.

(19) Zhou, J.; Wipf, D. O. *J. Electrochem. Soc.* **1997**, 144, 1202-1207.

(20) Sheffer, M.; Mandler, D. *J. Electrochem. Soc.* **1995**, 142, 82-84.

(21) Deiss, F.; Combellas, C.; Fretigny, C.; Sojic, N.; Kanoufi, F. *Anal. Chem.* **2010**, 82, 5169-5175.

(22) Grilli, S.; Coppola, S.; Vespini, V.; Merola, F.; Finizio, A.; Ferraro, P. *Proc. Natl. Acad. Sci. USA* **2011**, 108, 15106-15111.

(23) Hu, J.; Yu, M.-F. *Science* **2010**, 329, 313-316.

(24) Kim, J. T.; Seol, S. K.; Pyo, J.; Lee, J. S.; Je, J. H.; Margaritondo, G. *Adv. Mater.* **2011**, 23, 1968-1970.

(25) Laslau, C.; Williams, D. E.; Kannan, B.; Travas-Sejdic, J. *Adv. Funct. Mater.* **2011**, 21, 4607-4616.

(26) Laslau, C.; Williams, D. E.; Travas-Sejdic, J. *Prog. Polym. Sci.* **2012**, 37, 1177-1191.

(27) Yang, D.; Han, L.; Yang, Y.; Zhao, L.-B.; Zong, C.; Huang, Y.-F.; Zhan, D.; Tian, Z.-Q. *Angew. Chem. Int. Edit.* **2011**, 50, 8679-8682.

(28) Zhan, D.; Yang, D.; Zhu, Y.; Wu, X.; Tian, Z.-Q. *Chem. Comm.* **2012**, 48, 11449-11451.

(29) Ebejer, N.; Schnippering, M.; Colburn, A. W.; Edwards, M. A.; Unwin, P. R. *Anal. Chem.* **2010**, 82, 9141-9145.

(30) Snowden, M. E.; Gell, A. G.; Lai, S. C. S.; McKelvey, K.; Ebejer, N.; O'Connell, M. A.; Colburn, A. W.; Unwin, P. R. *Anal. Chem.* **2012**, 84, 2483-2491.

(31) Gell, A. G.; Ebejer, N.; Snowden, M. E.; McKelvey, K.; Macpherson, J. V.; Unwin, P. R. *Proc. Natl. Acad. Sci. USA* **2012**, 109, 11487-11492.

(32) Lai, S. C. S.; Patel, A. N.; McKelvey, K.; Unwin, P. R. *Angew. Chem. Int. Edit.* **2012**, 51, 5405-5408.

(33) Rodolfa, K. T.; Bruckbauer, A.; Zhou, D.; Schevchuk, A. I.; Korchev, Y. E.; Klenerman, D. *Nano Lett.* **2006**, 6, 252-257.

(34) Rodolfa, K. T.; Bruckbauer, A.; Zhou, D.; Korchev, Y. E.; Klenerman, D. *Angew. Chem. Int. Edit.* **2005**, 44, 6854-6859.

(35) Macdiarmid, A. G. *Synt. Met.* **2002**, 125, 11-22.

(36) Zhang, D.; Wang, Y. *Mat. Sci. Eng. B* **2006**, 134, 9-19.

(37) Lu, X.; Zhang, W.; Wang, C.; Wen, T.; Wei, Y. *Prog. Polym. Sci.* **2011**, 36, 671-712.

(38) Chen, D.; Lei, S.; Chen, Y. *Sensors* **2011**, 11, 6509-6516. (39) Gospodinova, N.; Terlemezyan, L. *Prog. Polym. Sci.* **1998**, 23, 1443-1484.

(40) Gospodinova, N.; Mokreva, P.; Terlemezya, L. *Polymer* **1995**, 36, 3585-3587.

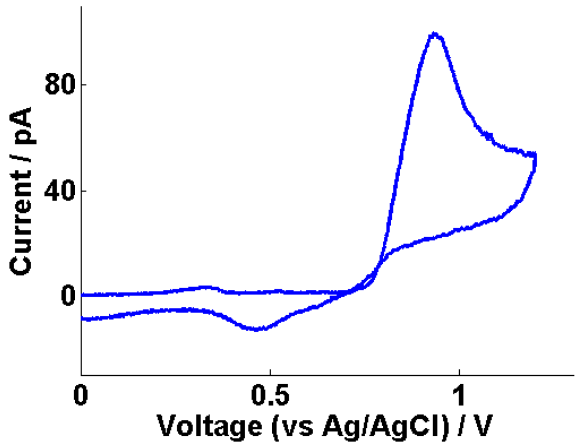

Figure 7.5: Cyclic voltammogram (200 mV s^{-1}) for the electropolymerization of polyaniline on a gold substrate using a 1 μm diameter SECCM probe. The solution in the probe contained 20 mM aniline hydrochloride and 75 μM HCl (36%).

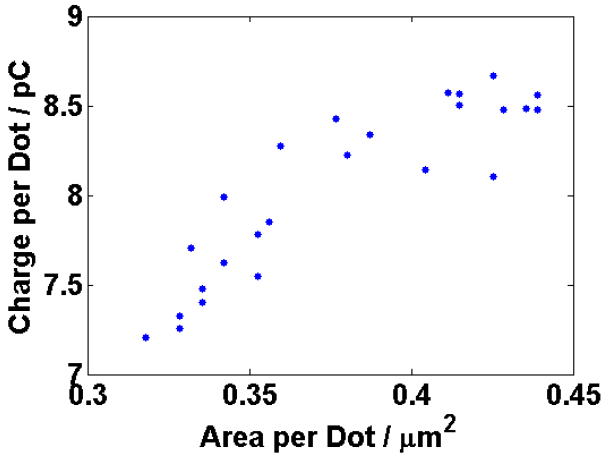

Figure 7.6: Scatter plot of dot size versus substrate charge for the array of 25 PANI dots shown in Figure 7.2.

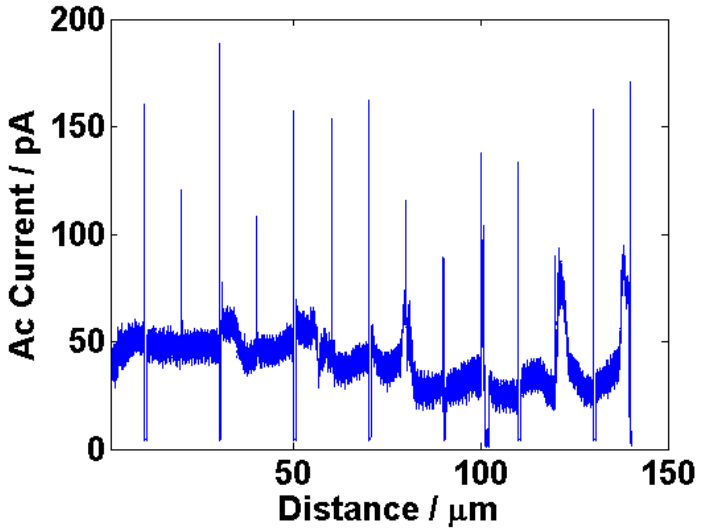

Figure 7.7: AC barrel current (feedback) measured during the deposition of PANI by controlling the surface potential (data in Figure 7.3 A).

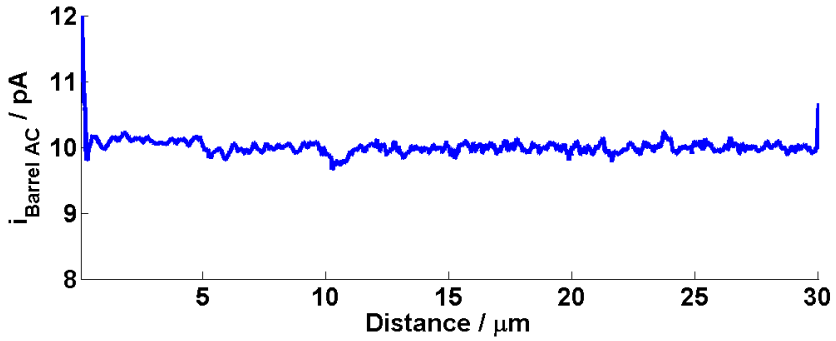

Figure 7.8: AC barrel current (feedback) during the deposition of PANI by galvanostatic control (data in Figure 7.3 B).

Chapter 8

Summary

EC-SPM allows the local flux (or concentration) of an electroactive species to be measured at, or close to, a surface (or interface). This provides information about the nature of the surface that cannot be easily obtained using other techniques. However, the probe must be placed precisely to avoid crashing into the surface. In addition, the quantitative analysis of the resulting electrochemical signal, typically measured at the probe, requires knowledge of this precise probe-substrate distance.

IC-SECM, presented in Chapter 2, is a new probe position technique that uses the physical interaction of the probe with the surface to determine the probe-surface separation. This new probe positioning technique complements other techniques such as shear force SECM, AC-SECM, AFM-SECM and SICM-SECM. An advantage of IC-SECM is the use of a non-electrochemical signal (the physical interaction of the probe with the surface) to detected the probe-surface distance. This allows many different types of probes, and modes of operation, to be used. However, the main advantage of IC-SECM is that it is simple and robust. A standard SECM probe (unlike shear force SECM, AFM-SECM or SICM-SECM) is used and minimal additional instrumentation is required.

As presented in Chapter 3, IC-SECM was used to study the molecular transport through dentin, an important biological membrane. IC-SECM allowed a UME

to be placed close to the dentin surface and redox active species that had passed though the sample to be detected at the UME. Knowledge of the probe-surface distance allowed FEM simulations to be used to quantify the electrochemical signal and extract the fluid flow rates through individual tubules. This research shows that IC-SECM provides additional information, in the form of the AC components, that can be used to analyse the probe response, as compared to a standard SECM approach.

As presented in Chapter 4, photosynthesis was investigated by placing a UME precisely, using the diffusion-limited feedback current, over isolated chloroplasts and thylakoid membranes, which contain the photosynthetic systems in higher plants. Using previous and new data, this allowed the production and consumption rates of oxygen to be measured and quantified using a FEM simulation. In addition, the detection of the interaction of an artificial electron acceptor with a single isolated thylakoid membrane was also demonstrated. This research shows the first use of SECM on isolated chloroplasts and thylakoid membranes, building on previous research using SECM to study photosynthesis.

A number of new techniques have been developed in the Warwick Electrochemistry and Interfaces group and new instruments were constructed to run these techniques. The new software, and hardware, for these new instruments was described in Chapter 5. These new instruments allowed new probe movement schemes to be quickly and easily implemented. These instruments demonstrate new capabilities and paradigms for EC-SPM research that are expected to be widely adopted in the future.

As presented in Chapter 6, a new dual electrode probe, which was quick and easy to fabricate, was developed. The probes were first characterised, using FEM simulations and IC-SECM, and then used to investigate two biologically relevant systems. Firstly, the oxidation of the important physiological agent, ascorbic acid (vitamin C), was investigated and quantified using a FEM simulation. Secondly,

the interaction of $FcTMA^{2+}$ with the thylakoid membrane bound photosynthetic electron transport pathway was observed for the first time. The new fabrication method greatly simplifies, compared to previously reported methods, the construction of duel electrode probes.

Finally, in Chapter 7, the theta-barrelled droplet technique, SECCM, was extended to include the electrochemical fabrication of nanoscale structures on surfaces. The liquid meniscus, which forms a nanoscale electrochemical cell, was used for the local electropolymerisation and deposition of a conducting polymer. The incorporation of the positional feedback, using the SECCM technique, allowed interesting structures to be constructed, and this shows how meniscus based fabrication methods can be easily and productively extended.

In summary, this thesis has shown the development of new EC-SPM techniques (Chapter 2 and 7), probes (Chapter 6), and instruments (Chapter 5). These have been used to investigate biologically relevant systems, such as dentin (Chapter 3), photosynthesis (Chapters 4 and 6) and ascorbic acid (Chapter 6).